Neutrinos as probes of hidden sectors

Matheus Hostert

A Thesis presented for the degree of
Doctor of Philosophy

Durham University

Institute for Particle Physics Phenomenology
Department of Physics
Durham University
United Kingdom

June 2019

Neutrinos as probes of hidden sectors

Matheus Hostert

Submitted for the degree of Doctor of Philosophy

June 2019

Abstract: This is some abstract about this thesis.

Dedicated to

Bárbara, Humberto and Luciana.

Contents

List of Figures

List of Tables

Declaration

The work in this thesis is based on research carried out in the Department of Physics at Durham University. No part of this thesis has been submitted elsewhere for any degree or qualification.

Acknowledgements

Chapter 1

Introduction

1.1 The Standard Model at 51

The Lagrangian density abov is the best experimentally verified description of nature we have. It stands for the Standard Model (SM) of particle physics, a theory that borrows the greatest theoretical physics ideas since the Maxwell equations, but which was officially born from the $SU(2)_L \times U(1)_Y$ theory of leptons by Weinber []. From its experimental success, we can gain confidence in our theoretical tools and methods, and from the shortcoming, we draw hope.

Self interactions ? gluons change colour. If we measure higgs self interactions, this will be a first. But how about longitudinal W and Z????????

Higgs questions ? elementary or composite? Natural? Portal to dark sector? All fermions get a mss from it? Is it alone? Single resonance?

1.1.1 Fields and symmetries

	Q_L	L	$\overline{u_R}$	$\overline{d_R}$	$\overline{e_R}$	H
SU(3)$_c$	**3**	**1**	$\overline{\mathbf{3}}$	$\overline{\mathbf{3}}$	**1**	**1**
SU(2)$_L$	**2**	**2**	**1**	**1**	**1**	**2**
U(1)$_Y$	1/3	-1	$-4/3$	2/3	2	1

Tab. 1.1. The representation of the SM left-handed Weyl fields and complex scalar under the gauge group. The last row stands for the U(1)$_Y$ charge.

The covariant derivative in the SM is given by

$$D_\mu = \partial_\mu + i g\, W_\mu^a \tau_a + i \frac{Y}{2} g'\, B_\mu + i \frac{g_s}{2}\, G_\mu^b \lambda_b, \qquad (1.1.1)$$

The covariant derivative allows us to *i)* write down kinetic terms for all SM fermions, *ii)* specify all gauge interactions for fermion and bosons. Take a purely electromagnetically interacting field ψ, for instance. A gauge transformation yields

$$\psi \to e^{-i\Lambda}\psi, \quad A_\mu \to A_\mu - \frac{1}{e}\partial_\mu\Lambda \implies D_\mu\psi \to e^{-i\Lambda}D_\mu\psi \implies \overline{\psi}i\slashed{D}\psi \to \overline{\psi}i\slashed{D}\psi,$$

explicitly showing the fermion kinetic term is invariant. Similar considerations apply for any gauge transformation within the SM. The invariant term in the relation above is the fermion kinetic term and it does not only allow for fermions to propagate, it also generates

all fermion-gauge interactions in the SM. Expanding it we have

$$\overline{\psi}\gamma^\mu \left[i\partial_\mu - g\, W_\mu^a \tau_a - \frac{Y}{2} g'\, B_\mu - \frac{g_s}{2}\, G_\mu^b \lambda_b \right] \psi, \tag{1.1.2}$$

1.1.2 Spontaneous symmetry breaking

After EWSB, the background higgs field always has a non-zero expectation value. In any isolated process, no matter how large the energies and momentum transfers involved, the relevant degrees of freedom are the ones in the broken phase (*i.e.h*).

1.1.3 Shortcomings

1.2 Portals to beyond the Standard Model

Given the hints that dark sectors beyond the SM may exist, we would like to investigate all the possible ways the particles in this sector may interact with the SM. One way to tackle this question is using effective field theories, where one studies all operators which are allowed by the content and symmetries of the SM. The idea is to construct a series of $d > 4$ operators in $1/\Lambda^{d-4}$, where Λ is the scale of the new physics. This approach thrives on its generality, but can become complicated very quickly with growing d. Most importantly, the scale Λ is assumed to be large, so that all new degrees of freedom have been integrated out of the theory. This is suitable for extentions involving particles which are very heavy, but the series is no longer well defined for new physics that is light and kinematically accessible at our experiments. In this case, the dynamics and kinematics of the new particles have to be specified, forcing us to write down the field content and symmetry group of the new physics. This is how we will proceed in this thesis.

We would like our SM extensions to follow specific *guiding principles* and *organise* them in a meaningful way. One way to do so is to study all the low dimension *neutral* operators that the SM has to offer. In contrast to effective field theories, we want *renormalisable* operators with $d < 4$ which are also gauge invariant. As it turns only a few such operators exist, which we usually refer to as portals. We dedicate the following sections to understanding these.

Neutrino portal Argubly the most motivated portal, this $d = 5/2$ operator can be written as

$$\left(\overline{L} \cdot H\right), \quad \text{and} \quad \left(\overline{L} \cdot \tilde{H}\right). \tag{1.2.1}$$

Any fermion field which couples to this operator acquires couplings to charged leptons and neutrinos in the standard model. The latter is particularly important, since it leads to mixing between the new species and the SM neutrinos. The new particle is then commonly called a *sterile neutrino* or a heavy neutral lepton.

Vector portal Any new vector particle from an abelian gauge may couple to the $d = 2$ field strength of the SM hypercharge

$$B_{\mu\nu}. \tag{1.2.2}$$

The resulting term, $B_{\mu\nu}X^{\mu\nu}$, is usually referred to as the kinetic mixing operator.

Higgs portal New scalar particles can mix with the SM higgs boson via

$$H^\dagger H. \tag{1.2.3}$$

In this case there are more possibilities depending on the nature of the new scalar field. Analogously to the SM, one could write $H^\dagger H \, S^\dagger S$ for a charged, or $H^\dagger H \, S$ for a siglet complex scalar. The latter term is the only super-renormalisable operator connecting the SM fields to new physics which is allowed. The phenomenology can be quite different depending on the charges of the new scalar, but in general The second operator has been discussed in detail in Ref. [14] and arises naturally in relaxion models ...).

A very simple BSM model with such portal arises in scalar singlet S extensions, where one generates the term $H^\dagger H \, S^\dagger S$ [15]. Remarkably, this extension can also have consequences to the "little hierarchy" problem, as the new scalar also contributes to the Higgs self-energy [16].

Fermionic currents A whole set of neutral operators in the SM come from the fermionic currents

$$J^\mu \equiv \overline{\psi}\gamma^\mu\psi, \tag{1.2.4}$$

where $\psi \in \{Q_L, L, u_R, d_R, \ell_R\}$. This provides SM currents which can be associated with new conserved quantities, *e.g.* we can choose to gauge. with a new vector. The first condition is that it be locally conserved $\partial_\mu J^\mu = 0$.

1.2.1   Others

Other possibilities for portals which we will not discuss in this thesis include the pseudoscalar portal, also known as the axion. This is also a very compelling avenue, as we generally expect light pseudo-Nambu-Goldstones to appear from the breaking of high scale symmetry groups. (see ...). Finally, see the dual...

Another interesting expectation for light new physics is that the new particles be electromagnetically neutral. This purely empirical constraint may not always hold, a classical example being millicharged particles which have escaped detection purely due to their small charges. The abelian nature of QED and of many of our SM extensions is actually unique in the sense that charge may not be quantized (see *e.g.* ...).

Chapter 2

Aspects of neutrino physics

2.1   Oscillations

2.2   Sources

To find a source of neutrinos, all we have to do is to look for environments where the Weak force is prominently manifested. A natural candidate, as we have seen in the discovery of the neutrino, are nuclear reactors. Fortunately, the list does not stop there. We now discuss in some detail some of the most important sources of neutrinos used in modern experiments.

Low energies (meV $\to$ MeV)

Medium energies (MeV $\to$ 100's of GeV)

High Energies (100's of GeV $\to$ EeV)

2.3   Scattering

Neutrino cross sections are an invaluable observable to understand the Weak force and to search for new physics.

2.4   Mass mechanisms

In Fig. 2.1, we show these unique tree-level completions of the Weinberg operator. For a review on low-scale models see [17].

2.4.1   Conventional seesaws

2.4.2   Low scale seesaw variants

2.4.3   Radiative masses

The most straightforward extension of the SM which can generate neutrino masses at loop level is perhaps the so-called Zee-Babu model.
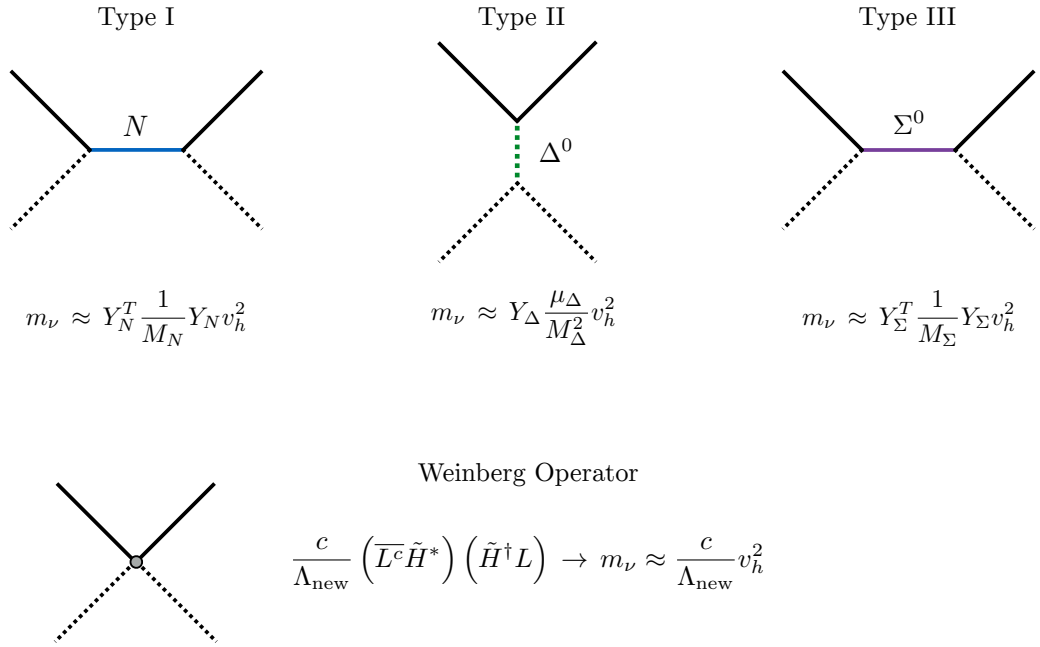
Fig. 2.1. The only three UV completions of the $d = 5$ Weinberg operator with their respective contributions to light neutrino masses.

Chapter 3

Neutrino Scattering

This chapter is dedicated to the study of rare neutrino scattering processes. Before we can explore the possibilities to constrain new physics, it is very important we understand our theoretical predictions in the SM. In this thesis we will see that leptonic and semi-leptonic neutrino scattering is a crucial tool to understanda and go beyond the SM. This chapter is dedicated to a refresher on neutrino-electron scattering and to original work developed on the calculation and phenomenology of neutrino trident scattering. These two processes were the object of study of experiments back in the 80's and 90's, but the high beam luminosity achieved at current neutrino experiments and expected at future facilitites (typically beyond 10^{21} protons on target), the relatively large fiducial masses of high-Z materials (typically 100 ton) of modern detectors, and improved particle idenditification (PID) capabilities allows to return to this topic at lower energies (E_ν = few GeV) with a refreshed approach.

3.1 Neutrino-electron scattering

Neutrino-electron scattering has long been a valuable probe of both the SM and potential new physics [18–21]. It is important to note that in the presence of novel leptophilic currents, experiments searching for e^+e^- tridents would also observe anomalous $\nu - e$ event rates. In fact, given the larger statistics present in the $\nu - e$ scattering sample, this channel is expected to provide the leading constraints in our scenarios with tree-level couplings to electrons.

In order to compute the $\nu - e$ cross section in the presence of the new leptophilic interactions we need to consider an analogous modification of the NC scattering amplitude

$$
\mathcal{M}_{\nu_\alpha - e} = -\frac{G_F}{\sqrt{2}} \left[\bar{u}(k_2)\gamma^\mu(1-\gamma_5)u(k_1) \right]
$$
$$
\times \left[\bar{u}(p_2)\gamma_\mu(C_\alpha^{\mathrm{V}} - C_\alpha^{\mathrm{A}}\gamma_5)u(p_1) \right], \tag{3.1.1}
$$

where the vector (C_V) and axial (C_A) effective couplings include both the SM and BSM contributions

$$
C_\alpha^{\mathrm{V}} = -\frac{1}{2} + 2s_{\mathrm{W}}^2 + \delta_{\alpha e} + \frac{Q_e^{\mathrm{V}} Q_\alpha^{\mathrm{L}}}{2\sqrt{2}G_F} \frac{(g')^2}{M_{Z'}^2 + 2m_e T_e}, \tag{3.1.2a}
$$
$$
C_\alpha^{\mathrm{A}} = -\frac{1}{2} + \delta_{\alpha e} + \frac{Q_e^{\mathrm{A}} Q_\alpha^{\mathrm{L}}}{2\sqrt{2}G_F} \frac{(g')^2}{M_{Z'}^2 + 2m_e T_e}, \tag{3.1.2b}
$$

with, as usual, $s_W \equiv \sin\theta_W$, being θ_W the weak angle and T_e is the kinetic energy of the recoil electron. The loop-induced kinetic mixing in the $L_\mu - L_\tau$ model also induces a $\nu - e$ coupling

$$C_\alpha^V = -\frac{1}{2} + 2s_W^2 + \delta_{\alpha e} + \frac{1}{\sqrt{2}G_F}\frac{g' \, e \, \varepsilon(q^2)}{M_{Z'}^2 + 2m_e T_e}. \tag{3.1.3}$$

The differential cross section is then given by

$$\frac{d\sigma_{\nu_\alpha - e}}{dT_e} = \frac{2m_e G_F^2}{\pi}\left[\left(C_\alpha^L\right)^2 + \left(C_\alpha^R\right)^2 \left(1 - \frac{T_e}{E_\nu}\right)^2\right.$$
$$\left. - C_\alpha^L C_\alpha^R \, m_e \frac{T_e}{E_\nu^2}\right]. \tag{3.1.4}$$

where the left and right handed constants are given by

$$C_\alpha^L \equiv \frac{1}{2}\left(C_\alpha^V + C_\alpha^A\right) \qquad \text{and} \qquad C_\alpha^R \equiv \frac{1}{2}\left(C_\alpha^V - C_\alpha^A\right).$$

For antineutrino scattering one obtains the cross section by exchanging $C_\alpha^L \leftrightarrow C_\alpha^R$.

3.1.1   Kinematics

The kinetic energy of the outgoing electron is bounded by kinematics and the energy resolution of the detector, which effectively sets a threshold energy T_{th} such that

$$T_{th} \leq T_e \leq T_{max}, \tag{3.1.5}$$

with $T_{max} = 2E_\nu^2/m_e + 2E_\nu$, the maximum kinetic energy attainable. We define the effective total cross section for an initial neutrino energy E_ν as

$$\sigma_{eff}(E_\nu, T_{th}) = \int_{T_{th}}^{T_{max}} \frac{d\sigma}{dT_e} \, dT_e. \tag{3.1.6}$$

This definition also ensures that the enhancement due to very light mediators becomes constant at around $\sqrt{2m_e T_{th}}$, as discussed in Ref. [21]. This is a consequence of the detector threshold and of the 2-body kinematics of the process. Finally, electroweak radiative corrections have been computed in the SM [22, 23], but will not be included here. Since they correspond to a change of a few percent we do not expect them to affect very much our results.

3.1.2 Measurements

MINERvA

CHARM-II, CHARM,

TEXONO, GEMMA, DAYA BAY?

3.2 Neutrino trident scattering

Trident events are processes predicted by the SM as the result of (anti)neutrino-nucleus scattering with the production of a charged lepton pair [24–28], $\overset{(-)}{\nu}_\alpha + \mathcal{H} \to \overset{(-)}{\nu}_{\alpha\,\mathrm{or}\,\kappa(\beta)} + \ell_\beta^- + \ell_\kappa^+ + \mathcal{H}$, $\{\alpha, \beta, \kappa\} \in \{e, \mu, \tau\}$[1] where $\mathcal{H}$ denotes a hadronic target. Depending on the (anti)neutrino and charged lepton flavours in the final-state, the process will be mediated by the Z^0 boson, W boson or both. Coherent interactions between (anti)neutrinos and the atomic nuclei are expected to dominate these processes as long as the momentum transferred Q is significantly smaller than the inverse of the nuclear size [24]. For larger momentum transfers diffractive and deep-inelastic scattering become increasingly relevant [29]. Although this process exists for all combinations of same-flavour or mixed flavour charged-lepton final-states, to this day only the ν_μ-induced dimuon mode, $\overset{(-)}{\nu}_\mu + \mathcal{H} \to \overset{(-)}{\nu}_\mu + \mu^+ + \mu^- + \mathcal{H}$, has been observed. The first measurement of this trident signal performed by CHARM II [30] is also the one with the largest statistics: 55 signal events in a beam of neutrinos and antineutrinos with $\langle E_\nu \rangle \approx 20$ GeV. Other measurements by CCFR [10] and NuTeV [31] at larger energies soon followed.

As the measurement of trident events may provide a sensitive test of the weak sector [32] as well as placing constraints on physics beyond the SM [9,10,33–37] it is relevant to investigate how to probe it further at current and future neutrino experiments. Atmospheric neutrinos, for instance, may provide a feasible measurement of the dimuon channel, as pointed out in Ref. [35][2]. Other trident modes were also recognized to be relevant by the authors of Ref. [29] who calculated the cross sections for trident production in all possible flavour combinations and estimated the number of events expected for the DUNE and SHiP experiments. They used the Equivalent Photon Approximation (EPA) [38] to compute the

---

[1]Throughout the manuscript we will consider α, β, κ as flavour indexes.

[2]The authors of Ref. [35] have performed the full calculation of the trident process and made their code publicly available.

cross section in the coherent and diffractive regimes of the scattering. The EPA, however, is known to breakdown for final state electrons [24, 39, 40] leading, as we will demonstrate here, to an overestimation of the cross section that in some cases is by more than 200%.

In this work, we present a unified treatment of the coherent and diffractive trident calculation beyond the EPA for all modes. We then compute the number and distribution of events expected in each mode at various near detectors, devoting particular attention to the case of liquid argon (LAr) detectors, as they are expected to lead the field of precision neutrino scattering measurements over the next few decades thanks to their excellent tracking and calorimetry capabilities. Finally, we address the likely backgrounds that may hinder these experimental searches — a question that we believe to be of utmost importance given the rarity of the process, and one that has been omitted in earlier sensitivity studies [29, 34].

This paper is organized as follows. In Sec. 3.3, we explain how to correctly calculate the trident SM cross sections, comparing our results to the EPA and explicitly showing the breakdown of this approximation. In Sec. 3.4, we discuss the trident event rates and kinematic distributions at the near detectors of several present and future neutrino oscillation experiments based on LAr technology: the three detectors of the Short-Baseline Neutrino (SBN) Program at Fermilab [41] and the near detector for the long-baseline Deep Underground Neutrino Experiment (DUNE) [42, 43], also located at Fermilab. We also consider the potential gains from an optimistic future facility: a 100 t LAr detector subject to the novel low-systematics neutrino beam of the Neutrinos from STORed Muons (νSTORM) project [44, 45]. We discuss the sources of background events at these facilities, providing a GENIE-level analysis [46] of how to reduce these backgrounds and assessing the impact they are expected to have on the trident measurement. In Sec. **??**, we discuss other near detectors that use more conventional technologies: the Interactive Neutrino GRID (INGRID) [47–50], the on-axis iron near detector for T2K at J-PARC, as well as three detectors at the Neutrino at the Main Injector (NuMI) beamline at Fermilab, the one for the Main INjector ExpeRiment ν-A (MINERνA) [51, 52] and the near detectors for the Main Injector Oscillation Search (MINOS) [53, 54] and the Numi Off-axis ν_e Appearance (NOνA) experiment [55, 56].

3.3 Trident Production Cross Section

In this section we consider neutrino trident production in the SM, defined as the process where a (anti)neutrino scattering off a hadronic system $\mathcal{H}$ produces a pair of same-flavour or mixed flavour charged leptons

$$\overset{(-)}{\nu_\alpha}(p_1) + \mathcal{H}(P) \rightarrow \overset{(-)}{\nu}_{\alpha \,\mathrm{or}\, \kappa(\beta)}(p_2) + \ell_\beta^-(p_4) + \ell_\kappa^+(p_3) + \mathcal{H}(P'), \qquad (3.3.1)$$

where $\beta(\kappa)$ corresponds to the flavour index of the negative (positive) charged lepton in both neutrino and antineutrino cases. Neutrino trident scattering can be divided into three regimes depending on the nature of the hadronic target: coherent, diffractive and deep inelastic, when the neutrino scatters off the nuclei, nucleons and quarks, respectively. At the energies relevant for neutrino oscillation experiments, the deep inelastic scattering contribution amounts at most to 1% of the total trident production cross section [29] and we will not consider it further.

The cross section for trident production has been calculated before in the literature, both in the context of the $V - A$ theory [24–26] and in the SM [32], while the EPA treatment was developed in Refs. [38–40]. Most calculations have focused on the coherent channels [24–26, 32, 38] but the diffractive process has been considered in [24, 25]. More recently, calculations using the EPA have been performed for coherent scattering with a dimuon final-state [34], and for all combinations of hadronic targets and flavours of final-states in [29]. While the EPA is expected to agree reasonably well with the full calculation for coherent channels with dimuon final-states, the assumptions of this approximation are invalid for the coherent process with electrons in the final-state [24, 39, 40]. For this reason, we perform the full $2 \rightarrow 4$ calculation without the EPA in a manner applicable to any hadronic target, following a similar approach to Refs. [24, 25]. Our treatment of the cross section allows us to quantitatively assess the breakdown of the EPA in both coherent and diffractive channels for all final-state flavours, an issue we come back to in Sec. 3.3.2.

We write the total cross section for neutrino trident production off a nucleus $\mathcal{N}$ with Z protons and $(A - Z)$ neutrons as the sum

$$\sigma_{\nu\mathcal{N}} = \sigma_{\nu\mathrm{c}} + \sigma_{\nu\mathrm{d}}, \qquad (3.3.2)$$

where $\sigma_{\nu\mathrm{c}}$ ($\sigma_{\nu\mathrm{d}}$) is the coherent (diffractive) part of the cross section. The relevant diagrams
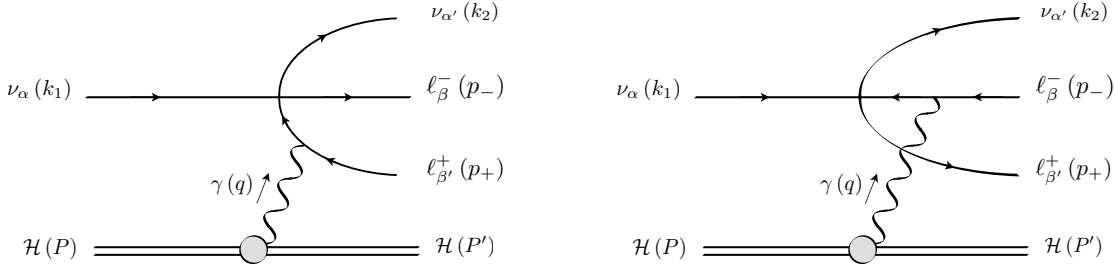
Fig. 3.1. Diagrams contributing to the neutrino trident process in the four-point interaction limit of the Standard Model.

for these processes in the coherent or diffractive regimes involve the boson Z^0, W or both mediators, depending on the particular mode. In the four-point interaction limit, depicted in Fig. 5.1, these reduce to only two contributions[3], one where the photon couples to the negatively and one to the positively charged lepton. In Table 3.1 we present the processes that will be considered in this work as well as the SM contributions present in each. Although our formalism applies also to processes with final-state τ leptons, the increased threshold makes them irrelevant for the experiments of interest in this study and we do not consider them further. The trident amplitude for a coherent (X = c) or diffractive (X = d) scattering regime can be written as

$$i\mathcal{M} = \mathrm{L}^\mu(\{p_i\}, q) \frac{-ig_{\mu\nu}}{q^2} \mathrm{H}^\nu_\mathrm{X}(P, P')\,, \qquad (3.3.3)$$

where $\{p_i\} = \{p_2, p_3, p_4\}$ is the set of outgoing leptonic momenta. $\mathrm{L}^\mu(\{p_i\}, q)$ is the total leptonic amplitude

$$\mathrm{L}^\mu \equiv -\frac{ieG_F}{\sqrt{2}} [\bar{u}(p_2)\gamma^\tau(1 - \gamma_5)u(p_1)] \times \bar{u}(p_4) \left[\gamma_\tau(V_{\alpha\beta\kappa} - A_{\alpha\beta\kappa}\gamma_5)\frac{1}{(\slashed{q} - \slashed{p}_3 - m_3)}\gamma^\mu \right.$$
$$\left. + \gamma^\mu \frac{1}{(\slashed{p}_4 - \slashed{q} - m_4)}\gamma_\tau(V_{\alpha\beta\kappa} - A_{\alpha\beta\kappa}\gamma_5) \right] v(p_3)\,, \qquad (3.3.4)$$

and $\mathrm{H}^\nu_\mathrm{X}(P, P')$ is the total hadronic amplitude

$$H^\nu_\mathrm{X} \equiv \langle \mathcal{H}(P)|J^\nu_\mathrm{E.M.}(q^2)|\mathcal{H}(P')\rangle\,, \qquad (3.3.5)$$

with $q \equiv P - P'$ denoting the transferred momentum, m_3 (m_4) the positively (negatively) charged lepton mass, $V_{\alpha\beta\kappa}(A_{\alpha\beta\kappa}) \equiv g_V^\beta(g_A^\beta)\delta_{\beta\kappa} + \delta_{\alpha\beta}$ ($\beta = \alpha$ or κ) the vector (axial)

---

[3]An additional diagram involving a $WW\gamma$ vertex has also been neglected, since it is of order $1/M_W^4$.

(Anti)Neutrino	SM Contributions
$\overset{(-)}{\nu_\mu}\,\mathcal{H} \to \overset{(-)}{\nu_\mu}\,\mu^-\mu^+\,\mathcal{H}$	CC + NC
$\overset{(-)}{\nu_\mu}\,\mathcal{H} \to \overset{(-)}{\nu_e}\,e^\pm\mu^\mp\,\mathcal{H}$	CC
$\overset{(-)}{\nu_\mu}\,\mathcal{H} \to \overset{(-)}{\nu_\mu}\,e^-e^+\,\mathcal{H}$	NC
$\overset{(-)}{\nu_e}\,\mathcal{H} \to \overset{(-)}{\nu_e}\,e^-e^+\,\mathcal{H}$	CC + NC
$\overset{(-)}{\nu_e}\,\mathcal{H} \to \overset{(-)}{\nu_\mu}\,\mu^\pm e^\mp\,\mathcal{H}$	CC
$\overset{(-)}{\nu_e}\,\mathcal{H} \to \overset{(-)}{\nu_e}\,\mu^-\mu^+\,\mathcal{H}$	NC

Tab. 3.1. (Anti)Neutrino trident processes considered in this paper.

couplings, depending on the channel and have labels in accordance to Eq. (3.3.1), and $J^\nu_{\text{E.M.}}(q^2)$ the electromagnetic current for the hadronic system $\mathcal{H}$ (a nucleus or a nucleon).

We can write the differential cross section as

$$\frac{\mathrm{d}^2\sigma_{\nu\mathrm{X}}}{\mathrm{d}Q^2\mathrm{d}\hat{s}} = \frac{1}{32\pi^2(s - M^2_{\mathcal{H}})^2}\frac{\mathrm{H}^{\mu\nu}_{\mathrm{X}}\mathrm{L}_{\mu\nu}}{Q^4}\,, \tag{3.3.6}$$

where $s = (p_1 + P)^2$, $\hat{s} \equiv 2\,(p_1 \cdot q)$, $Q^2 = -q^2$ and $M_{\mathcal{H}}$ is the mass of the hadronic target. We have also introduced the hadronic tensor $\mathrm{H}^{\mu\nu}_{\mathrm{X}}$

$$\mathrm{H}^{\mu\nu}_{\mathrm{X}} \equiv \overline{\sum_{\text{spins}}}\,(\mathrm{H}^\mu_{\mathrm{X}})^*\,\mathrm{H}^\nu_{\mathrm{X}}. \tag{3.3.7}$$

The two scattering regimes in which the hadronic tensor is computed will be discussed in more detail in Sec. 3.3.1. The leptonic tensor, $\mathrm{L}^{\mu\nu}$, integrated over the phase space of the three final-state leptons, $\mathrm{d}^3\Pi\,(p_1 + q; \{p_i\})$, and merely summed over final and initial spins is given by

$$\mathrm{L}^{\mu\nu}(p_1, q) \equiv \int \mathrm{d}^3\Pi\,(p_1 + q; \{p_i\}) \left(\sum_{\text{spins}} (\mathrm{L}^\mu)^*\,\mathrm{L}^\nu\right). \tag{3.3.8}$$

We can use $\mathrm{L}^{\mu\nu}$ to define two scalar functions, one related to the longitudinal ($\mathrm{L_L}$) and the other to the transverse ($\mathrm{L_T}$) polarization of the exchanged photon

$$\mathrm{L_T} = -\frac{1}{2}\left(g^{\mu\nu} - \frac{4Q^2}{\hat{s}^2}p_1^\mu p_1^\nu\right)\mathrm{L}_{\mu\nu}, \quad \text{and} \quad \mathrm{L_L} = \frac{4Q^2}{\hat{s}^2}p_1^\mu p_1^\nu\mathrm{L}_{\mu\nu}\,. \tag{3.3.9}$$

This allows us to write the differential cross section as a sum of a longitudinal and a transverse contribution [57] as follows

$$\frac{\mathrm{d}^2\sigma_{\nu\mathrm{X}}}{\mathrm{d}Q^2\mathrm{d}\hat{s}} = \frac{1}{32\pi^2}\frac{1}{\hat{s}\,Q^2}\left[h^{\mathrm{T}}_{\mathrm{X}}(Q^2, \hat{s})\,\sigma^{\mathrm{T}}_{\nu\gamma}(Q^2, \hat{s}) + h^{\mathrm{L}}_{\mathrm{X}}(Q^2, \hat{s})\,\sigma^{\mathrm{L}}_{\nu\gamma}(Q^2, \hat{s})\right], \tag{3.3.10}$$

where we have defined two functions for the flux of longitudinal and transverse virtual photons

$$h_{\mathrm{X}}^{\mathrm{T}}(Q^2, \hat{s}) \equiv \frac{2}{(E_\nu M_{\mathcal{H}})^2} \left[p_{1\mu} p_{1\nu} - \frac{\hat{s}^2}{4Q^2}\, g_{\mu\nu} \right] \mathrm{H}_{\mathrm{X}}^{\mu\nu}, \quad \text{and} \tag{3.3.11a}$$

$$h_{\mathrm{X}}^{\mathrm{L}}(Q^2, \hat{s}) \equiv \frac{1}{(E_\nu M_{\mathcal{H}})^2}\, p_{1\mu} p_{1\nu}\, \mathrm{H}_{\mathrm{X}}^{\mu\nu}, \tag{3.3.11b}$$

and two leptonic neutrino-photon cross sections associated with them[4]

$$\sigma_{\nu\gamma}^{\mathrm{T}}(Q^2, \hat{s}) = \frac{\mathrm{L}_{\mathrm{T}}}{2\hat{s}}, \quad \text{and} \quad \sigma_{\nu\gamma}^{\mathrm{L}}(Q^2, \hat{s}) = \frac{\mathrm{L}_{\mathrm{L}}}{\hat{s}}. \tag{3.3.12}$$

The kinematically allowed region in the $(Q^2, \hat{s})$ plane can be obtained by considering the full four-body phase space, as in [24–26]. The limits for such physical region are given by

$$Q_{\min}^2 = \frac{M_{\mathcal{H}} \hat{s}^2}{2E_\nu (2E_\nu M_{\mathcal{H}} - \hat{s})}, \qquad\qquad Q_{\max}^2 = \hat{s} - m_L^2, \tag{3.3.13a}$$

$$\hat{s}_{\min} = \frac{E_\nu}{2E_\nu + M_{\mathcal{H}}} \left[m_L^2 + 2E_\nu M_{\mathcal{H}} - \Delta \right] \qquad \hat{s}_{\max} = \frac{E_\nu}{2E_\nu + M_{\mathcal{H}}} \left[m_L^2 + 2E_\nu M_{\mathcal{H}} + \Delta \right], \tag{3.3.13b}$$

with $m_L \equiv m_3 + m_4$, and

$$\Delta \equiv \sqrt{(2E_\nu M_{\mathcal{H}} - m_L^2)^2 - 4M_{\mathcal{H}}^2 m_L^2}.$$

Let us emphasize that Eq. (3.3.10) is an exact decomposition, and does not rely on any approximation of the process. In the following section, we will show how to calculate the flux functions $h_{\mathrm{X}}^{\mathrm{T}}$ and $h_{\mathrm{X}}^{\mathrm{L}}$ from Eq. 3.3.11 in different scattering regimes. The total cross section for the process can then be computed by finding $\sigma_{\nu\gamma}^{\mathrm{L}}$ and $\sigma_{\nu\gamma}^{\mathrm{T}}$ from Eqs. (3.3.4), (3.3.8) and (3.3.9) and integrating over all allowed values of Q^2 and $\hat{s}$. Note that $\sigma_{\nu\gamma}^{\mathrm{L}}$ and $\sigma_{\nu\gamma}^{\mathrm{T}}$ are universal functions for a given leptonic process and need only to be computed once.

3.3.1 Hadronic Scattering Regimes

Depending on the magnitude of the virtuality of the photon, $Q = \sqrt{-q^2}$, the hadronic current can contribute in different ways to the trident process. Thus, given the decomposition in Eq. (3.3.10), the change in the hadronic treatment translates to computing the

---

[4]Note that we include a factor of $1/2$ in $\sigma_{\nu\gamma}^{\mathrm{T}}$ to match the polarization averaging of the on-shell cross section: $\sigma_{\nu\gamma}^{\mathrm{on-shell}} = \frac{1}{2\hat{s}} \left(\overline{\sum}_r (\epsilon_r^\mu)^* \epsilon_r^\nu \mathrm{L}_{\mu\nu} \right) \big|_{Q^2=0} = \frac{1}{4\hat{s}} \left(-g^{\mu\nu} \mathrm{L}_{\mu\nu} \right) \big|_{Q^2=0} = \frac{\mathrm{L}_{\mathrm{T}}}{2\hat{s}} \big|_{Q^2=0} = \sigma_{\nu\gamma}^{\mathrm{T}}(0, \hat{s})$.

flux factors h_X^T and h_X^L for each scattering regime. From those flux factors, $\sigma_{\nu c}$ and $\sigma_{\nu d}$ can be calculated.

Coherent Regime ($H_c^{\mu\nu}$)

In the coherent scattering regime the incoming neutrino interacts with the whole nucleus without resolving its substructure. For this to occur frequently, we need small values of Q. Despite the relatively large neutrino energies in contemporary neutrino beams, this is still allowed for trident.

In this regime, the hadronic tensor $H_c^{\mu\nu}$ for a ground state spin-zero nucleus of charge Ze can be written in terms of the nuclear electromagnetic form factor $F(Q^2)$, discussed in more detail in Appendix **??**, as

$$H_c^{\mu\nu} = 4Z^2 e^2 \left| F(Q^2) \right|^2 \left(P^\mu - \frac{q^\mu}{2} \right) \left(P^\nu - \frac{q^\nu}{2} \right). \tag{3.3.14}$$

From Eq. 3.3.11, we find that the transverse and longitudinal flux functions for the coherent regime are

$$h_c^T(Q^2, \hat{s}) = 8Z^2 e^2 \left(1 - \frac{\hat{s}}{2E_\nu M} - \frac{\hat{s}^2}{4E_\nu^2 Q^2} \right) |F(Q^2)|^2, \tag{3.3.15a}$$

$$h_c^L(Q^2, \hat{s}) = 4Z^2 e^2 \left(1 - \frac{\hat{s}}{4E_\nu M} \right)^2 |F(Q^2)|^2, \tag{3.3.15b}$$

where E_ν is the energy of the incoming neutrino and M is the nuclear mass. For a fixed value of $\hat{s}$ in the physical region, the h_c^T flux function becomes zero at $Q_{\min}$ while the longitudinal component does not. This different behaviour can be seen explicitly in their definitions, Eqs. (3.3.15), as the terms in the parenthesis in h_c^T cancel each other at $Q_{\min}$. This does not occur for h_c^L since the physical values of $\hat{s}$ are always smaller than $E_\nu M$ in this hadronic regime. Due to this fact, $Q_{\min}$, which according to Eq. (3.3.13a) depends on both the neutrino energy and target material, can be approximated to

$$Q_{\min} \approx \frac{\hat{s}}{2E_\nu},$$

which only depends on the incoming neutrino energy. On the other hand, as Q becomes large, the flux functions $h^{T,L}$ become quite similar, $h_c^T \approx 2h_c^L$, and favour small values of $\hat{s}$. After some critical value of the virtuality Q, $h_c^{T,L}$ become negligible due to the nuclear form factor. The Q value at which this happens depends on the target material, but not on
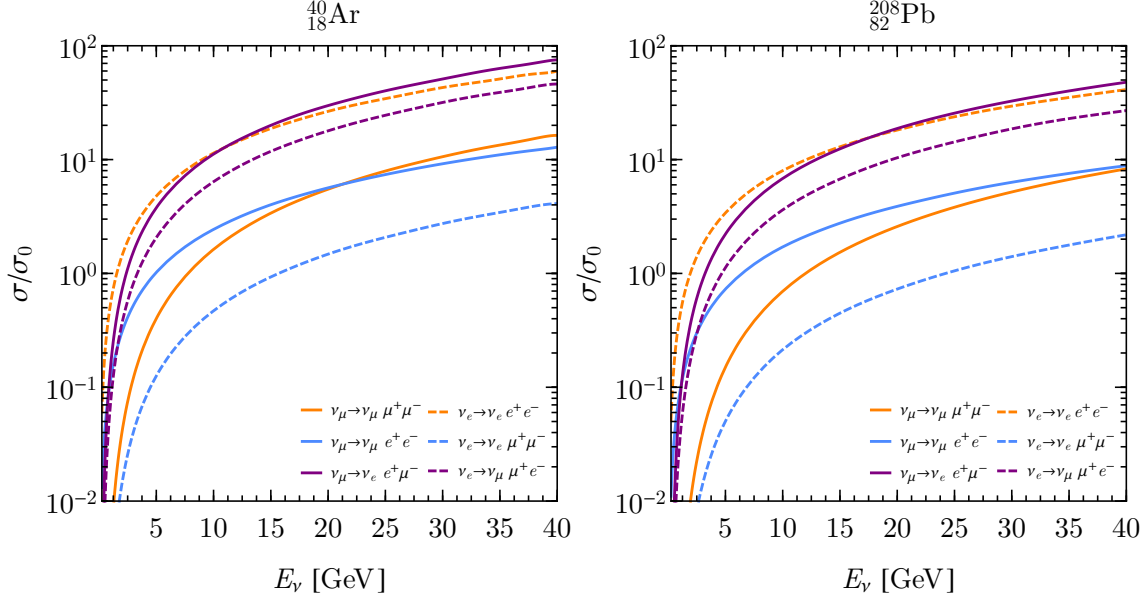
Fig. 3.2. Cross sections for coherent neutrino trident production on ^{40}Ar (left) and ^{208}Pb (right) normalized to $\sigma_0 = Z^2 \, 10^{-44}$ cm^2. The full (dashed) lines correspond to the scattering of an incoming ν_μ (ν_e) produced by the NC (light-blue), CC (purple), and CC+NC (orange) SM interactions.

the incoming neutrino energy. For instance, in the case of an Ar target the flux functions basically vanish for $Q \gtrsim 250$ MeV.

The final cross sections for coherent neutrino trident production on Argon can be seen in Fig. 3.2. Despite thresholds being important for the behaviour of these cross sections for GeV neutrino energies, we can see that mixed channels quickly become the most important due to their CC nature. At large energies one can then rank the cross sections from largest to smallest as CC, CC+NC, and NC only channels. Nevertheless, one must be aware of the fact that the cross sections are dominated by low Q^2 even at large energies, leading to large effects due to the final-state lepton masses as discussed in [29].

Diffractive Regime ($\mathrm{H}_\mathrm{d}^{\mu\nu}$)

At larger Q^2, the neutrino interacts with the individual nucleons of the nucleus. In this diffractive regime $\mathrm{H}_\mathrm{d}^{\mu\nu}$ is given by the sum of the contributions of the two types of nucleons: protons (N = p) and neutrons (N = n), so

$$\mathrm{H}_\mathrm{d}^{\mu\nu}(P, P') = Z \, \mathrm{H}_\mathrm{p}^{\mu\nu}(P, P') + (A - Z) \, \mathrm{H}_\mathrm{n}^{\mu\nu}(P, P') , \qquad (3.3.16)$$

where each $H_N^{\mu\nu}$ is the square of the matrix element of the nucleon electromagnetic current summed over final and averaged over initial spins. Neglecting second class currents, the matrix elements take the form

$$\langle N(P')| J_{E.M.}^\mu(Q^2) |N(P)\rangle = e\,\overline{u}_N(P')\left[\gamma^\mu F_1^N(Q^2) - i\frac{\sigma^{\mu\nu}q_\nu}{2M_N}F_2^N(Q^2)\right]u_N(P),\quad (3.3.17)$$

with $F_{1,2}^N(Q^2)$ the Dirac and Pauli form factors, respectively. The hadronic tensors are then given by [58]

$$H_N^{\mu\nu} = e^2\left[4\,H_1^N(Q^2)\left(P^\mu - \frac{q^\mu}{2}\right)\left(P^\nu - \frac{q^\nu}{2}\right) - H_2^N(Q^2)\left(Q^2 g^{\mu\nu} + q^\mu q^\nu\right)\right],\quad (3.3.18)$$

where the $H_1^N(Q^2)$ and $H_2^N(Q^2)$ form factors, functions of $F_{1,2}^N(Q^2)$, are given in Appendix **??**. The flux functions in the diffractive regime can then be calculated as

$$h_N^T(Q^2,\hat{s}) = 8\,e^2\left[\left(1 - \frac{\hat{s}}{2E_\nu M_N} - \frac{\hat{s}^2}{4E_\nu^2 Q^2}\right)H_1^N(Q^2) + \frac{\hat{s}^2}{8E_\nu^2 M_N^2}H_2^N(Q^2)\right],\quad (3.3.19a)$$

$$h_N^L(Q^2,\hat{s}) = 4e^2\left[\left(1 - \frac{\hat{s}}{4E_\nu M_N}\right)^2 H_1^N(Q^2) - \frac{\hat{s}^2}{16E_\nu^2 M_N^2}H_2^N(Q^2)\right].\quad (3.3.19b)$$

In the case of the proton, the flux functions $h_p^{T,L}$ have some unique features given the presence of both electric and magnetic contributions. Specifically, the transverse function is non-zero at $Q = Q_{min}$ for a fixed $\hat{s}$, due to the additional term proportional to H_2^p. Indeed, for large values of $\hat{s}$, the H_2^p term dominates the transverse function. An opposite behaviour occurs for the longitudinal component. There, the H_1^p term dominates over the second term for all physical values of $\hat{s}$, Q, and for any incoming neutrino energy. On the other hand, the flux functions of the neutron, which have only the magnetic moment contribution, have somewhat different characteristics. While h_n^T behaves similarly to h_p^T, that is, it is dominated by the second term for large values of $\hat{s}$, h_n^L is zero at Q_{min} due to the exact cancellation between the $H_{1,2}^n$ terms. This cancellation is not evident from Eq. (3.3.19b); however, simplifying the longitudinal component for the neutron case, one finds

$$h_n^L(Q^2,\hat{s}) = 4e^2\left(1 + \frac{Q^2}{4M_n^2}\right)\frac{Q^2}{4M_N^2}\left(1 - \frac{\hat{s}}{2E_\nu M_N} - \frac{\hat{s}^2}{4E_\nu^2 Q^2}\right)\left|F_2^n(Q^2)\right|^2,$$

which is zero for $Q = Q_{min}$. Also, this shows why h_p^L does not vanish at Q_{min} since there we have the additional contribution of the electric component.

When the neutrino interacts with an individual nucleon inside the nucleus, one must be aware of the nuclear effects at play. One such effect is Pauli blocking, a suppression of

neutrino-nucleon interactions due to the Pauli exclusion principle. Modelling the nucleus as an ideal Fermi gas of protons and neutrons, one can take Pauli blocking effects into account by requiring that the hit nucleon cannot be in a state which is already occupied [27]. This requirement is implemented in our calculations by a simple replacement of the differential diffractive cross section

$$\frac{\mathrm{d}^2\sigma_{\nu\mathrm{d}}}{\mathrm{d}Q^2\mathrm{d}\hat{s}} \to f(|\vec{q}|)\,\frac{\mathrm{d}^2\sigma_{\nu\mathrm{d}}}{\mathrm{d}Q^2\mathrm{d}\hat{s}},$$

where $|\vec{q}|$ is the magnitude of the transferred three-momentum in the lab frame. In particular, following [27], assuming an equal density of neutrons and protons, we have

$$f(|\vec{q}|) = \begin{cases} \dfrac{3}{2}\dfrac{|\vec{q}|}{2\,k_F} - \dfrac{1}{2}\left(\dfrac{|\vec{q}|}{2\,k_F}\right)^3, & \text{if } |\vec{q}| < 2\,k_F\,, \\ 1, & \text{if } |\vec{q}| \geq 2\,k_F\,, \end{cases} \tag{3.3.20}$$

where k_F is the Fermi momentum of the gas, taken to be 235 MeV. This is a rather low value of k_F and the assumption of equal density of neutrons and protons must be taken with care for heavy nuclei. We refrain from trying to model any additional nuclear effects as we believe that this is the dominant effect on the total diffractive rate, particularly when requiring no hadronic activity in the event. The net result is a reduction of the diffractive cross section by about 50% for protons and 20% for neutrons. Unless clearly stated otherwise, we always include Pauli blocking in our calculations.

Our final cross sections for this regime can be seen in Fig. 3.3. One can clearly see that the neutron contribution is subdominant, and that, up to factors of Z^2, the proton one is comparable to the coherent cross section. Note that now the typical values of Q^2 are much larger than in the coherent regime and the impact of the final-state lepton masses is much smaller.

3.3.2   Breakdown of the EPA

In order to understand the breakdown of the EPA in the neutrino trident case, let us first remind briefly the reader about the Weizsäcker–Williams method of equivalent photons in Quantum Electrodynamics (QED) [59, 60], and the main reason for its validity in that theory. The EPA, first introduced by E. Fermi [61], is based on a simple principle: when an ultra-relativistic particle P_i approaches a charged system C_s, like a nucleus, it will
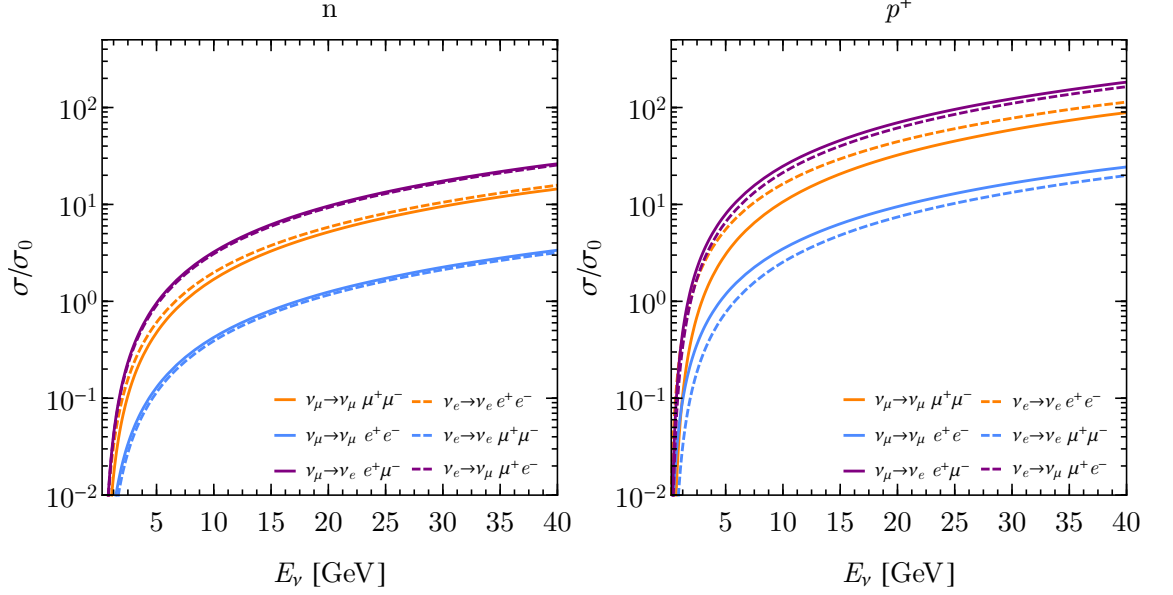
Fig. 3.3. Cross sections for diffractive neutrino trident production on neutrons (left) and protons (right), including Pauli blocking effects as described in the text, normalized to $\sigma_0 = 10^{-44}$ cm^2. The full (dashed) lines correspond to the scattering of an incoming ν_μ (ν_e) produced by the NC (light-blue), CC (purple), and CC+NC (orange) SM interactions.

perceive the electromagnetic fields as nearly transverse, similar to the fields of a pulse of radiation, *i.e.*, as an on-shell photon. Therefore, it is possible to obtain an approximate total cross section for the inelastic scattering process producing a set of final particles P_f, $\sigma_t(P_i + C_s \rightarrow P_f + C_s)$, by computing the scattering of the incoming particle with a real photon integrated over the energy spectrum of the off-shell photons,

$$\sigma_t(P_i + C_s \rightarrow P_f + C_s) \approx \int dP(Q^2, \hat{s}) \, \sigma_\gamma(P_i + \gamma \rightarrow P_f; \hat{s}, Q^2 = 0), \qquad (3.3.21)$$

where the photo-production cross section for the process $P_i + \gamma \rightarrow P_f$, $\sigma_\gamma(P_i + \gamma \rightarrow P_f; \hat{s}, Q^2 = 0)$, depends on the center-of-mass energy of the P_i–photon system, $\sqrt{\hat{s}}$. Here $dP(Q^2, \hat{s})$ corresponds to the energy spectrum of the virtual photons, that is, the probability of emission of a virtual photon with transferred four-momentum Q^2 resulting in an center-of-mass energy $\sqrt{\hat{s}}$. For trident scattering off a nuclear target, this probability can be approximated by [34, 38]

$$dP(Q^2, \hat{s}) = \frac{Z^2 e^2}{4\pi^2} |F(Q^2)|^2 \, \frac{d\hat{s}}{\hat{s}} \, \frac{dQ^2}{Q^2} \, . \qquad (3.3.22)$$

A crucial fact in QED is that the cross section $\sigma_\gamma^{\text{QED}}(P_i + \gamma \to P_f; \hat{s}, 0)$ is inversely proportional to $\hat{s}$,

$$\sigma_\gamma^{\text{QED}}(P_i + \gamma \to P_f; \hat{s}, 0) \propto \frac{1}{\hat{s}}.$$

We see clearly that small values of $\hat{s}$ and consequently of the transferred four-momentum Q^2 dominate the cross section. Hence, the on-shell contribution is much more significant than the off-shell one, so the EPA will be valid and give the correct cross section estimate for any QED process.

Now, let us consider the case of neutrino trident production. In this case, the equivalent-photon cross section in the four-point interaction limit has a completely opposite dependence on the center-of-mass energy; it is *proportional* to $\hat{s}$,

$$\sigma_\gamma^{\text{FL}}(P_i + \gamma \to P_f; \hat{s}, 0) \propto G_{\text{F}}^2 \, \hat{s}.$$

This dependence is a manifestation of the unitarity violation in the Fermi theory. Therefore, we can see that for weak processes larger values of $\hat{s}$, and, consequently, larger values of Q^2 are more significant [39, 40]. The EPA is then generally not valid for the neutrino trident production, as the virtual photon contribution dominates over the real one. Nevertheless, one may wonder if there is a situation in which the EPA can give a reasonable estimate for a neutrino trident process. As noticed in the early literature [39, 40], the presence of the nuclear form factor introduces a cut in the transferred momentum which, in turn, makes the EPA applicable for the specific case of the dimuon channel in the coherent regime. Let us discuss this in more detail.

Recalling our exact decomposition, Eq. (3.3.10), it is necessary to consider two assumptions for implementing the EPA [39]:

1. The longitudinal polarization contribution to the cross section can be neglected, i.e., $\sigma_{\nu\gamma}^{\text{L}}(Q^2, \hat{s}) \approx 0$;

2. The transverse polarization contribution to the cross section can be taken to be on-shell, i.e., $\sigma_{\nu\gamma}^{\text{T}}(Q^2, \hat{s}) \approx \sigma_{\nu\gamma}^{\text{T}}(0, \hat{s})$.

Assuming for now that these approximations hold, we can find a simplified expression for the coherent neutrino-target process, described by Eqs. (3.3.10) and (3.3.15), in terms of

the photon-neutrino cross section[5]:

$$\sigma_{\text{EPA}} = \frac{Z^2 e^2}{4\pi^2} \int_{m_L^2}^{\hat{s}_{\max}} \frac{d\hat{s}}{\hat{s}} \, \sigma_{\nu\gamma}^{\text{T}}(0, \hat{s}) \int_{(\hat{s}/2E_\nu)^2}^{Q_{\max}^2} \frac{|F(Q^2)|^2}{Q^4} \left[Q^2(1-y) - M_{\mathcal{H}}^2 y^2 \right] dQ^2, \quad (3.3.23)$$

where we introduced the fractional change of the nucleus energy y, defined as $\hat{s} = (s - M_{\mathcal{H}}^2)y$, and the integration limits can be obtained from (3.3.13) after considering that $m_L^2 \ll E_\nu M_{\mathcal{H}}$. Keeping only the leading terms in the small parameter y [38], we recover the EPA applied to the neutrino trident case

$$\sigma_{\text{EPA}} = \int \sigma_{\nu\gamma}^{\text{T}}(0, \hat{s}) \, dP(Q^2, \hat{s}), \qquad (3.3.24)$$

where $dP(Q^2, \hat{s})$ is given in Eq. (3.3.22). The EPA in the form of Eq. (3.3.24) has been used in trident calculations for the coherent dimuon channel [34] as well as for coherent mixed- and electron-flavour trident modes and diffractive trident modes [29]. Using our decomposition, we can explicitly compute both $\sigma_{\nu\gamma}^{\text{L}}$ and $\sigma_{\nu\gamma}^{\text{T}}$ and verify if the EPA conditions are satisfied for any channel and, if they are not, quantify the error introduced by making this approximation. For that purpose, we will compare the results of the full calculation, Eq. (3.3.10), with the EPA results, Eq. (3.3.24), by computing the following ratios in the physical region of the $(Q, \hat{s})$ plane,

$$\frac{\sigma^{\text{L}}(Q^2, \hat{s}) \, h_{\text{c}}^{\text{L}}(Q^2, \hat{s})}{\sigma^{\text{T}}(Q^2, \hat{s}) \, h_{\text{c}}^{\text{T}}(Q^2, \hat{s})}, \quad \frac{\sigma_{\nu\gamma}^{\text{T}}(Q^2, \hat{s})}{\sigma_{\nu\gamma}^{\text{T}}(0, \hat{s})}. \qquad (3.3.25)$$

The first ratio in Eq. (3.3.25) will indicate where the longitudinal contribution can be neglected compared to the transverse one; while, the second ratio will show where the transverse contribution behaves as an on-shell photon.

As an illustration of the general behaviour, we show in Fig. 3.4 those ratios of cross sections for an incoming ν_μ of fixed energy $E_\nu = 3$ GeV colliding coherently with an ^{40}Ar target, for the dielectron (left panels), mixed (middle panels) and dimuon (right panels) channels. On the top panels of Fig. 3.4 we see that the longitudinal component can be neglected for $Q \lesssim m_\alpha$, for the dielectron and dimuon channels, $\alpha = e, \mu$, while in the mixed case there is a much less pronounced hierarchy between the transverse and longitudinal components. On the bottom panels we have the comparison between on-shell and off-shell transverse photo-production cross sections. Again, we find that the EPA is only valid for $Q \lesssim m_\alpha$

---

[5]An analogous expression can be obtained for the diffractive regime from Eq. (3.3.19).
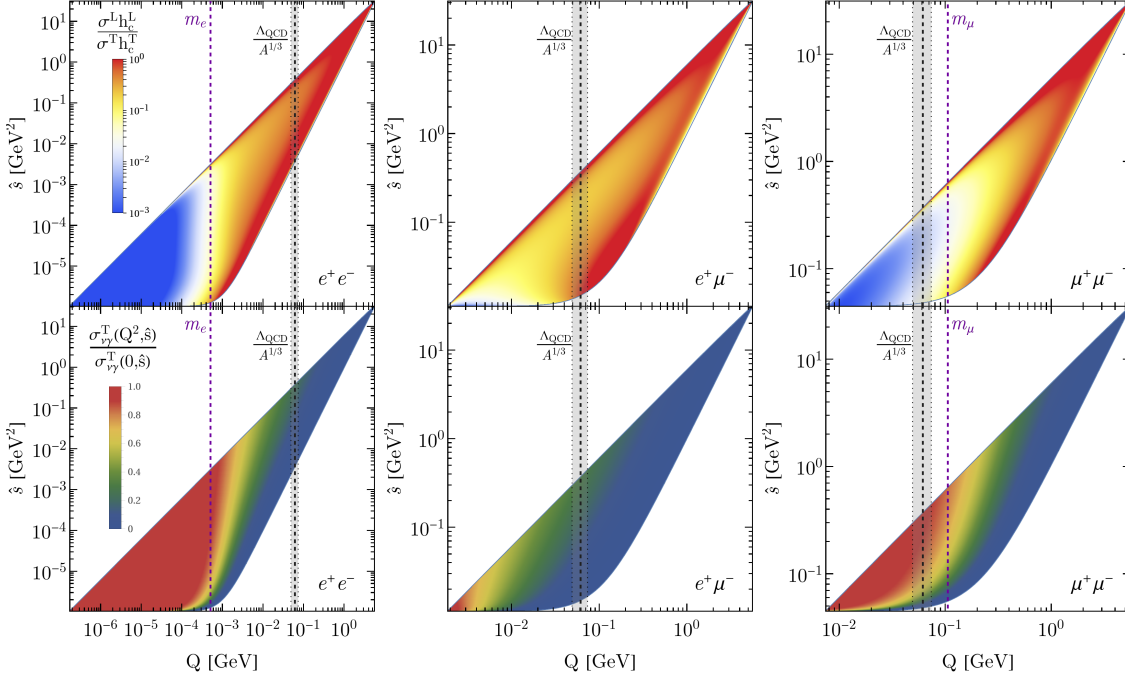
Fig. 3.4. Comparison between the full calculation of the trident production coherent cross section and the EPA in the kinematically allowed region of the $(Q, \hat{s})$ plane for an incoming ν_μ with fixed energy $E_\nu = 3$ GeV colliding with an ^{40}Ar target. The left, middle and right panels correspond to the dielectron, mixed and dimuon final-states, respectively. The top panels correspond to the comparison between the longitudinal and transverse contributions while the bottom ones show the ratio between the transverse cross sections computed for an specific value of Q with the cross section for an on-shell photon. The thick black dashed lines correspond to the cut in the Q^2 integration at $\Lambda_{\rm QCD}^2/A^{2/3}$, and the shadowed region around these lines account for a variation of 20% in the value of this cut. The purple dashed lines are for $Q = m_\alpha$, $\alpha = e, \mu$ for the unmixed cases.

for the dielectron and dimuon channels. For the mixed case, there is only a very small region in $Q < 10^{-2}$ GeV for which the off-shell transverse cross section is comparable to the on-shell one. This relative suppression of the off-shell cross section can be understood by noticing that Q enters the lepton propagators, suppressing the process for $Q \gtrsim m_\alpha$. For mixed channels it is then the smallest mass scale (m_e) that dictates the fall-off of the matrix element in Q, whilst the heaviest mass (m_μ) defines the phase space boundaries, rendering most of this phase space incompatible with the EPA assumptions.

These results explicitly show that the EPA is, in principle, not suitable for any neutrino trident process as it can overestimate the cross section quite substantially by treating the photo-production cross section at large Q^2 as on-shell. However, as previously mentioned, in the coherent regime the nuclear form factor introduces a strong suppression for large values of Q^2. In general, this dominates the behaviour of the cross sections for values of Q^2
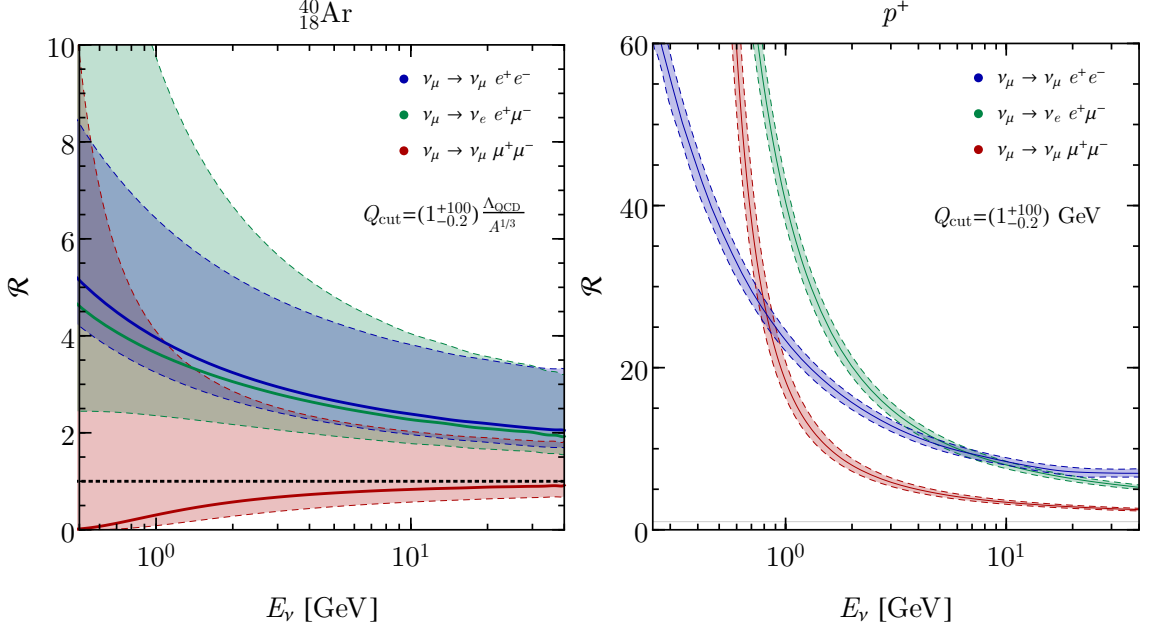
Fig. 3.5. Ratio $\mathcal{R}$ of the trident cross section calculated using the EPA to the full four-body calculation. Left panel: Ratio in the coherent regime on ^{40}Ar. The full curves correspond to the central value of Q_{cut}, and the upper (lower) boundary corresponds to a choice 100 times larger (20% smaller). Right panel: Ratio in the diffractive regime for scattering on protons, where the full curves corresponds to the central value of 1.0 GeV, and the upper (lower) boundary corresponds to a choice 100 times larger (20% smaller); we have taken the lower limit in the integration on Q to match the choice of the coherent regime and we do not include Pauli blocking in these curves. A guide to the eye at $\mathcal{R} = 1$ is also shown.

smaller than the purely kinematic limit, Q^2_{max}, and of the order of $\Lambda_{\text{QCD}}/A^{1/3} \approx 0.06$ GeV for coherent scattering on ^{40}Ar. In the dimuon case, the latter scale happens to be smaller than the charged lepton masses, implying that the region where the EPA breaks down is heavily suppressed due to the nuclear form factor. The same cannot be said about coherent trident channels involving electrons, as the nuclear form factor suppression happens for much larger values of Q than the EPA breakdown. Furthermore, for diffractive scattering the nucleon form factors suppress the cross sections only for much larger Q values, $Q \approx 0.8$ GeV. The effective range of integration then includes a significant region where the EPA assumptions are invalid, leading to an overestimation of the diffractive cross section for every process regardless of the flavours of their final-state charged leptons.

In some calculations, artificial cuts have been imposed on the range of Q^2, affecting the validity of the EPA. In Ref. [29], it is claimed that to avoid double counting between different regimes, an artificial cut must be imposed, lowering the upper limit of integration in Q^2. Ref. [29] chooses a value of $Q^{\text{cut}}_{\text{max}} = \Lambda_{\text{QCD}}/A^{1/3}$ in the coherent regime (black thick

dashed lines in Fig. 3.4), and $Q_{\mathrm{min}}^{\mathrm{cut}} = \max\left(\Lambda_{\mathrm{QCD}}/A^{1/3}, \hat{s}/2E_\nu\right)$ and $Q_{\mathrm{max}}^{\mathrm{cut}} = 1.0$ GeV in the diffractive regime. We believe that no such cut is required on physical grounds[6], and their presence will impact the EPA cross section quite dramatically. Let us first consider the dimuon case in the coherent regime, where the EPA assumptions hold reasonably well in the relevant parts of phase space. By introducing a value for $Q_{\mathrm{max}}^{\mathrm{cut}}$ we would be decreasing the total relevant phase space for the process, reducing the total cross section. Therefore, despite the EPA tendency to overestimate the cross section in this channel, an artificial cut in Q^2 can actually lead to an underestimation of the cross section. In the electron channels, where the EPA breakdown is much more dramatic, we can expect that the overestimation of the cross section by the EPA is reduced by the cut $Q_{\mathrm{max}}^{\mathrm{cut}}$. In fact, one way to improve the EPA for the dielectron channel is to artificially cut on the Q^2 integral around the region where the approximation breaks down [62]. This cut does then improve the coherent EPA calculation by decreasing the overestimation of the cross section. However, an energy independent cut cannot provide a good estimate of the cross section over all values of E_ν. To illustrate our point and to quantify the errors induced by the EPA, we show on the left panel of Fig. 3.5 the ratio $\mathcal{R}$ of the trident cross section calculated using the EPA with an artificial cut at Q_{cut}^2, as performed in [29], to the full calculation used in this work as a function of the incoming neutrino energy:

$$\mathcal{R} = \frac{\sigma_{\mathrm{EPA}}(E_\nu)|_{Q_{\mathrm{cut}}}}{\sigma_{\mathrm{4PS}}(E_\nu)} \,. \tag{3.3.26}$$

In this plot we vary the artificial cut on Q^2 around the choice of [29] (shown as the central dashed line) in two ways. First we reduce it by 20%, and then increase it by a large factor, recovering the case with no Q^2 cut. From this, our conclusions about the validity of the approximation are confirmed, and it becomes evident that the trident coherent cross section is very sensitive to the choice of Q_{cut}^2. In particular, the EPA with all the assumptions that lead to Eq. (3.3.24) and the absence of a Q^2 cut can lead to an overestimation of all trident channels, including the dimuon one. Once the cut is implemented, however, the approximation becomes better for the dimuon channel, but still unacceptable for the electron ones. It is also clear that an energy independent cut cannot give the correct cross section at all energies. This is particularly troublesome for detectors subjected to a neutrino

---

[6]It should be noted that the coherent and diffractive regimes have different phase space boundaries and that the form factors should guarantee their independence.

flux covering a wide energy range such as the near detectors for DUNE and MINOS or MINERνA. Moreover, Eq. (3.3.24) fails at low energies, and generally, overestimates the coherent cross sections by at least 200%. At these energies, one must be wary of the additional approximations in Eq. (3.3.24) regarding the integration limits and the small y limit.

On the right panel of Fig. 3.5 we illustrate what happens in the diffractive regime, where the nucleon form factors impact the cross section at much larger values of Q^2 and have a slower fall-off. We see that the diffractive cross section is dramatically overestimated over the full range of E_ν considered and for any trident mode. The discrepancy is particularly important for $E_\nu \lesssim 5$ GeV and larger than in the coherent regime by at least an order of magnitude[7]. We also see that the cuts on Q^2 impact the EPA calculation much less dramatically, and that its use is unlikely to yield the correct result.

Given these problems with both coherent and diffractive cross section calculations due to the breakdown of the EPA for trident production, in what follows we will use the complete four-body calculation.

3.3.3 Coherent versus Diffractive Scattering in Trident Production

Let us now comment on the significance of the coherent and diffractive contributions to the total cross for the different trident channels. In Fig. 3.6 we present the ratio of the coherent and the diffractive scattering cross sections to the total cross section for an ^{40}Ar target for an incoming ν_μ (left) and ν_e (right) neutrino. We can see that the coherent regime dominates at all neutrino energies when there is an electron in the final-state, especially in the dielectron case. This can be explained by noting that the Q^2 necessary to create an electron pair is smaller than the one needed to create a muon; thus, coherent scattering is more likely to occur for this mode. Conversely, as one needs larger momentum transferred to produce a muon (either accompanied by an electron or another muon) the diffractive regime becomes more likely in these modes, as we can explicitly see in Fig. 3.6. Because of this effect the diffractive contribution is $\lesssim 10\%$, except for the dimuon channel

---

[7]There are some differences in the treatment of the hadronic system between the EPA calculation in [29] and the one presented here. However, these differences are of the order 10% to 20%. Note also that we do not implement any Pauli blocking when calculating $\mathcal{R}$ to avoid ambiguities over the choice of the range of Q^2.
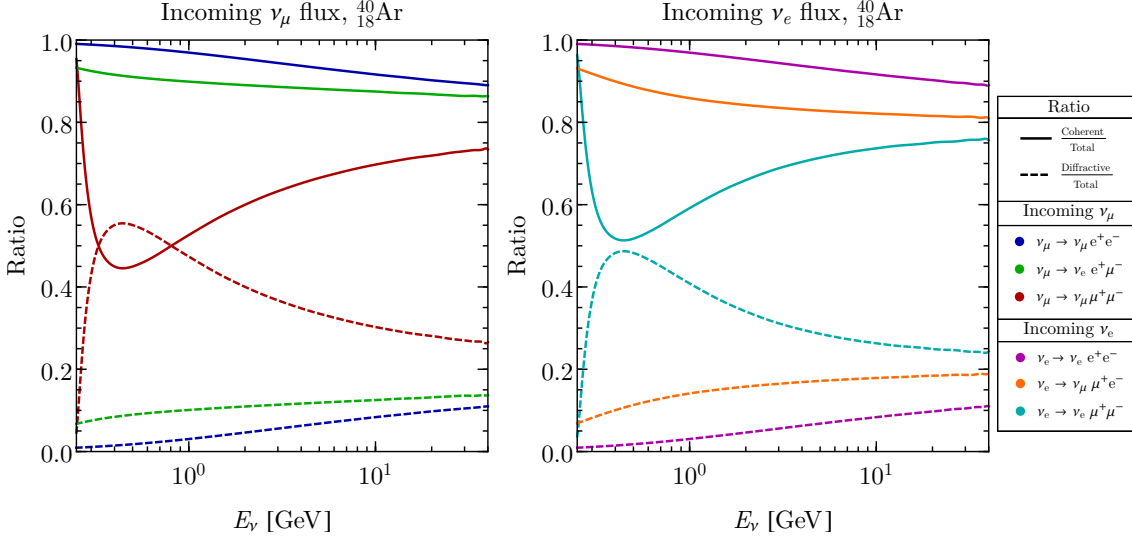
Fig. 3.6. On the left (right) panel we show the ratio of the coherent (full lines) and the diffractive (dashed lines) contributions to the total trident cross section for an incoming flux of $\nu_\mu(\nu_e)$ as a function of E_ν for an ^{40}Ar target.

where it can be between 30 and 40% in most of the energy region. Furthermore, when we compare the two incoming types of neutrinos, we see that for an incoming ν_μ the diffractive contribution is larger than the coherent one in the range $0.3\text{ GeV} \lesssim E_\nu \lesssim 0.8\text{ GeV}$, while for an incoming ν_e this never happens. This difference can be explained by the fact that CC and NC contributions are simultaneously present for the scattering of an initial ν_μ creating a muon pair, whereas for an initial ν_e creating a muon pair, we will only have the NC contribution, see Table 3.1.

An important difference between the coherent and diffractive regimes will be in their hadronic signatures in the detector. Neutrino trident production is usually associated with zero hadronic energy at the vertex, a feature that proved very useful in reducing backgrounds in previous measurements. Whilst this is a natural assumption for the coherent regime, it need not be the case in the diffractive one. In fact, in the latter it is likely that the struck nucleon is ejected from the nucleus in a significant fraction of events with Q exceeding the nuclear binding energy [8]. Since the dominant diffractive contribution comes from scattering on protons, these could then be visible in the detector if their energies are above threshold. On the other hand, the struck nucleon is subject to many nuclear effects which may significantly affect the hadronic signature, such as interactions

---

[8]The peak of our diffractive Q^2 distributions happens at around $Q \approx 300$ MeV, much beyond the typical binding energy for Ar (see Appendix **??**). Without Pauli suppression, however, we expect this value to drop.

of the struck nucleon in the nuclear medium as well as reabsorption. Our calculation of Pauli blocking, for example, shows large suppressions ($\sim 50\%$) precisely in the low Q^2 region, usually associated with no hadronic activity. This then raises the question of how well one can predict the hadronic signatures of diffractive events given the difficulty in modelling the nuclear environment. We therefore do not commit to an estimate of the number of diffractive events that would have a coherent-like hadronic signature, but merely point out that this might introduce additional uncertainties in the calculation, especially in the $\mu^+\mu^-$ channel where the diffractive contribution is comparable to the coherent one. Finally, from now on we will refer to the number of trident events with no hadronic activity as coherent-like, where this number can range from coherent only to coherent plus all diffractive events.

3.4 Trident Events in LAr Detectors

In this section we calculate the total number of expected trident events for some present and future LAr detectors with different fiducial masses, total exposures and beamlines. In Table **??** we specify the values used for each set-up and in Fig. **??** we show the total production cross section for each neutrino trident mode of Table 3.1 as well as the neutrino fluxes as a function of E_ν at the position of each experiment.

3.4.1 Event Rates

The total number of trident events, N_{X}^{ψ}, expected for a given trident mode at any detector is written as

$$N_{\mathrm{X}}^{\psi} = \mathrm{Norm} \times \int dE_\nu \, \sigma_{\nu\mathrm{X}}(E_\nu) \frac{d\phi_\nu(E_\nu)}{dE_\nu} \epsilon(E_\nu) \,, \tag{3.4.1}$$

where $\sigma_{\nu\mathrm{X}}$ can be the trident total (X $= \mathcal{N}$), coherent (X $=$ c) or diffractive (X $=$ d) cross sections for a given mode, ϕ_ν is the flux of the incoming neutrino and $\epsilon(E_\nu)$ is the efficiency of detection of the charged leptons. In the calculations of this section, we assume an efficiency of 100%[9]. The normalization is calculated as

$$\mathrm{Norm} = \mathrm{Exposure} \, [\mathrm{POT}] \times \frac{\mathrm{Fiducial \ Detector \ Mass} \times \mathrm{N_A}}{m_{\mathrm{T}}} \, [\mathrm{target \ particles}] \,,$$

---

[9]See Section B.0.1 for a discussion on the detection efficiencies for trident events and backgrounds.

where m_T is the molar mass of the target particle and N_A is Avogadro's number. Two features of the cross sections are important for the event rate calculation: threshold effects, especially for channels involving muons in the final-state, and cross section's growth with energy. In particular, we expect higher trident event rates for experiments with higher energy neutrino beams.

We start our study with the three detectors of the SBN program, one of which, μBooNE, is already installed and taking data at Fermilab. These three LAr time projection chamber detectors are located along the Booster Neutrino Beam line which is by now a well-understood source, having the focus of active research for over 15 years. Although the number of trident events expected in these detectors is rather low, they may offer one of the first opportunities to study trident events in LAr, as well as to better understand their backgrounds in this medium and to devise improved analysis techniques. After that we study the proposed near detector for DUNE. This turns out to be the most important LAr detector for trident production since it will provide the highest number of events in both neutrino and antineutrino modes. Finally, having in mind the novel flavour composition of neutrino beams from muon facilities, we investigate trident rates at a 100 t LAr detector for the νSTORM project. This last facility could offer a very well understood neutrino beam with as many electron neutrinos as muon antineutrinos from muon decays, creating new possibilities for trident scattering measurements.

The SBN Program   The SBN Program at Fermilab is a joint endeavour by three collaborations ICARUS, μBooNE and SBND to perform searches for eV-sterile neutrinos and study neutrino-Ar cross sections [41]. As can be seen in Tab. **??**, SBND has the shortest baseline (110 m) and therefore the largest neutrino fluxes (shown in Fig. **??** and taken from Fig. 3 of [41]). The largest detector, ICARUS, is also the one with the longest baseline (600 m) and consequently subject to the lowest neutrino fluxes. The ratio between the fluxes at the different detectors are $\phi_{\mu\text{BooNE}}/\phi_{\text{SBND}} = 5\%$ and $\phi_{\text{ICARUS}}/\phi_{\text{SBND}} = 3\%$. The neutrino beam composition is about 93% of ν_μ, 6% of $\overline{\nu}_\mu$ and 1% of $\nu_e + \overline{\nu}_e$.

Considering the difference in fluxes and the total number of targets in each of these detectors, one can estimate the following ratios of trident events: $N^\Psi_{\mu\text{BooNE}}/N^\Psi_{\text{SBND}} \sim 8\%$ and $N^\Psi_{\text{ICARUS}}/N^\Psi_{\text{SBND}} \sim 10\%$. Unfortunately, since the fluxes are peaked at a rather low energy ($E_\nu \lesssim 1$ GeV), where the trident cross sections are still quite small ($\lesssim 10^{-42}$ cm^2)

we expect very few trident events produced. The exact number of trident events for those detectors according to our calculations is presented in Tab. 3.2. For each trident channel the first (second) row shows the number of coherent (diffractive) events. As expected, less than a total of 20 events across all channels can be detected by SBND, and a negligible rate of events is expected at μBooNE and ICARUS.

DUNE Near Detector The DUNE experiment will operate with neutrino as well as antineutrino LBNF beams produced by directing a 1.2 MW beam of protons onto a fixed target [42, 43]. The design of the near detector is not finalised, but the current designs favour a mixed technology detector combining a LAr TPC with a larger tracker module. In this work, we will assume that DUNE ND is a LAr detector located at 574 m from the target with a fiducial mass of 50 t [63]. As the trident event rate scales with the density of the target, any tracker module will not significantly influence the total event rate, and does not feature in our estimates; although, its presence is assumed to improve reconstruction of final-state muons. Our estimates can be easily scaled for the final design by using Eq. (3.4.1).

For the first 6 years of data taking (3 years in the neutrino plus 3 years in the antineutrino mode) the collaboration expects 1.83×10^{21} POT/year with a plan to upgrade the beam after the 6th year for 2 extra years in each beam mode with double exposure, making a total of $1.83 \times (3 + 2 \times 2) \times 10^{21}$ POT for each mode [64]. We will assume the total 10-year exposure in our calculations. . as the relevant fluxes at the DUNE ND location (see Fig. **??**). The beam composition of the neutrino (antineutrino) beam is about 96% ν_μ ($\overline{\nu}_\mu$), 4% $\overline{\nu}_\mu$ (ν_μ) and 1% $\nu_e + \overline{\nu}_e$.

The number of trident events for DUNE ND can be found in Tab. 3.2. The numbers in parentheses correspond to antineutrino beam mode. Note that although the trident cross sections are the same for neutrinos and antineutrinos, the fluxes are a bit lower for the antineutrino beam, as a consequence we predict a lower event rate for this beam[10]. Due to the much higher energy and wider energy range of the neutrino fluxes at DUNE ND, as compared to the SBN detectors, DUNE can observe a considerable number of trident events, about 300 times the number of trident events expected for SBND just in the neutrino

---

[10]A similar difference will apply to the processes constituting the background to the trident process, although there is an additional suppression in many channels due to the lower antineutrino cross sections.

mode. Moreover, the subdominant component of each beam mode will also contribute to the signal. For example, we expect to observe 2051 trident events in the $\bar{\nu}_\mu \to \bar{\nu}_e e^- \mu^+$ channel in the antineutrino mode. However, we also expect 235 events in the $\nu_\mu \to \nu_e e^+ \mu^-$ channel produced by the subdominant component of ν_μ in the antineutrino beam. We have considered 100% detection efficiency here, however, we will see in Sec. 3.4.2 that after implementing hadronic vetos, detector thresholds and kinematical cuts to substantially reduce the background we expect an efficiency of about 47%-65% on coherent tridents, depending on the channel (see Tab. 3.4).

The mixed flavour trident channel is the one with the highest statistics (more than 6000 events adding neutrino and antineutrino beam modes), 11% of which are produced by diffractive scattering. The dielectron channel comes next with a total of a bit more than 1900 events, 5% of which are produced by diffractive scattering. Although the dimuon channel is the less copious one, with only about 750 events produced, almost 34% of these events are produced by a diffractive process. This can be understood by recalling our discussions in Sec. 3.3.3.

Finally, we note that a dedicated high-energy run at DUNE has been mooted, to be undertaken after the full period of data collecting for the oscillation analysis. Thanks to the higher energies of the beam, this has the potential to see a significant number of neutrino tridents, provided it can collect enough POTs.

ν**STORM** In this section we study the trident rates for a possible LAr detector for the proposed νSTORM experiment [44, 45]. The νSTORM facility is based on a neutrino factory-like design and has the goal to search for sterile neutrinos and study neutrino nucleus cross sections [65]. Although this proposal is in its early days, νSTORM has the potential to make cross section measurements with unprecedented precision. In its current design, 120-GeV protons are used to produce pions from a fixed target with the pions subsequently decaying into muons and neutrinos. The muons are captured in a storage ring and during repeated passes around the ring they decay to produce neutrinos. Consequently, the storage ring is an intense source of three types of neutrino flavours: ν_μ from π^+ and K^+ decays, which will be more than 99% of the total flux, ν_e and $\bar{\nu}_\mu$ from recirculated muon decays which will comprise less than 1% of the total flux. An important point, however, is that the neutrinos coming from the pion and kaon decays can be separated by event

timing from the ones produced by the stored muons. This distinction allows the ν_μ flux to be studied almost independently from the $\bar{\nu}_\mu$ and ν_e flux. In addition, it implies after the initial flash of meson-derived events, that the flux consists of as many electron neutrinos as muon antineutrinos. We will assume a LAr detector for νSTORM at a baseline of $50\,\mathrm{m}$ with $100\,\mathrm{t}$ of fiducial mass with an exposure of 10^{21} POT. The neutrino fluxes, assuming a central μ^+ momentum of 3.8 GeV/c in the storage ring, are taken from Ref. [45] and are shown in Fig. **??**.

In Tab. 3.2, we show the results of our calculations for νSTORM. More than 97% of the events from the incoming ν_μ are from pion decays and only less than 3% from kaon decays. Since we only consider the decay of mesons with positive charges and we expect neutral and wrong charge contamination to be small, we do not have trident events from incoming $\bar{\nu}_e$. The total number of mixed flavour, dielectron and dimuon channel events is, respectively, 214, 120 and 17, much less than what can be achieved at the larger neutrino energies available at the DUNE ND. The novel flavour structure of the beam does enhance the contribution of ν_e induced tridents with respect to the $\overset{(-)}{\nu_\mu}$ ones, but this contribution only becomes dominant for the e^+e^- tridents in the muon decay events. Finally, we emphasize that the experimental design parameters for νSTORM are far from definite. Increasing the energy of stored muons and the size of the detector are both viable options which could significantly enhance the rates we present.

3.4.2 Background Estimates for Neutrino Trident in LAr

The study of any rare process is a struggle against both systematic uncertainties in the event rates and unavoidable background processes. True dilepton signatures are naturally rare in neutrino scattering experiments, but with modest rates of particle misidentification a non-trivial background arises. In this section we estimate the background to trident processes in LAr and its impact on the trident measurement. We perform our analysis only for DUNE ND, in neutrino and antineutrino mode, but our results are expected to be broadly applicable to other LAr detectors. We have generated a sample of 1.1×10^6 background events using GENIE [46] for incident electron and muon flavour neutrinos and antineutrinos. It is worth noting, however, that this event sample will in fact be smaller than the total number of neutrino interactions expected in the DUNE ND. Our

goal, therefore, will be to demonstrate that with modest analysis cuts background levels can be suppressed significantly such that they become comparable to or smaller than the signals we are looking for. In the absence of events that satisfy our background definition, we argue that the frequency of that type of event is less than one in 1.1×10^6 interactions of the corresponding initial neutrino.

To account for misreconstruction in the detector, we implement resolutions as a gaussian smear around the true MC energies and angles. We assume relative energy resolutions as $\sigma/E = 15\%/\sqrt{E}$ for e/γ showers and protons, and $6\%/\sqrt{E}$ for charged pions and muons. Angular resolutions are assumed to be $1°$ for all particles (proton angles are never smeared in our analysis). The detection thresholds are a crucial part of the analysis, since for many channels one ends up with very soft electrons. We take thresholds to be 30 MeV for muons and e/γ showers kinetic energy, 21 MeV for protons and 100 MeV for $\pi^\pm$ [43].

Background Candidates

We focus on three final-state charged lepton combinations: $\mu^+\mu^-$, $\mu^\pm e^\mp$ and e^+e^-. Genuine production of these states is possible in background processes, but usually rare, deriving from meson resonances or other prompt decays. The majority of the background is expected to be from particle misidentification (misID). We assume that protons can always be identified above threshold and that neutrons leave no detectable signature in the detector. In addition, we require no charge ID capabilities from the detector and assume that the interaction vertex can always be reconstructed. Under these assumptions, we have incorporated three misidentifications which will affect our analysis, and give our naive estimates for their rates in Tab. 3.3. Any other particle pairs are assumed to be distinguishable from each other when needed.

The requirement of no hadronic activity helps constrain the possible background processes, but one is still left with significant events with invisible hadronic activity and other coherent neutrino-nucleus scatterings. These are then reduced by choosing appropriate cuts on physical observables, exploring the discrepancies between our signal and the background. In our GENIE analysis, we include all events that have final-states identical to trident, or that could be interpreted as a trident final-state considering our proposed misID scenarios. Our dominant sources of background for $\mu^+\mu^-$ tridents are ν_μ-initiated charged-current

events with an additional charged pion in the final-state (ν_μCC1$\pi^\pm$). For e^+e^- tridents, the most important processes are neutral current scattering with a π^0 (NCπ^0), while for mixed $e^\pm\mu^\mp$ tridents, the ν_μ-initiated charged-current events with a final-state π^0 (CCπ^0) dominate the backgrounds. In each case, the pion is misidentified to mimic the true trident final-state. Other relevant topologies include charm production, CCγ and ν_eCC$\pi^\pm$. For a detailed discussion of these backgrounds processes we refer the reader to Appendix 3.6.

Estimates for the DUNE ND

In this section we provide estimates for the total background for each trident final-state for the DUNE ND. The number of total inclusive CC interactions in the 50 t detector due to neutrinos of all flavours is calculated to be 5.18×10^8. We scale our background event numbers to match this, and argue that one has to reach suppressions of order $10^{-6} - 10^{-5}$ to have a chance to observe trident events. Whenever our cuts remove all background events from our sample, we assume the true background rate is one event per 1.1×10^6 ν interactions and scale it to the appropriate number of events in the ND, applying the misID rate whenever relevant. Within our framework, this provides a conservative estimate as the true background is expected to be smaller.

Our estimates are shown in Table 3.4. We start with the total number of background candidates N_B^{misID}, using only the naive misID rates shown in Table 3.3. These are much larger than the trident rates we expect, by at least 2 orders of magnitude. Next, we veto any hadronic activity at the interaction vertex, obtaining N_B^{had}. We emphasize that this veto also affects the diffractive tridents in a non-trivial way, and therefore we remain agnostic about the hadronic signature of these. Finally, one can look at the kinematical distributions of coherent trident in Section B.0.1 and try to estimate optimal one dimensional cuts for the DUNE ND based on the kinematics of the final-state charged leptons. This is a simple way to explore the striking differences between the peaked nature of our signal and the smoother background. In a real experimental setting it is desirable to have optimization methods for isolating signal from background, preferably with a multivariate analyses. However, even in our simple analysis, cutting on the small angles to the beamline and the low invariant masses of our trident signal can achieve the desired background suppressions. For the $\mu^+\mu^-$ tridents we show the effect of our cuts in Fig. 3.7. The cuts are defined to

be $m^2_{\mu^+\mu^-} < 0.2$ GeV^2, $\Delta\theta < 20°$, $\theta_\pm < 15°$. The kinematics is very similar in the other trident channels, with slightly less forward distributions for electrons. For the e^+e^- channel we take $m^2_{e^+e^-} < 0.1$ GeV^2, $\Delta\theta < 40°$ and $\theta_\pm < 20°$. The asymmetry between the positive and negative charged leptons is visible in the distributions, where the latter tends to be more energetic. This feature was not explored in our cuts, as it is not significant enough to further improve background discrimination. In the mixed flavour tridents, however, one sees a much more pronounced asymmetry. The muon tends to carry most of the energy and be more forward than the electron, which can make the search for this channel more challenging due to the softness of the electron in the high energy event. Nevertheless, the low invariant masses and forward profiles can still serve as powerful tool for background discrimination, provided the event can be well reconstructed. We assume that is the case here and use the following cuts on the background: $m^2_{e^\pm\mu^\mp} < 0.1$ GeV^2, $\Delta\theta < 20°$, $\theta_e < 40°$ and $\theta_\mu < 20°$. When performing kinematical cuts, we also include the effects of detection thresholds after smearing. For a discussion on the impact of these thresholds on the trident signal see Section B.0.1.

The resulting signal efficiencies due to our cuts and thresholds are shown in the last two columns of Table 3.4. One can see that these are all $\approx 50\%$ or greater for our coherent samples, whilst all background numbers remain much below the trident signal. The diffractive samples are also somewhat more affected by our cuts than the coherent ones. If one is worried about the contamination of coherent events by diffractive ones, then the kinematics of the charged leptons alone can help reduce this, independently of the hadronic energy deposition of the events. For instance, in the case where all $\mu^+\mu^-$ diffractive events appear with no hadronic signature, then after our cuts the diffractive contribution is reduced from 41% to 15% of the total trident signal. This reduction is, however, also subject to large uncertainties coming from nuclear effects. In summary, the set of results above are encouraging, suggesting that the signal of coherent-like trident production is sufficiently unique to allow for its search at near detectors despite naively large backgrounds.

Finally, we comment on some of the limitations of our analysis. The low rate of trident events calls for a more careful evaluation of other subdominant processes that could be easily

---

[11]Despite the fact that many diffractive events will likely deposit hadronic energy in the detector, we quote the efficiency of our cuts on diffractive events with no assumptions on their hadronic signature.
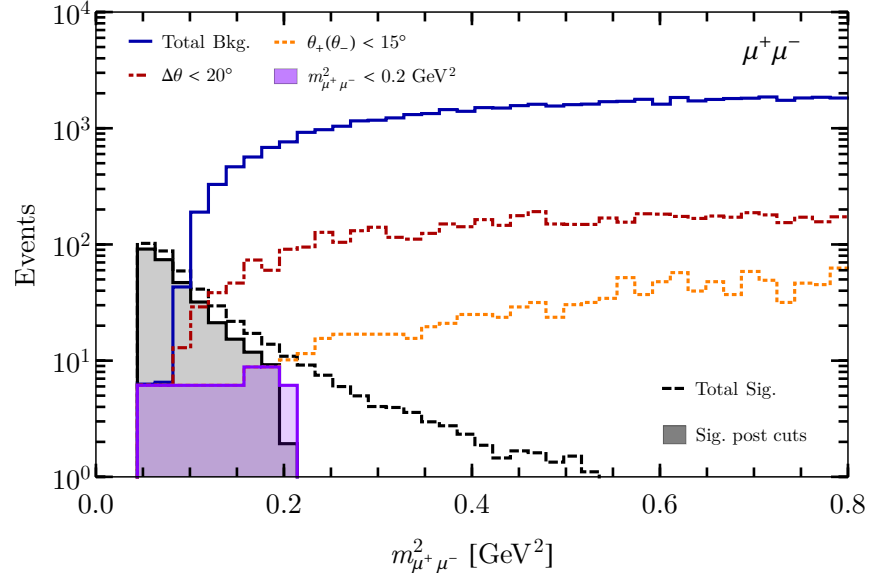
Fig. 3.7. Signal and background distributions in invariant mass. The total background events (blue) include the misID rates in table Table 3.3. We apply consecutive cuts on the background, starting with cuts on the separation angle $\Delta\theta$ (red), both charged lepton angles to the beamline (θ_+ and θ_-) (orange) and the invariant mass $m^2_{\mu^+\mu^-}$. We show the signal samples before and after all the cuts in dashed black and filled black, respectively.

be overlooked. For channels involving electrons, it is possible that de-excitation photons and internal bremsstrahlung become a source of background, as these also produce very soft EM showers, none of which are implemented in GENIE. The question of reconstruction of these soft EM showers, accompanied either by a high energy muon or by another soft EM shower also would have to be addressed, especially in the latter case where a trigger for these soft events would have to be in place. A more complete analysis is also needed for treating the decay products of charged pions and muons produced in neutrino interactions, as well as rare meson decay channels (like the Dalitz decay of neutral pions $\pi^0 \to \gamma e^+ e^-$). Cosmic ray events are not expected to be a problem due to the requirement of a vertex and a correlation with the beam for trident events. Perhaps even more exotic processes, such as the production of three final-state charged leptons ($\nu_\alpha(\bar{\nu}_\alpha) + \mathcal{H} \to \ell^-_\alpha(\ell^+_\alpha) + \ell^+_\beta + \ell^-_\beta + \mathcal{H}'$), can also become relevant. For instance, radiative trimuon production [66] can potentially serve as a background to dimuon tridents if one of the muons is undetected. Similarly, μee production would fake a dielectron (mixed) trident signature if the muon (an electron) is missed. We are not aware of any estimates for the rate of these processes at the DUNE ND, but we note that their rate can be comparable to trident production at energies above 30 GeV [67]. Improvements on our analysis should come from the collaboration's

sophisticated simulations, allowing for a better quantification of hadronic activity, more realistic misID rates and more accurate detector responses.

3.5   Conclusions

Neutrino trident events are predicted by the SM, however, only $\overline{\nu}_\mu$ initiated dimuon tridents have been observed in small numbers, typically fewer than 100 events. This will change in the near future thanks to the current and future generations of precision neutrino scattering and oscillation experiments, which incorporate state-of-the-art detectors located at short distances from intense neutrino sources. In this work we discuss the calculation of the neutrino trident cross section for all flavours and hadronic targets, and provide estimates for the number and distributions of events at 9 current or future neutrino detectors: five detectors based on the new LAr technology (SBND, μBooNE, ICARUS, DUNE ND and νSTORM ND) as well as four more conventional detectors (INGRID, MINOS ND, NOνA ND and MINERνA). The search for tridents, however, need not be exclusive to near detectors of accelerator neutrino experiments. As pointed out by the authors of Ref. [35], atmospheric neutrino experiments can also look for these processes, benefiting from the increase of the cross section at large energies.

We have stressed the need for a full four-body phase space calculation of the trident cross sections without using the EPA. This approximation has been employed in recent calculations and can lead to overestimations of the cross section by 200% or more at the peak neutrino energies relevant for many accelerator neutrino experiments. Moreover, we show why the EPA is not applicable for computing trident cross sections, and provide the first quantitative assessment of this breakdown for coherent and diffractive hadronic regimes. We find that the breakdown of the approximation is most severe for processes with electrons in the final-state and for diffractive scattering of all final state flavours. For coherent dimuon production, the approximation can give a reasonable result at large neutrino energies. This is due to the nuclear form factors that serendipitously suppress those regions of phase space where the EPA is least applicable. We also demonstrated that the best results in this channel are achieved when applying artificial cuts to the phase space. However, even in this case, at energies relevant for the above experiments, the EPA can artificially suppress the coherent scattering contribution and increase the diffractive

one giving rise to an incorrect rate and distributions of observable quantities. For instance, the invariant mass of the charged lepton pair $m_{\ell\ell}^2$ and their angular separation $\Delta\theta$ are more uniformly distributed for diffractive than for coherent trident scattering. Using the correct distributions is crucial to correctly disentangle the signal from the background by cutting on these powerful discriminators.

Our calculations show that DUNE ND is the future detector with the highest neutrino trident statistics, more than 6000 mixed events, 11% produced by diffractive scattering, more than 1900 dielectron events, 5% produced by diffractive scattering and about 750 dimuon events, almost 34% of those produced by a diffractive process. Making use of our efficiencies (see Table 3.4), assuming an ideal background suppression and neglecting systematic uncertainties, we quote the statistical uncertainty on the coherent-like flux averaged cross section for the DUNE ND. We do this for coherent only events and, in brackets, for coherent plus diffractive events, yielding

$$\frac{\delta\langle\sigma^{e^\pm\mu^\mp}\rangle}{\langle\sigma^{e^\pm\mu^\mp}\rangle} = 1.8\,\%\,(1.6\,\%), \quad \frac{\delta\langle\sigma^{e^+e^-}\rangle}{\langle\sigma^{e^+e^-}\rangle} = 3.4\,\%\,(3.3\,\%) \quad \text{and} \quad \frac{\delta\langle\sigma^{\mu^+\mu^-}\rangle}{\langle\sigma^{\mu^+\mu^-}\rangle} = 5.5\,\%\,(5.1\,\%).$$

In this optimistic framework we expect the true statistical uncertainty on coherent-like tridents to lie between the two numbers quoted, depending on how many diffractive events contribute to the coherent-like event sample. This impressive precision would provide unprecedented knowledge of the trident process and the nuclear effects governing the interplay between coherent and diffractive regimes. We emphasize, however, that given these small values for the relative uncertainties, the trident cross section will likely be dominated by systematic uncertainties from detector response and backgrounds which are not modelled here.

For DUNE ND, we have studied the distribution of observables which could help distinguish trident events from the background. We have estimated the background for each trident channel via a Monte Carlo simulation using GENIE, and identified the dominant contributions arising primarily from particle misidentification. We conclude that reaching background rates of the order $\mathcal{O}(10^{-6} - 10^{-5})$ times the CC rate is necessary to observe trident events at DUNE ND, and given the distinctive kinematic behaviour of the trident signal a simple cut-based GENIE-level analysis suggests that this is an attainable goal in a LAr TPC.

Existing facilities may also be able to make a neutrino trident measurement at their near detectors. Despite not including reconstruction efficiencies nor an indication of the impact of backgrounds, we find that the largest trident statistics is available at INGRID, the T2K on-axis near detector. We predict about 660 (1700) events for the mixed flavour, 300 (770) events for the dielectron and 50 (130) events for the dimuon channel for T2K-I (T2K-II). The more fine-grained near detector of MINOS and MINOS+ is also expected to have collected a significant numbers of events during its run. As such, the very first measurement of neutrino trident production of mixed and dielectron channels may be at hand.

3.6   Individual Backgrounds

Here we discuss backgrounds to trident final-states in more detail. We start by motivating our misID rates shown in Table 3.3, and then discuss the dominant background processes individually.

In LAr photons can be distinguished from a single electron if their showers start displaced from the vertex (if present). Photons have a conversion length in LAr of around 18 cm, meaning 5–10% could be expected to convert quickly enough to hinder electron-photon discrimination by this means if the resolution on the gap is from 1–2 cm [68]. Once pair conversion happens, photons can be distinguished from a single electron purely by dE/dx measurements in the first 1–2 cm of their showers. Motivated by the success of this method as shown at ArgoNeuT [68] and based on projections for DUNE [42], we assume that 5% of photons would be taken as $e^{\pm}$ with perfect efficiency, without the need for an event vertex. Needless to say that a dedicated study for trident topologies would be necessary for a more complete study. It is worth noting that our remarks concern only the misID of a single photon for a single electron, whilst the distinction between a photon and an overlapping e^+e^- pair without a vertex can be much more challenging. For this reason we take the misID rate between an overlapping e^+e^- pair and a photon to be 1 in the absence of a vertex.

Charged pions are notorious for faking long muon tracks. We estimate this misID rate as arising from through-going pions, which do not exhibit the decay kink used in their identification. We assume an interaction length of around 1 m, meaning that about 5%

of particles travel ~ 3 meters and escape the fiducial volume. Assuming that this is the most likely way a pion can spoof a muon, we estimate a naive suppression rate of 10^{-2}. In a more complete study, it is desirable to explore the length of the muon and pion tracks inside the detector as a function of energy. The length of the contained tracks can also be an important tool for background suppression which we leave to future studies.

3.6.1 Pion Production

Coherent pion production in its charged ($\nu + A \rightarrow \ell^{\mp} + \pi^{\pm} + A$) and neutral ($\nu + A \rightarrow \nu + \pi^0 + A$) current version is very abundant at GeV energies. The cross section for these processes is modelled in GENIE using a modern version of the Rein-Sehgal model [69, 70]. The charged current version serves mainly as a background to $\mu^+ \mu^-$ tridents, but can also appear as a background for $e^{\pm} \mu^{\mp}$ tridents for incoming electron neutrinos or antineutrinos. It has been studied before at MiniBooNE [71], MINERνA [72, 73], T2K [49, 74], and for the first time in LAr at ArgoNeuT [75]. This process has a very distict low 4-momentum transfer to the nucleus $|t|$ [72], but a much flatter distribution in invariant mass if compared to trident. The neutral current version of coherent pion production serves as a background to $e^+ e^-$ tridents. This process has been studied before by the MiniBooNE [76], SciBooNE [77] and in LAr by the ArgoNeuT collaboration [78]. There are two possibilities for these events to fake an $e^+ e^-$ trident: when one of the gammas produced in the π^0 decay is missed and the other is misIDed for an overlapping $e^+ e^-$ pair, and when both photons are each misIDed for a single electron. This signature also comes with low hadronic activity, but for separated visible photons the invariant mass is a natural discriminator, as in the detector $m_{\gamma\gamma} \approx m_{\pi^0}$.

Resonant pion production can also contribute to trident backgrounds in the absence of any reconstructed protons. Resonant pion production can be larger than its coherent counterpart and is modelled in GENIE by the Rein-Sehgal model [79]. Its CC version was measured by MiniBooNE [71], K2K [80], MINOS [53], and MINERνA [51]. In the latter measurement one can clearly see the large number of events with undetected protons. The misIDed photon and the charged lepton invariant mass are once more flatter than the trident ones, allowing for a kinematical discrimination whenever a single photon is undetected. It is worth noting that these are some of the dominant underlying processes

for pion production in GENIE, but all events leading to topologies relevant for trident are included in our analysis.

3.6.2   Charm Production

Since the first observation of dimuon pairs from charm production in neutrino interaction by the HPWF experiment in 1974 [81], a lot has been learned about these processes (see [82] for a review) in neutrino experiments. Particularly, the production of charm quarks and their subsequent weak decays into muons or electrons have been identified as a major source of background for early trident searches. At the lower neutrino energies at DUNE, however, this is expected to be a smaller yet non-negligible contribution. From our GENIE samples, we estimate that a charmed state is produced at a rate of around $10^{-4}(N_{\mathrm{CC}} + N_{\mathrm{NC}})$. Most of these produce either D mesons, Λ_c or Σ_c baryons. These particles decay in chains, emitting a muon with a branching ratio of around 0.1, and are always accompanied by pions or other hadronic particles. We therefore expect these rates to be negligible with a hadronic veto, and do not consider them further. We hope, however, that future studies will address these channels in more detail.

3.6.3   CCγ and NCγ

The emission of a single photon alongside a CC process could be a background for μe tridents if the photon is misIDed as a single electron. When the photon is produced in a NC event, it can be a background to overlapping e^+e^- tridents. In GENIE, these topologies arise mainly due to resonance radiative decays and from the intra-nuclear processes. For this reason, it usually comes accompanied with extra hadronic activity. For hadronic resonances, we have simulated CC processes in GENIE and estimated the multiplicities: 0.5% single photon and 1% double photon emission from CC rates. Radiative photon production from the charged lepton, on the other hand, does not need to come accompanied by hadrons. It is phase space and $\alpha \approx 1/137$ suppressed with respect to CCQE rates, and therefore could occur at appreciable rates compared to our signal. This contribution, however, is not included in GENIE and is absent from our samples. The rates of internal photon bremsstrahlung have been estimated before, particularly for T2K where a low-energy photon is an important background for electron appearance searches [83],

and as a background to the low energy events at MiniBooNE [84]. De-excitation gammas from the struck nuclei can also generate CCγ or NCγ topologies [85]. These contributions for Ar are not included in GENIE, but are expected to come with a distinct energy profile, which can be tagged on.

Channel	SBND	μBooNE	ICARUS	DUNE ND	νSTORM ND
$\nu_\mu \to \nu_e e^+ \mu^-$	10	0.7	1	2844 (235)	159
	1	0.08	0.1	369 (33)	18
$\overline{\nu}_\mu \to \overline{\nu}_e e^- \mu^+$	0.4	0.02	0.04	122 (2051)	23
	0.04	0.003	0.004	16 (262)	3
$\nu_e \to \nu_\mu e^- \mu^+$	0.05	0.003	0.004	22 (7)	9
	0.008	0.0005	0.0008	5 (1)	2
$\overline{\nu}_e \to \overline{\nu}_\mu e^+ \mu^-$	0.005	0.0003	0.0005	5 (14)	–
	0.001	0.0001	0.0001	1 (3)	–
Total $e^\pm \mu^\mp$	10	0.7	1	2993 (2307)	191
	1	0.1	0.1	391 (299)	23
$\nu_\mu \to \nu_\mu e^+ e^-$	6	0.4	0.7	913 (58)	73
	0.2	0.04	0.02	57 (5)	3
$\overline{\nu}_\mu \to \overline{\nu}_\mu e^- e^+$	0.2	0.01	0.02	34 (695)	9
	0.01	0.001	0.002	2 (41)	0.5
$\nu_e \to \nu_e e^- e^+$	0.2	0.01	0.02	50 (13)	32
	0.01	0.001	0.002	4 (1)	2
$\overline{\nu}_e \to \overline{\nu}_e e^+ e^-$	0.02	0.001	0.002	10 (34)	–
	0.0009	0.0001	0.0002	1 (2)	–
Total $e^+ e^-$	6	0.4	0.7	1007 (800)	114
	0.2	0.0	0.02	64 (49)	6
$\nu_\mu \to \nu_\mu \mu^+ \mu^-$	0.4	0.03	0.04	271 (32)	9
	0.3	0.03	0.04	135 (14)	5
$\overline{\nu}_\mu \to \overline{\nu}_\mu \mu^- \mu^+$	0.01	0.001	0.001	14 (177)	2
	0.01	0.0009	0.001	7 (93)	1
$\nu_e \to \nu_e \mu^+ \mu^-$	0.002	0.0001	0.0001	1 (0.5)	0.4
	0.001	0.0001	0.0001	0.5 (0.2)	0.2
$\overline{\nu}_e \to \overline{\nu}_e \mu^+ \mu^-$	0.0002	0.0000	0.0000	0.3 (0.9)	–
	0.0001	0.0000	0.0000	0.1 (0.3)	–
Total $\mu^+ \mu^-$	0.4	0.0	0.0	286 (210)	11
	0.3	0.0	0.0	143 (108)	6

Tab. 3.2. Total number of **coherent** (top row) and **diffractive** (bottom row) trident events expected at different LAr experiments for a given channel. The numbers in parentheses are for the antineutrino running mode, when present. These calculations considered a detector efficiency of 100%.

misID	Rate
γ as $e^{\pm}$	0.05
γ as $e^{+}e^{-}$	0.1 (w/ vertex)
	1 (no vertex + overlapping)
$\pi^{\pm}$ as $\mu^{\pm}$	0.1

Tab. 3.3. Assumed misID rates for various particles in a LAr detector. We take these values to be constant in energy.

Channel	$\mathbf{N}_{\mathrm{B}}^{\mathrm{misID}}/\mathbf{N}_{\mathrm{CC}}$	$\mathbf{N}_{\mathrm{B}}^{\mathrm{had}}/\mathbf{N}_{\mathrm{CC}}$	$\mathbf{N}_{\mathrm{B}}^{\mathrm{kin}}/\mathbf{N}_{\mathrm{CC}}$	$\epsilon_{\mathrm{sig}}^{\mathrm{coh}}$	$\epsilon_{\mathrm{sig}}^{\mathrm{dif}}$ [11]
$e^{\pm}\mu^{\mp}$	$1.67\,(1.62)\times 10^{-4}$	$2.68\,(4.31)\times 10^{-5}$	$4.40\,(3.17)\times 10^{-7}$	0.61 (0.61)	0.39 (0.39)
$e^{+}e^{-}$	$2.83\,(4.19)\times 10^{-4}$	$1.30\,(2.41)\times 10^{-4}$	$6.54\,(14.1)\times 10^{-6}$	0.48 (0.47)	0.21 (0.21)
$\mu^{+}\mu^{-}$	$2.66\,(2.73)\times 10^{-3}$	$10.4\,(9.75)\times 10^{-4}$	$3.36\,(3.10)\times 10^{-8}$	0.66 (0.67)	0.17 (0.16)

Tab. 3.4. Reduction of backgrounds at the DUNE ND in neutrino (antineutrino) mode and its impact on the signal for each distinguishable trident final-state. $\mathbf{N}_{\mathrm{B}}^{\mathrm{misID}}$ stands for total backgrounds to trident after only applying misID rates, $\mathbf{N}_{\mathrm{B}}^{\mathrm{had}}$ are the backgrounds after the hadronic veto, and $\mathbf{N}_{\mathrm{B}}^{\mathrm{kin}}$ reduce the latter with detection thresholds and kinematical cuts (see text for the cuts chosen). These quantities are normalized to the total number of CC interactions in the ND $\mathbf{N}_{\mathrm{CC}}$ (flavour inclusive). We also show the impact of our detection thresholds and kinematical cuts on the trident signal via efficiencies for coherent only ($\epsilon_{\mathrm{sig}}^{\mathrm{coh}}$) and diffractive only samples ($\epsilon_{\mathrm{sig}}^{\mathrm{dif}}$). We do not cut on the hadronic activity of diffractive events.

Chapter 4

New fundamental forces at DUNE

4.1 Introduction

The discovery of neutrino oscillation is the first laboratory-based proof of physics Beyond the Standard Model (BSM) establishing that, in contrast to the predictions of the Standard Model (SM), the neutrino sector has at least three mass eigenstates distinct from the flavour states defined by the charged-leptons. However, the mechanism which generates neutrino masses remains unknown and many competing candidate theories exist, ranging from the simplicity of a Dirac mass term protected by a symmetry (see *e.g.* [86–88]) or the popular see-saw mechanisms [89–97] to proposals with a more elaborate spectrum of particles. In general, more elaborate scenarios have additional motivations, including the explanation of lepton mass and flavour hierarchies (see *e.g.* [98]), the matter-antimatter asymmetry of the universe [99–101], the existence of dark matter [102, 103], the scale of neutrino masses [104–106] or anomalous experimental results [107]. Uncovering the nature of new physics in the neutrino sector, and its connection to other BSM concerns, will be a central aim of the experimental and theoretical programs over the next few decades.

Although significant progress has already been made, the neutrino sector remains relatively poorly explored. There are still large uncertainties on the masses and on some of the mixing parameters of the light neutrinos [108], but even beyond the effects of neutrino mass, many SM cross sections are poorly known theoretically and infrequently measured. This is in part due to the typical energy scales of neutrino experiments which necessitate the modelling of the neutrino-nucleus interactions, but also because of the rareness of neutrino scattering (see Ref. [109]). Much effort has gone into measuring crucial cross sections at oscillation experiments [48, 110, 111] and at the Main Injector Experiment for ν-A (MINERνA) [112], a dedicated cross section experiment. However, given the necessity and potential richness of BSM physics in the neutrino sector, and the wide array of measurements yet to be made, it is conceivable that new physics will also manifest itself as detectable signatures in neutrino scattering. It is crucial to keep an open mind about what future experimental work might find, for instance, in the auxiliary physics program of the Near Detector (ND) of the next-generation Deep Underground Neutrino Experiment (DUNE) [113].

Novel interactions in the neutrino sector have been proposed for a variety of reasons, including as a potentially observable effect in the neutrino oscillation probabilities (see *e.g.* [114]), as a way of ameliorating tension introduced by sterile neutrinos in the early

universe [115–122], and as a possible explanation of anomalous results at short baseline [13, 123, 124]. Models which introduce new interactions between neutrinos and matter have been discussed in simplified settings [125–127], via Effective Field Theory [37, 128] and specific UV complete models [129] (see also [130] for a neutrinophilic Z' study at the DUNE ND). One class of models restricts the new interactions to leptons. This arises most naturally in settings with a gauged subgroup of lepton number, with most attention given to the anomaly free subgroups $L_\alpha - L_\beta$ for $\alpha, \beta \in \{e, \mu, \tau\}$ [131, 132]. Such leptophilic interactions must satisfy strong constraints from processes involving charged-leptons [6], but in the case of a gauged $L_\mu - L_\tau$ symmetry, neutrino processes have been found to be particularly competitive [11].

In this work, we study potential constraints which can be placed on a general set of leptophilic Z' models in the two most likely scattering channels for this type of BSM at the near detector of DUNE: $\nu - e$ scattering and $\nu\ell\ell$ trident scattering. During ten years of running, a 75-t near detector subjected to the intense neutrino beam at the Long-Baseline Neutrino Facility (LBNF) will provide tens of thousands of $\nu - e$ scattering events. The cross section for this process is theoretically well understood and can therefore be a sensitive probe of BSM physics. Additionally, this process has received special interest due to its potential in reducing systematic uncertainties in the neutrino flux [133, 134], an undertaking which can be affected by new physics. Despite not being a purely leptonic process, neutrino trident production can also be measured with reasonable precision at DUNE, where hundreds of coherent and diffractive trident events are expected at the ND [135]. We study the neutral current channels with dielectron or dimuon final states, pointing out how the new physics contribution impacts the non-trivial kinematics of these processes. The main advantage in such measurements lies on the flavour structure of dimuon tridents, which can be used to constrain otherwise difficult to test models, such as the one where a new force is associated to the $L_\mu - L_\tau$ gauge symmetry [11].

Although these processes can place stringent bounds on many classes of mediators, many scenarios are already heavily constrained through other experimental work. A recent study of several different $U(1)_X$ models using $\nu - e$ scattering was presented in Ref. [21], where data from past $\nu - e$ experiments CHARM-II, GEMMA and TEXONO has been used to put bounds on the couplings and masses of general Z's. Novel charged particles are typically

constrained to be very massive, leading to little enhancement of the charged current neutrino scattering rates. In particular, charged scalars have been considered in $\nu\ell\ell$ trident scattering in Ref. [36], where it is found that trident measurements can provide competitive bounds on charged scalars, albeit only in simplified theoretical settings. The requirement of doubly charged scalars or the connection to neutrino masses introduced by the typical UV completions of such models dilutes the relevance of the trident bounds. Neutral scalars are viable, but also present challenging UV completions. Novel Z' interactions in $\nu\ell\ell$ trident scattering with dimuon final states have been studied in Ref. [11], where it was shown to be a promising channel to probe a $L_\mu - L_\tau$ gauge symmetry. This model was revisited in Refs. [9] and [136], where the effects of kinetic mixing and the possibility of a measurement by T2K was alluded to. Finally, neutrino trident scattering with atmospheric neutrinos was shown to be sensitive to this model as well as to simplified scalar models in [137]. It should be noted, however, that as it was shown in Ref. [135] the Equivalent Photon Approximation (EPA) discussed in several recent studies [9, 36] for the calculation of the trident cross section leads to intolerably large errors in the predictions for the $\nu\ell\ell$ scattering channels in the SM. For this reason, we calculate this process without making this approximation.

The structure of the paper is as follows. In Section 4.2, we describe the basic properties of the leptophilic scenarios that we will consider in this work. In Section 4.3, we discuss the calculation of the trident and $\nu - e$ scattering cross sections in a general model of leptophilic Z'. In Section 4.4, we show how DUNE can place bounds on a few popular leptophilic Z' models, discussing our assumptions for experimental configurations and backgrounds. We make our concluding remarks in Section 4.5.

4.2 Leptophilic Z' models

Since we are interested in models where the novel neutral currents are present only in the lepton sector, let us consider explicitly a U(1)$_{Z'}$ extension of the SM whose Lagrangian is given by

$$\mathcal{L} \supset -g' Z'_\mu \left[Q^{\mathrm{L}}_\alpha \, \overline{L^\alpha_L} \gamma^\mu L^\alpha_L + Q^{\mathrm{R}}_\alpha \, \overline{\ell^\alpha_R} \gamma^\mu \ell^\alpha_R + \sum_{\mathrm{N}} Q_{\mathrm{N}} \, \overline{N_R} \gamma^\mu N_R \right], \tag{4.2.1}$$

where L_α (ℓ_α) represents the leptonic SU(2) doublet (singlet) of flavour $\alpha \in \{e, \mu, \tau\}$, and we included N right-handed neutrinos with charges Q_{N} under the new symmetry for

completeness. Thus, we have $7 + N$ new parameters to characterize the couplings between the new boson and the lepton sector, one gauge coupling g' and $6+N$ charges $\{Q_\alpha^L, Q_\alpha^R, Q_N\}$. Below the scale of the Electroweak Symmetry Breaking (EWSB), the relevant interaction terms in the Lagrangian are given by

$$\mathcal{L} \supset -g' Z'_\mu [Q_\alpha^L \, \overline{\nu_\alpha} \gamma^\mu P_L \nu_\alpha + \frac{1}{2} \overline{\ell_\alpha} \gamma^\mu (Q_\alpha^V - Q_\alpha^A \gamma^5) \ell_\alpha$$
$$+ \sum_N Q_N \, \overline{N_R} \gamma^\mu N_R], \tag{4.2.2}$$

where $Q_\alpha^V \equiv Q_\alpha^L + Q_\alpha^R$ and $Q_\alpha^A \equiv Q_\alpha^L - Q_\alpha^R$. We note that the right-handed singlets could modify the form of the neutrino interaction in Eq. (4.2.2) by introducing a right-chiral current. The details of this would depend on the relationship between these chiral states and the flavour-basis neutrino ν_α. However, in practice our Lagrangian is fully general, as the polarization effects in the neutrino beam ensure that only the left-handed charge is relevant for light-neutrino scattering experiments.

The Lagrangian in Eq. (4.2.1) contains all of the terms necessary for this analysis. However, when it comes to assigning specific charges to the particles, a few wider model-building considerations are worthy of discussion. In the SM, any non-vectorial symmetry would forbid the Yukawas responsible for the charged-lepton mass terms post-ESWB; similarly, possible negative implications for neutrino mass generation are expected. The precise implementation of the neutrino mass mechanism is highly model dependent, but neutrino gauge charges are not compatible with many usual realizations[1]. Furthermore, the novel gauge boson Z' will also require a mass generation mechanism, and indeed this could be achieved via the means of symmetry breaking. Although each of these is an important aspect of model building, their resolution can be expected to have little impact on the phenomenology of neutrino scattering, and we will not pursue them here. Anomaly freedom of our new symmetry, however, is a more pertinent concern. It has been shown that an anomalous group can always be made anomaly free via the introduction of exotically charged sets of fermions which can be given arbitrarily large masses [138]. Yet these novel fermionic states necessarily introduce effects at low-scales, which in some cases can strongly affect the phenomenology of the model [139]. Therefore, while it seems likely that mass generation can be addressed with the addition of new particles which do not interfere with

---

[1]If neutrino masses are thought of as coming from a Weinberg operator, it is clear that the leptonic doublet must be uncharged under any unbroken $U(1)'$ group.

neutrino scattering phenomenology, anomaly freedom is more pernicious. For this reason we will briefly discuss how anomaly freedom will dictate the types of leptonic symmetries that we consider in the remainder of this work.

Anomaly freedom.   The most general anomaly-free symmetries compatible with the SM were first deduced in the context of Grand Unification Theories (GUT) [140,141]. More recently, an atlas of all anomaly-free $U(1)$ extensions of the SM with flavour-dependent charges has been provided by Ref. [142]. Interestingly, the only anomaly-free subgroups of the SM with renormalisable Yukawa sector are leptophilic: the lepton-family number differences $L_\alpha - L_\beta$ ($\alpha, \beta = e, \mu, \tau$) [131, 132]. The popular $B - L$ symmetry is in fact anomalous unless right-handed SM singlets are added with the appropriate charges. This is well motivated by the necessity of neutrino mass generation but remains a hypothesis, as not all models of neutrino mass require novel fermionic content. For the sake of discussion, we follow a similar logic and consider the most general anomaly free subgroups of the SM accidental leptonic symmetries allowing for an arbitrary number of right-handed fermionic singlets. These would presumably be associated with the neutrino mass generation mechanism, but we impose no specific relations in this regard due to the significant model-building freedom. The anomaly conditions for a leptophilic model with right-handed neutrinos are given below [143] [2]

$$\mathrm{SU(2)_W^2 \times U(1)_{Z'}} \quad \sum_\alpha Q_\alpha^\mathrm{L} = 0, \tag{4.2.3a}$$

$$\mathrm{U(1)_Y^2 \times U(1)_{Z'}} \quad \sum_\alpha \left[\frac{1}{2}Q_\alpha^\mathrm{L} - Q_\alpha^\mathrm{R}\right] = 0, \tag{4.2.3b}$$

$$\mathrm{U(1)_Y \times U(1)_{Z'}^2} \quad \sum_\alpha \left[(Q_\alpha^\mathrm{L})^2 - (Q_\alpha^\mathrm{R})^2\right] = 0, \tag{4.2.3c}$$

$$\mathrm{U(1)_{Z'}^3} \quad \sum_\alpha \left[2(Q_\alpha^\mathrm{L})^3 - (Q_\alpha^\mathrm{R})^3\right] - \sum_\mathrm{N} Q_\mathrm{N}^3 = 0, \tag{4.2.3d}$$

$$\text{Gauge-Gravity} \quad \sum_\alpha \left[2Q_\alpha^\mathrm{L} - Q_\alpha^\mathrm{R}\right] - \sum_\mathrm{N} Q_\mathrm{N} = 0. \tag{4.2.3e}$$

In the absence of new N_R particles ($Q_\mathrm{N} = 0$) and assuming that $Q_\alpha^\mathrm{L} = Q_\alpha^\mathrm{R}$, that is considering vector couplings, we find the three well-known discrete solutions for the Eqs. (4.2.3): the antisymmetric pairs $L_\alpha - L_\beta$, $\alpha, \beta = \{e, \mu, \tau\}$, $\alpha \neq \beta$. As far as anomalies are concerned,

---

[2]Notice that $\mathrm{U(1)_{Z'}^3}$ together with gauge-gravity conditions imply that the number of right-handed states must be at least $N = 3$.

all three pairs are equal, but frequently focus falls on $L_\mu - L_\tau$, which has no coupling to electrons and correspondingly weaker constraints. If we reconsider these conditions with charged right-handed neutrinos, we find a one dimensional continuous family of potential symmetries which can be consistently gauged. We can parametrise this as

$$\varrho(L_\alpha - L_\beta) + \vartheta(L_\beta - L_\lambda), \tag{4.2.4}$$

with

$$3\varrho\,\vartheta(\vartheta - \varrho) = \sum_N Q_N^3. \tag{4.2.5}$$

What we have shown is that linear combinations of the $(L_\alpha - L_\beta)$ choice of charges yield an anomaly free scenario provided N right-handed neutrinos respecting Eq. (4.2.5) are added to the theory. We have checked that the "anomaly-free atlas" in [144] contains a subset of these solutions, which are more general.

The above conclusions are based on the assumption of vectorial charge assignments. In the SM, this requirement is a consequence of the origin of mass assuming a chargeless Higgs. However, in non-minimal models this requirement could be relaxed. Even with this extra freedom, not all charge assignments are allowed: for example, a purely chiral $U(1)'$ cannot satisfy Eq. (4.2.3c) without additional matter charged under the SM gauge group. The axial-vector case, however, does have further solutions: we find that the same one-dimensional family of charges is allowed as for the vectorial gauge boson — in this case, the charges apply to the left-handed fields and the right-handed ones have the opposite charges. In such a model the leptonic mass generation mechanism would necessarily be more complicated than in the SM, but such a possibility is not excluded. UV completions of an axial-vector Z' have been presented in [145, 146], however, these generally introduce extra bounds that are expected to be stronger than neutrino scattering bounds (see *e.g.* [139, 147]). For this reason, we only comment on the consequences of an axial-vector case in our calculations, but do not develop any particular model or constraint.

Kinetic mixing.   The symmetries of our SM extensions allow for kinetic mixing between the Z' and the SM gauge bosons [148–150]

$$\mathcal{L}_{\text{mix}} = -\frac{\varepsilon}{2} F_{\kappa\rho} F'^{\,\kappa\rho}, \tag{4.2.6}$$

where $F_{\kappa\rho}$ and $F'^{\kappa\rho}$ are the field strength tensors of the hypercharge and the Z' boson, respectively. The presence of such coupling introduces a very rich phenomenology and has been explored in great detail in the literature [151]. In this work, we choose to focus on the less constrained possibility of vanishing tree-level kinetic mixing. In this case, kinetic mixing is still radiatively generated due to the presence of particles charged under both the SM and the new $U(1)$ group. As well as the SM particle content, additional particles present in the UV theory may also contribute to kinetic mixing, but we will neglect these contributions in this study as they are highly model dependent [3]. We compute ε between the Z' and the SM *photon*, and find the one-loop result to be finite for any $\varrho(L_\alpha - L_\beta) + \vartheta(L_\beta - L_\lambda)$ gauge group, with divergences cancelling between families. In particular, for the $L_\mu - L_\tau$ model our result is in agreement with Refs. [12, 136]

$$
\begin{aligned}
\varepsilon(q^2) =& \frac{eg'}{2\pi^2} \int_0^1 \mathrm{d}x\, x(1-x) \ln \frac{m_\mu^2 - x(1-x)q^2}{m_\tau^2 - x(1-x)q^2} \\
& \xrightarrow{q^2 \to 0} \frac{eg'}{12\pi^2} \ln \frac{m_\mu^2}{m_\tau^2}.
\end{aligned}
\tag{4.2.7}
$$

Note that the finiteness of the one-loop result has important consequences for the leptophilic theories we consider. As pointed out in Ref. [6], the finiteness of ε implies that one is able to forbid tree-level kinetic mixing, albeit in a model dependent manner. This happens, for instance, when embedding the new leptophilic $U(1)$ group in a larger non-abelian group G, which is completely independent from the SM sector. This choice of one-loop generated kinetic mixing should be seen as a conservative choice; in the absence of cancellation between tree and loop-level kinetic mixing, this yields the least constrained scenario for an $L_\mu - L_\tau$ model. Additional constraints from first-family leptons are now relevant [149, 152], especially $\nu - e$ scattering measurements, where the strength of the constraint makes up for the loop suppression in the coupling. For neutrino trident scattering, one can safely ignore loop-induced kinetic mixing contributions in the calculation since these are either smaller than the tree-level new physics contribution or yield very weak bounds compared to other processes.

We emphasize that if accompanied by a consistent mechanism for the generation of the Z' mass terms and leptonic Yukawa terms, the models we consider constitute a UV complete

---

[3] The authors of Ref. [12] have calculated the contribution to kinetic mixing in the $L_\mu - L_\tau$ model from a pair of scalars with opposite charges. These are typically subdominant, provided the mass hierarchy between the two scalars is not much larger than that of the charged leptons.

extension of the SM. The treatment of such scenarios lies beyond the scope of this work, but we note that if their scalar sectors are light enough they can also yield rich phenomenology at low scales [153].

4.3   Signatures of leptonic neutral currents

When a neutrino impinges on a detector it has only two options for BSM scattering via a leptophilic mediator. In the simplest scenario, the neutrino interacts via the new mediator with the electrons of the detection medium. In this case, there is a tree-level $\nu - e$ scattering process which would be expected to show the clearest signs of new physics. For scattering off a hadron, however, the leptophilic nature of the mediator means that the first tree-level contribution will necessarily come from a diagram which also includes at least one additional SM mediator. Any neutrino-hadron scattering process can be embellished with the new boson to create a BSM signature. In general, the final states of these processes will be either identical to the original un-embellished process (perhaps with missing energy) or it will have an extra pair of leptons in the final state. These neutrino trilepton production processes, which we will refer to as tridents for simplicity, can be subdivided into four types:

- $\ell\ell\ell$ trident: $\mathcal{H} + \nu_\alpha \rightarrow \mathcal{H}' + \ell_\alpha^- + \ell_\beta^+ + \ell_\beta^-$

- $\nu\ell\ell$ trident: $\mathcal{H} + \nu_\alpha \rightarrow \mathcal{H} + \nu_\beta + \ell_\gamma^+ + \ell_\delta^-$

- $\nu\nu\ell$ trident: $\mathcal{H} + \nu_\alpha \rightarrow \mathcal{H}' + \ell_\alpha^- + \nu_\beta + \overline{\nu}_\beta$

- $\nu\nu\nu$ trident: $\mathcal{H} + \nu_\alpha \rightarrow \mathcal{H} + \nu_\alpha + \nu_\beta + \overline{\nu}_\beta$

We note that these processes all occur in the SM, and so the hunt for new physics will necessarily be competing against a background of genuine SM events. Moreover, for final states with missing energy in the form of neutrinos, isolating a BSM signal would necessarily rely on spectral measurements and other backgrounds have the potential to be large. In particular, the trident production of $\nu\nu\nu$ and $\nu\nu\ell$ will be seen as contributions to the neutral-current (NC) elastic and charged-current quasi-elastic (CCQE) processes, and we expect backgrounds to be insurmountable (see *e.g.* Ref. [154] for new physics contributions to CCQE processes). The $\ell\ell\ell$ channels, on the other hand, are expected to

Bethe-Heitler   Dark-Bremsstrahlung
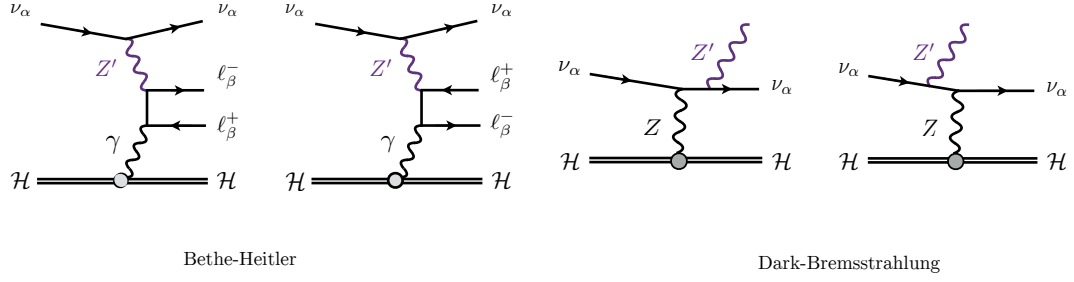
Fig. 4.1. The BSM contributions to neutrino trident production considered in our calculation. The diagrams on the left are referred to as Bether-Heitler contributions due to their resemblance to pair-production. On the right, we show diagrams with a radiative-like Z' emission, which allows for the production of on-shell Z' particles, which subsequently decays into a charged-lepton pair.

have a much more manageable SM background. Trimuon production, for instance, has been measured in the past and provides a multitude of kinematical observables in the final state [155, 156]. The SM rate for this channel contains radiative photon diagrams as well as hadronic contributions [157–159], whilst for leptophilic neutral bosons, the dominant contributions comes from a weak process with initial and final state radiation of a Z', making it a less sensitive probe of light new physics. Finally, the $\nu\ell\ell$ production, the most discussed trident signature in the literature, has already been observed in the dimuon channel [10, 30, 160]. This channel is by far the most important trident process for our study, as the leptonic subdiagrams contain only weak vertices in the SM.

4.3.1   Neutrino trident scattering

In the $\nu\ell\ell$ neutrino trident scattering, an initial neutrino scatters off a hadronic target producing a pair of charged leptons in the process. Since we focus solely on neutral current processes and on flavour conserving new physics, no mixed flavour tridents are relevant and we can write

$$\mathcal{H}(P) + \nu_\alpha(p_1) \to \mathcal{H}(P') + \nu_\alpha(p_2) + \ell_\beta^-(p_3) + \ell_\beta^+(p_4).$$

In the SM this process receives CC and NC contributions when $\alpha = \beta$, and is a purely NC process if $\alpha \neq \beta$. The BSM contributions to trident production we consider are shown in Fig. 4.1. Beyond computing the Bethe-Heitler (BH) contributions considered previously, we show that radiative contributions to these processes are generally small. Using the

Narrow-Width-Approximation (NWA), we compute the cross section for the radiation of a Z' particle from a neutrino-nucleus interaction, which can then promptly decay to an $\ell^+\ell^-$ pair. We call these contributions Dark-Bremsstrahlung (DB) processes for their similarity with electron brehmsstrahlung in QED. We now discuss the two amplitudes individually.

Bethe-Heitler. The BH amplitude can be written as follows

$$\mathcal{M}_{\mathrm{BH}} = \frac{\mathrm{L}_\mu \, \mathrm{H}_{\mathrm{EM}}^\mu}{Q^2}\,, \tag{4.3.1}$$

where $Q^2 \equiv -q^2 = (P - P')^2$ is the momentum transfer and $\mathrm{H}_{\mathrm{EM}}^\mu$ the hadronic amplitude for coherent or diffractive electromagnetic scattering

$$\mathrm{H}_{\mathrm{EM}}^\mu \equiv \langle \mathcal{H}(P) | J_{\mathrm{EM}}^\nu(q^2) | \mathcal{H}(P') \rangle\,. \tag{4.3.2}$$

We refer the reader to Ref. [135] for the details on the treatment of the hadronic amplitude. The leptonic amplitude for NC scattering L_μ reads

$$
\begin{aligned}
\mathrm{L}_\mu \equiv -\frac{ieG_F}{\sqrt{2}} & [\bar{u}(p_2)\gamma^\tau(1-\gamma_5)u(p_1)] \\
& \times \bar{u}(p_4)\left[\gamma_\tau(\hat{V}_{\alpha\beta} - \hat{A}_{\alpha\beta}\gamma_5)\frac{1}{(\slashed{q} - \slashed{p}_3 - m_3)}\gamma_\mu \right. \\
& \left. + \gamma_\mu \frac{1}{(\slashed{p}_4 - \slashed{q} - m_4)}\gamma_\tau(\hat{V}_{\alpha\beta} - \hat{A}_{\alpha\beta}\gamma_5)\right]v(p_3)\,.
\end{aligned}
\tag{4.3.3}
$$

In writing the equation above, we have introduced effective vector and axial couplings containing SM and BSM contributions

$$\hat{V}_{\alpha\beta} = g_V^{\ell_\beta} + \delta_{\alpha\beta} + \frac{Q_\alpha^L Q_\beta^V}{2\sqrt{2}G_F}\frac{(g')^2}{K^2 + M_{Z'}^2}\,, \tag{4.3.4a}$$

$$\hat{A}_{\alpha\beta} = g_A^{\ell_\beta} + \delta_{\alpha\beta} + \frac{Q_\alpha^L Q_\beta^A}{2\sqrt{2}G_F}\frac{(g')^2}{K^2 + M_{Z'}^2}\,, \tag{4.3.4b}$$

where $K^2 = -(p_1 - p_2)^2$ and $g_V^{\ell_\beta}$'s ($g_A^{\ell_\beta}$'s) are the SM vector (axial) couplings. Note the dependence on the positive kinematic variable K^2 in the BSM contribution, which can lead to a significant peaked behaviour in the cross section. To avoid numerical difficulties, we have modified the phase space treatment proposed in [161, 162], as shown in Appendix **??**.

Dark-Bremsstrahlung. Due to the small decay width of the Z' ($\Gamma \propto g'^2 M_{Z'}$), one can obtain an estimate for its resonant production using the NWA. In the true narrow-width

limit, this process reduces to a 3-body phase space calculation and does not interfere with the BH amplitude [4]. Our DB amplitude for $\nu_\alpha(k_a) + \text{A}(k_b) \to \nu_\alpha(k_1) + Z'(k_2) + \text{A}(k_3)$ reads

$$\mathcal{M}_{\text{DB}} = g' Q_\alpha^L \frac{G_F}{\sqrt{2}} J_\mu \text{H}_\text{W}^\mu, \tag{4.3.5}$$

where H_W^μ is the weak hadronic current (see Appendix **??**) and

$$
\begin{aligned}
J_\mu =& \overline{u}(k_1) \Big[\gamma^\alpha \frac{k\!\!\!/_1 + k\!\!\!/_2}{(k_1 + k_2)^2} \gamma_\mu \\
&+ \gamma_\mu \frac{k\!\!\!/_a - k\!\!\!/_2}{(k_a - k_2)^2} \gamma^\alpha \Big] (1 - \gamma^5) u(k_2)\, \epsilon_\alpha^*(k_2),
\end{aligned} \tag{4.3.6}
$$

where $\epsilon_\alpha^*(k_2)$ is the polarization vector of the Z'. The previous amplitude can then be squared and integrated over phase-space for the total DB cross section. The different charged lepton final states can then be imposed with their respective branching ratios (BR). As a final remark, we note that the typical decay lengths of the new boson are typically below 1 cm for the parameter space of interest, such that their decay is indeed prompt.

From the previous discussions it is clear that the contributions to the total cross section at the lowest order in g' come from the interference between the BSM and the SM BH diagrams, and from the DB. The latter, however, contains an extra power of G_F and is expected to be subdominant with respect to the BH interference. Our results for the individual flux integrated cross sections are shown in Fig. 4.2 for the $\mu^+\mu^-$ and in Fig. 4.3 for the e^+e^- trident channels. We show the BH contributions as well as the DB one normalized by the SM trident cross section. All cross sections are flux integrated using the 62.4 GeV p^+ DUNE flux described in Section 4.4.1. For generality, we do not include the BR factors in the DB contributions, and so the green lines only apply for $\mu^+\mu^-$ tridents if $M_{Z'} > 2m_\mu$ and would suffer additional suppression due to the BR. In each figure we show two panels, one for vector couplings and one for axial-vector couplings. This is interesting from a purely computational point of view, as it shows explicitly the BH cross section scaling with the $M_{Z'}$ in the two cases. Whilst the scaling is similar for dielectron tridents, it differs significantly between the vector and axial-vector cases of the dimuon

---

[4]We note that despite the fact that interference terms between resonant and non-resonant contributions vanish in the narrow-width limit, the errors induced by the NWA can no longer be shown to be of the order of $\Gamma_{Z'}/M_{Z'}$ [163]. Nevertheless, we do not expect a more careful evaluation of the resonant contribution to change our conclusions.
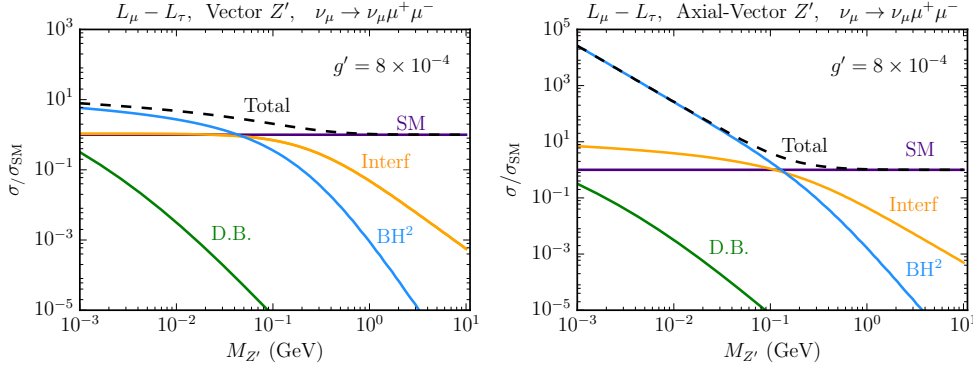
Fig. 4.2.   Flux integrated cross sections normalized to the flux integrated SM trident cross section for dimuon production. On the left (right) panel we show the vector (axial-vector) Z' case. We separate the different contributions: SM only, interference between SM and BSM Bethe-Heitler contributions (interf) and BSM Bethe-Heither only (BH^2). The Dark-Bremsstrahlung (DB) cross section is also shown, but does not take the branching ratio into final state charged leptons into account.
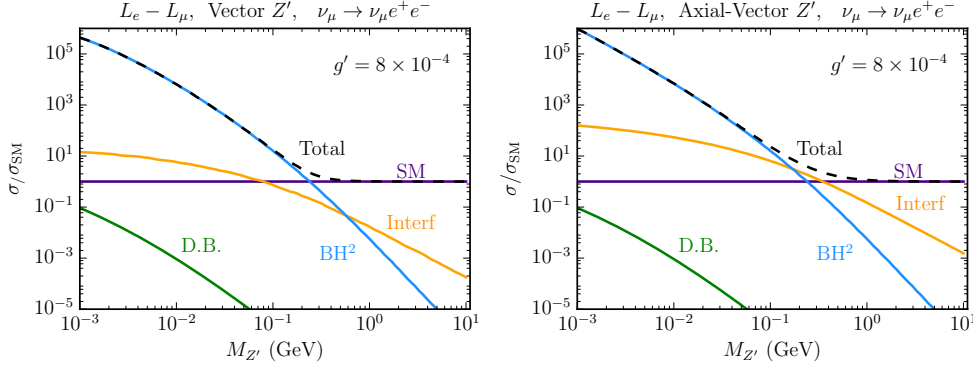
Fig. 4.3.   Same as Fig. 4.2 but for the e^+e^- trident channel.

cross section. This suggests the presence of mass suppression effects in the BH process. We do not investigate this further, but note that there are large cancellations between the two BH diagrams in Fig. 4.1 which are only present for vector-like couplings.

The Equivalent Photon Approximation

We now comment on the EPA for neutrino trident production. This approximation is known to perform quite badly for the SM neutrino trident production cross section [135]. One may wonder, however, if the EPA gets better or worse when computing our BSM cross sections. Naturally, it would be most inadequate for the resonant-like cross sections, since the photon propagator and the strong $1/Q^4$ behaviour is absent. However, if one focuses on the BH contributions, a marginal improvement of the accuracy of the approximation is seen as one lowers the mass of the Z' mediator. In the SM, the $\nu - \gamma$ cross sections scale as
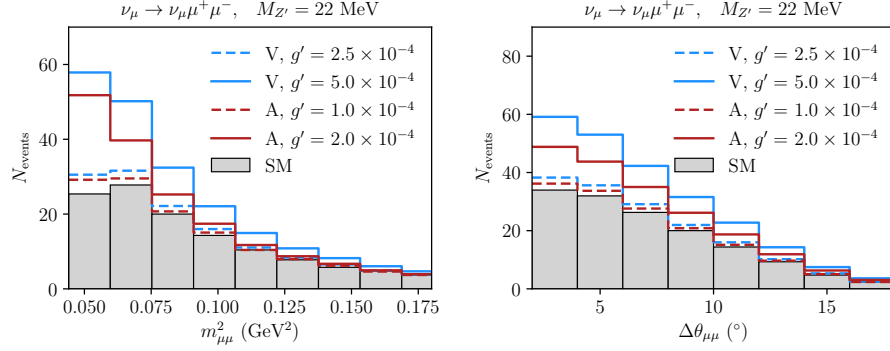
Fig. 4.4. Distribution of the number of neutrino trident events as a function of the invariant mass of the dimuon pair (left) and their separation angle (right) at the DUNE ND. The distributions were produced using the DUNE 120 GeV p^+ neutrino beam and have been smeared as described in Section 4.4.1. For the new physics, we plot the case of a vector (V), $Q^L = Q^R$, and axial-vector (A), $Q^L = -Q^R$, Z' assuming Q^L_α to be given by $L_\mu - L_\tau$.

a typical weak cross section, $\sigma_{\nu\gamma} \propto G_F^2 \hat{s}$, where $\hat{s}$ is the square of the center of mass energy of the $\nu - \gamma$ system. On the other hand, if the cross section is dominated by the BSM BH contributions, then as we take the limit of small Z' masses, it scales more similarly to a QED cross section, $\sigma_{\nu\gamma} \propto 1/\hat{s}$. This behaviour, however, is only present at low masses and only for the BSM contribution. Since we are interested in regions of the parameter space where BSM and SM cross sections are of similar size, then we expect the total cross section to have a behaviour which is a combination of the two. As a sanity check, we numerically verified that for parameter space points where the BSM contributions are of the same order as the SM cross section, the improvement in the accuracy of the EPA is still not satisfactory. For instance, the ratio between the EPA prediction and the full calculation for the dimuon channel assuming a $Q_{\text{max}} = (140 \text{ MeV})/A^{1/3}$ goes from $\approx 30\%$ in the SM to $\approx 60\%$ for $g' = 8 \times 10^{-4}$ and $M_{Z'} = 5$ MeV. For this reason, we only use the full $2 \to 4$ calculation in what follows.

Trident kinematical distributions

The impact of new physics on the total cross section for trident production has been explored in the previous section. It is then natural to ask what the impact of new physics is on the kinematics of trident production which are, especially in the case of the invariant mass and angular variables, of utmost importance for background reduction. In this section we show how the new physics can alter the distributions of these important variables. All
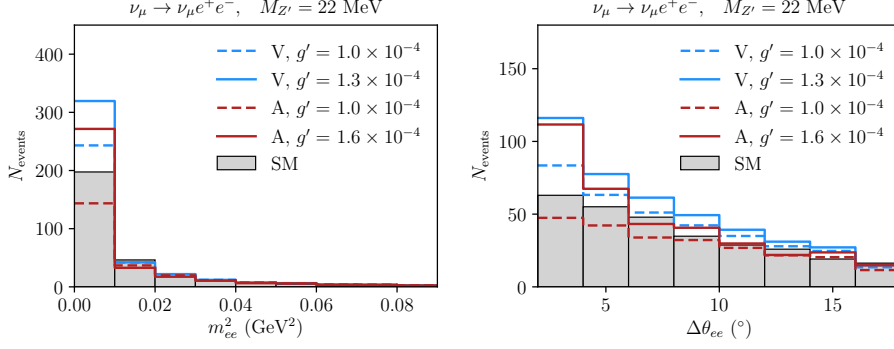
Fig. 4.5. Same as Fig. 4.4 but for e^+e^- trident events. In all cases we assume Q_α^L to be given by $L_e - L_\mu$.

results that follow have been obtained using trident events produced by our dedicated Monte Carlo (MC). Smearing and selection cuts have been applied as detailed in Sec. 4.4.

The variables of interest in background reduction are the charged lepton invariant mass $m_{\ell\ell}^2$ and their separation angle $\Delta\theta_{\ell\ell}$. In Fig. 4.4 we show the dimuon invariant mass spectrum between $4m_\mu^2$ and 0.2 GeV^2, and the dimuon separation angle between $2°$ and $18°$ for a light vector boson with $M_{Z'} = 22$ MeV. We show the results for the dielectron channel in Fig. 4.5. The light new physics here enhances these distributions at low values of these parameters. We show our results for two types of mediators, vector and axial-vector leptophilic bosons. Comparing the couplings necessary to produce similar BSM enhances of the number of events, we see that axial-vector bosons lead to larger enhancements with smaller couplings. In particular, it leads to greater spectral distortions for the Z' mass shown.

4.3.2   Neutrino-electron scattering

$\nu - e$ kinematical distributions

The angle between the scattered electron and the outgoing neutrino θ is related to their energies as

$$1 - \cos\theta = m_e \frac{1-y}{E_e},$$

where $y \equiv T_e/E_\nu$ is the inelasticity ($T_{\rm th}/E_\nu < y < 1$) and $E_e = T_e + m_e$ is the outgoing electron energy. This implies that at $\mathcal{O}(\text{GeV})$ neutrino energies, the electron recoil is very forward and obey $E_e\theta^2 < 2m_e$, up to detector resolution. For this reason, we choose to
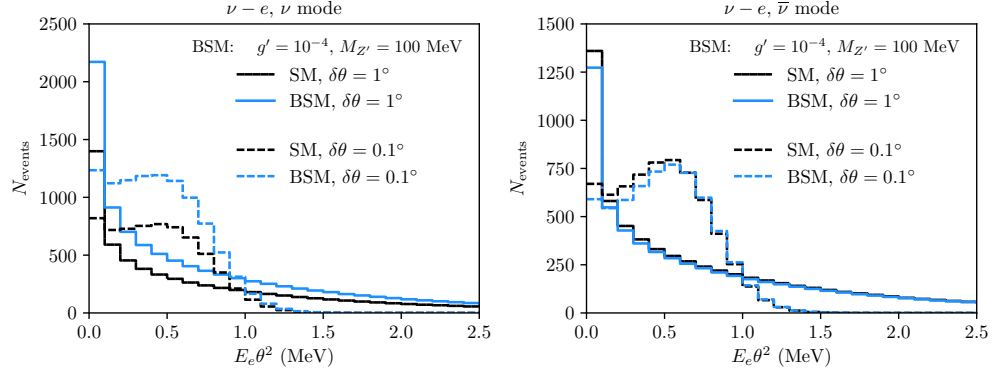
Fig. 4.6. Number of $\nu - e$ scattering events in the DUNE ND as a function of $E_e\theta^2$ for the neutrino (left) and antineutrino (right) beams from the 120 GeV p^+ configuration. We show the prediction in the SM and in a vector $L_e - L_\mu$ Z' model for two angular resolutions $\delta\theta$. The electron kinetic energy threshold is taken to be 600 MeV and the energy resolution is fixed at $\sigma/E = 15\%/\sqrt{E}$.

analyse our results in terms of $E_e\theta^2$. In this case, the differential cross section becomes

$$\frac{d\sigma_{\nu_\alpha - e}}{d(E_e\theta^2)} = \frac{E_\nu}{2m_e}\frac{d\sigma_{\nu_\alpha - e}}{dT_e}\bigg|_{T_e = E_\nu(1 - \frac{E_e\theta^2}{2m_e})} . \qquad (4.3.7)$$

This distribution is particularly important for suppressing the background. Given the kinematics explained above, $E_e\theta^2$ must be smaller than $2m_e$ for $\nu - e$ scattering, while it is often much larger for neutrino-nucleon scattering, the dominant background (See Section 4.4.1). We show in Fig. 4.6 the expected $\nu - e$ event distribution as a function of $E_e\theta^2$ for the SM and a light Z' case, in the neutrino and anti-neutrino modes at the DUNE ND. As expected, the signal is extremely forward and the final distribution is highly sensitive to the angular resolution $\delta\theta$ of the detector. At a conservative value of $\delta\theta = 1°$, little information about the true distribution is left, and a significant portion of the signal lies in a region where $E_e\theta^2 > 2m_e$. Therefore, shape information may improve the search for a light new physics only when the angular and energy resolutions of the detector are well understood.

4.3.3   Interference effects

Since for $\nu - e$ scattering and neutrino trident production there exists a SM contribution, we expect the experimental sensitivity to new physics to be dominated by the interference between SM and BSM contributions. We now argue what kind of interference one can expect in each one of these processes.

For neutrino trident production we follow Ref. [164] and separate the differential cross section as

$$d\sigma = \hat{V}^2 \, d\sigma_{\rm V} + \hat{V}\hat{A} \, d\sigma_{\rm V-A} + \hat{A}^2 \, d\sigma_{\rm A}, \qquad (4.3.8)$$

where we dropped the flavour indices in $\hat{V}$ and $\hat{A}$ from (4.3.4b) for simplicity. This allows us to write the interference between the SM and the vector new physics as

$$d\sigma_{\rm INT} = \frac{Q_\alpha^L Q_\beta^V}{2\sqrt{2}G_F} \frac{(g')^2}{K^2 + M_{Z'}^2} \left(2\, C_{\rm V}^{\rm SM} \, d\sigma_{\rm V} + C_{\rm A}^{\rm SM} \, d\sigma_{\rm V-A} \right). \qquad (4.3.9)$$

Depending on the region of phase space considered, the term proportional to $d\sigma_{\rm V-A}$ can be of similar size to $d\sigma_{\rm V}$. However, $d\sigma_{\rm V-A}$ changes sign as a function of the angular variables or energies, leading to small integrated cross sections (typically two orders of magnitude smaller than the integral of the $d\sigma_{\rm V}$ term). Ignoring this term, one can then completely predict the type of interference in trident production. For $\nu_\mu \to \nu_\mu \mu^+ \mu^-$ trident production, for instance, $C_{\rm V}^{\rm SM} > 0$ and the second generation charge appears squared, leading to constructive interference in all cases. For $\nu_\mu \to \nu_\mu e^+ e^-$ trident events, on the other hand, $C_{\rm V}^{\rm SM} < 0$. If the first and second generation charges come in with opposite signs, then the interference is still constructive, otherwise destructive interference happens. The same considerations also apply to antineutrino scattering if one ignores the $d\sigma_{\rm V-A}$ term. Finally, the axial-vector case is completely analogous taking $V \leftrightarrow A$ in Eq. (4.3.9).

For $\nu - e$ scattering analytical expressions can easily be used [21]. Taking $C_L^{\rm SM} = -1/2 + s_{\rm W}^2 \sim -1/4$ and $C_L^{\rm SM} = s_{\rm W}^2 \sim 1/4$ we have

$$\frac{d\sigma_{{\rm INT}\,\nu_\mu - e}}{dT_e} \sim -\frac{\sqrt{2}m_e G_F}{4\pi} \frac{g'^2}{m_{Z'}^2 + 2m_e T_e} \left(-1 + (1-y)^2 \right) \qquad (4.3.10{\rm a})$$

$$\frac{d\sigma_{{\rm INT}\,\bar{\nu}_\mu - e}}{dT_e} \sim -\frac{\sqrt{2}m_e G_F}{4\pi} \frac{g'^2}{m_{Z'}^2 + 2m_e T_e} \left(1 - (1-y)^2 \right). \qquad (4.3.10{\rm b})$$

Since $y < 1$, the interference term for $\nu_\mu - e$ is always positive (constructive), and for $\bar{\nu}_\mu - e$ it is always negative (destructive).

4.4 DUNE sensitivities

Having studied the behaviour of neutrino trident production and neutrino-electron scattering cross sections in the presence of light new bosons, we now apply our results in

sensitivity studies for the DUNE ND. As discussed in Section 4.2, we limit our studies to $L_e - L_\mu$ and $L_\mu - L_\tau$ models with vector gauge bosons. We start with a discussion on the experimental details, highlighting the challenges of backgrounds and laying out our statistical methods in Section 4.4.1. Then we show our main results in Sections 4.4.2 and 4.4.3, comparing our sensitivity curves to the leading bounds in the parameter space of the leptophilic models from other experiments.

4.4.1 Analysis techniques

The LBNF is expected to produce an intense beam of neutrinos and antineutrinos from a 1.2 MW proton beam colliding against a fixed target [113]. The DUNE ND, where the number of neutrino interactions is the largest, is expected to be located at a distance of 574 m from the target. Despite its design not being final yet [165, 166], we focus on the possibility of a 75-t fiducial mass Liquid Argon (LAr) detector. Regarding the neutrino fluxes, we now concentrate on the option of a beam from 120 GeV protons with 1.1×10^{21} POT per year. The LBNF could also provide higher or lower energy neutrinos depending on the proton energy, target and focusing system used. We explore other possibilities shown in Table 4.1 and we take the flux files provided in Ref. [167, 168]. We assume that the experiment will run 5 years in neutrino and another 5 years in antineutrino mode. The final exposure, therefore, will vary with beam designs, and is equal to a total of 11×10^{22} POT in the case of 120 GeV protons. To generate neutrino scattering events, we use our own dedicated MC, Gaussian smearing the true MC energies and angles as a proxy for the detector effects during reconstruction. We assume an energy resolution of $\sigma/E = 15\%/\sqrt{E}$ ($\sigma/E = 6\%/\sqrt{E}$) for e/γ showers (muons) and angular resolutions of $\delta\theta = 1°$ for all particles [43].

An interesting addition to the design of the DUNE ND would be a magnetized high-pressure Gaseous Argon (GAr) tracker placed directly behind the LAr module [169]. The lower thresholds for particle reconstruction and the presence of a magnetic field is expected to improve event reconstruction and reduce backgrounds to neutrino-electron scattering and neutrino trident production. We note that despite the relatively small fiducial mass of such a GAr module, $\lesssim 1$ tonne, it would still provide a sizeable number of these rare leptonic neutrino scattering processes.

Design	Mode	$\mu^+\mu^-$ trident	e^+e^- trident	$\nu - e$ scattering	POTs/year
62.4 GeV p^+	ν	36.5	92.7	7670	1.83×10^{21}
	$\overline{\nu}$	27.3	73.4	4620	1.83×10^{21}
80 GeV p^+	ν	42.0	102	8380	1.4×10^{21}
	$\overline{\nu}$	33.0	84.3	5320	1.4×10^{21}
120 GeV p^+	ν	47.6	110	8930	1.1×10^{21}
	$\overline{\nu}$	40.7	97.6	6450	1.1×10^{21}
ν_τ app optm	ν	210	321	24900	1.1×10^{21}
	$\overline{\nu}$	156	243	14700	1.1×10^{21}

Tab. 4.1. The SM rates for neutrino trident production and neutrino-electron scattering per year at the 75-t DUNE ND after kinematical cuts.

With the intense flux at DUNE and the large number of POT, the $\nu - e$ scattering measurement will not be statistically limited, with order 10^4 events in the DUNE ND after a few years. Systematics from the beam and detector are then the limiting factor for the sensitivity to new physics in this measurement. Current work on neutrino flux uncertainties shows that normalization uncertainties can be reduced to the order of 5% [170–172], with similar projections for DUNE [113]. The electron energy threshold also plays a role in the new physics search. In particular, for new light bosons the enhancement at very low momentum transfer $2T_e m_e$ has a cut-off at the minimum electron recoil energy (see Eq. (3.1.6)). This implies that the experiment is no longer sensitive to the Z' mass below $\sqrt{2T_{\text{th}}m_e}$. In our analysis, we assume a realistic overall normalization systematic uncertainty of 5% and a $\nu - e$ scattering electron kinetic energy threshold of 600 MeV.

Lowering systematic uncertainties on the flux is challenging given the large hadroproduction and focusing uncertainties at the LBNF beam. Here, improvements on the experimental side in determining the neutrino flux will be extremely valuable (see *e.g.* Ref. [173]). If one is searching for novel leptophilic neutral currents, hadronic processes and inverse muon decay measurements are available, but these are limited either by theoretical uncertainties or by statistics, and might not be applicable in the whole energy region of interest. As to the electron energy, assuming a threshold as low as 30 MeV would be safe for electron detection, but at these low energies backgrounds can be incredibly challenging due to the overwhelming π^0 backgrounds. Increasing this threshold to 600 MeV, however, has little impact in our sensitivities and is only 200 MeV below the threshold used in the most recent MINERνA analysis [133], where good reconstruction is important for measuring

the flux. For e^+e^- and $\mu^+\mu^-$ tridents, we refrain from increasing the analysis thresholds from a naive 30 MeV. This is certainly an aggressive assumption but it is necessary if e^+e^- tridents are to be measured, since these events are quite soft [135]. Thresholds for $\mu^+\mu^-$ tridents are much less important since the events are generally more energetic than their dielectron analogue.

Backgrounds ($\nu_\mu \to \nu_\mu \ell^+\ell^-$) We now discuss the individual sources of backgrounds to neutrino trident production. A pair of charged leptons is very rarely produced in neutrino interactions, usually coming from heavy resonance decays [109, 160, 174–176]. Since our signal is mostly coming from coherent interactions with nuclei, cuts in the hadronic energy deposition in the detector E_{had}, often large in heavy meson production processes, can help reduce backgrounds. Coherent and diffractive production of mesons is an exception to this, in particular pion production [72, 73, 75, 78], which is the main background to trident due to particle mis-identification (misID). Muons are known to be easily spoofed by charged pions, making CC ν_μ interactions with $\pi^\pm$ in the final state (CC1π) one of the largest contributions to the backgrounds of $\mu^+\mu^-$ tridents. Similarly, NC π^0 production stands as the leading background to e^+e^- tridents when the photons are misIDed as two electrons, or if one of the photons pair converts and the other escapes detection. In Ref. [135], we have shown that the $\mu^+\mu^-$ and e^+e^- pairs produced in trident have small separation angles ($\Delta\theta$), possess small invariant masses ($m_{\ell\ell}^2$) and that both charged leptons are produced with small angles with respect to the neutrino beam ($\theta_\pm$). With simplified misID rates, we used the GENIE [46] event generator to show that simple kinematical cuts can reduce backgrounds significantly, achieving a significance of $S_{\mu\mu}/\sqrt{B_{\mu\mu}} \sim 44$ and $S_{ee}/\sqrt{B_{ee}} \sim 17.3$ for the DUNE ND in neutrino mode, where S and B stand for signal and background, respectively. In our current analysis we implement the same kinematical cuts, which are as follows: $m_{\mu\mu}^2 < 0.2$ GeV^2, $\theta_\pm < 15°$ and $\Delta\theta < 20°$ for the $\mu^+\mu^-$ channel, and $m_{ee}^2 < 0.1$ GeV^2, $\theta_\pm < 20°$ and $\Delta\theta < 40°$ for the e^+e^- one. We impose these cuts again in our signal analysis, and point out that the new physics enhancement happens precisely in this favourable kinematical region, (see Section 4.3.1). Given the background rejection we find with our naive misID rates, we do not include backgrounds in our results, unless indicated otherwise.
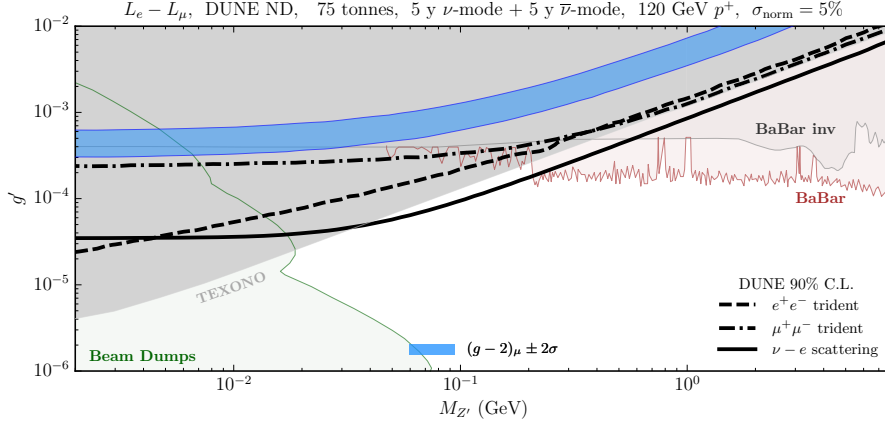
Fig. 4.7. The DUNE ND neutrino scattering sensitivities to the $L_e - L_\mu$ Z' at 90% C.L. The solid line shows the $\nu - e$ scattering sensitivity, followed by the dielectron trident in dashed line, and the dimuon trident in dot-dashed line. The coloured regions are excluded by other experiments, where we highlight the neutrino-electron scattering measurements at reactor experiments [1–3], searches at the BaBar e^+e^- collider [4,5] and beam dump experiments [6].

Backgrounds ($\nu - e$)   For neutrino-electron scattering, backgrounds will arise from either the genuine production of an electron or via the misID of particle showers in the detector, both in the absence of observable hadronic energy deposition. The former scenario happens mostly by the CC interactions of the flux suppressed ν_e states present in the beam. The main contribution will be from CCQE interactions where the struck nucleon is invisible either for being below threshold or due to nuclear re-absorption. The misID of a photon initiated EM shower for an electron one is expected to be rare in LAr, where the first few cm of the showers can be used to separate electrons and photons by their characteristic dE/dx. However, the large NC rates for the production of single photons and π^0 can become a non-negligible background. For instance, coherent NC π^0 production leaves no observable hadronic signature and may look like a single electron if one of the photons is mis-identified and the other escapes detection. Finally, after misID happens, the signal can still look unique in its kinematical properties. In particular, $E_e\theta^2$ cuts can dramatically reduce backgrounds due to the forwardness of our signal (see e.g. [133, 177]).

Statistics.   In order to assess the potential of DUNE to discover new physics, we perform a sensitivity analysis using a χ^2 test with a pull method for systematic uncertainties. Our goal is to assess when DUNE would be able to rule out the SM, and so we generate BSM
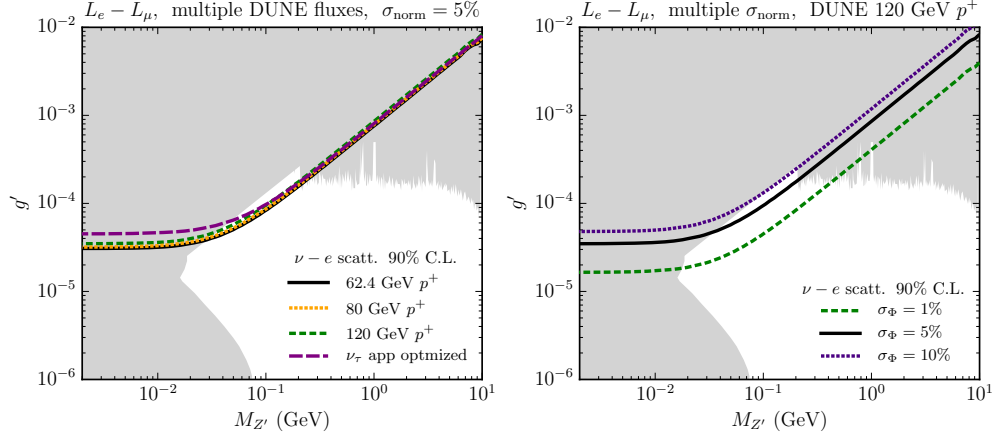
Fig. 4.8. The $\nu - e$ scattering sensitivity to the $L_e - L_\mu$ model at 90% C.L. On the left panel we show the sensitivity using different choices for the neutrino flux, and on the right we use the neutrino beam from 120 GeV protons and vary the normalization systematic uncertainty from an aggressive 1% to a conservative 10%.

events and fit the SM prediction to it. Our χ^2 function is defined as

$$\chi^2 = \min_\alpha \left[\frac{(N_{\text{BSM}} - (1+\alpha)N_{\text{SM}} - (\alpha+\beta)N_{\text{BKG}})^2}{N_{\text{BSM}}} \right.$$
$$\left. + \left(\frac{\alpha}{\sigma_{\text{norm}}} \right)^2 + \left(\frac{\beta}{\sigma_{\text{BKG}}} \right)^2 \right], \qquad (4.4.1)$$

where the number of events for the BSM case is given by N_{BSM}, the SM number of events is N_{SM} and the number of background events is N_{BKG}. The nuisance parameters α and β, with their uncertainties σ_{norm} and σ_{BKG}, take into account normalization uncertainties from the flux and detector, and uncertainties on the background prediction, respectively. For the DUNE ND, we assume $\sigma_{\text{norm}} = 5\%$ and $\sigma_{\text{BKG}} = 10\%$. These systematics will likely be dominated by flux normalization uncertainties, and can only be measured with interactions that do not depend on the leptophilic BSM physics.

4.4.2 $L_e - L_\mu$

New vector bosons with couplings to the first and second generation leptons can be probed very effectively in neutrino experiments by meausuring the $\nu - e$ scattering rate. This has been recognized in the literature [6, 21, 178], where bounds from various experiments, including CHARM-II [179], TEXONO [1–3] and Borexino [180] have been derived on these bosons. Curiously, the bound calculated from the CHARM-II data has been pointed out by Ref. [6] to be too optimistic. The uncertainty on the neutrino flux is a real hindrance

for these measurements which has not been taken into account when these bounds were computed. This is particularly important for measurements with large statistics, and for this reason we do not show the CHARM-II bound here. The measurement of $\overline{\nu}_e - e$ scattering at TEXONO, on the other hand, is statistically limited, and the bound it places on this class of models can safely ignore the flux systematics. This turns out to provide the strongest limit in a large region of the $L_e - L_\mu$ parameter space. Trident bounds can be obtained for this model, but due to their lower statistics and more involved kinematics, are subdominant.

We show our results for the DUNE ND in Fig. 4.7. Our results are for the combined $\nu + \bar{\nu}$ modes and do not include backgrounds. The opposite charges between the first and second families implies constructive interference between the SM and BSM contributions for neutrino scattering, contrary to what happens in a $B - L$ model, for instance. Therefore, the strongest bounds on this model can be obtained at DUNE in neutrino mode. It is clear, however, that the degree with which DUNE can probe unexplored parameter space is a question of how much the uncertainties on the flux can be lowered. To illustrate this effect, we vary the normalization systematics on the right panel of Fig. 4.8, going from a conservative 10% to an aggressive 1% uncertainty. The effect of changing the thresholds is very small, being most important in a region already probed by other experiments. Different beam designs seem to have only a small impact on the sensitivity, as shown on the left panel of Fig. 4.8.

Since we show the bounds obtained from the neutrino and antineutrino runs combined, it is not possible to see the effects of destructive interference. If only channels with destructive interference were available, however, it would have been possible to allow for cancellations between the total interference and the square of the BSM contributions in certain regions of parameter space at the level of the total rate. The region where this cancellation happens depends strongly on the neutrino energies involved and on the integrated phase space of the recoiled electron. In that case, one expects that the sensitivity to the lowest new physics couplings comes, in fact, from the search for a deficit of $\nu - e$ scattering events, as opposed to the constructive interference case where an excess of events is always produced. We note that this has no significant impact on the sensitivity of a leptophilic Z', but might provide crucial information about the nature of the Z' charges in case of detection.

The trident bounds we obtain are not competitive for this model despite the fact that the trident cross sections receive similar enhancements to that of $\nu - e$ scattering. This is due to two reasons: the low number of events and the non-trivial kinematics of trident processes. Since the neutrino is essentially scattering off virtual charged leptons produced in the Coulomb field of the nucleus, it has to typically transfer more energy to the system than it would in a scattering off real particles in order to produce visible signatures. This remark also helps us to explain the behaviour of the sensitivity curves at the lowest masses. Whilst $\nu - e$ scattering cross sections become insensitive to the boson mass at $\sqrt{2 m_e T_{\rm th}}$, the trident cross sections do not. This behaviour is most dramatic in the $e^+ e^-$ tridents, but is also present in the $\mu^+ \mu^-$ one. This is a consequence of the 4-body phase space kinematics, where now the momentum transfer through the Z' propagator is no longer trivially related to the final state particle energies, as in $2 \rightarrow 2$ processes. It should be noted, however, that both the dimuon and the dielectron trident rates become nearly independent of $M_{Z'}$ below the muon and the electron mass, respectively, where only a logarithmic dependence is expected [11].

DUNE can also probe this class of models in a different way. In the context of long range forces in neutrino oscillation experiments and with the same choice of charges, Ref. [181] places competitive bounds in this model with Super-Kamiokande data and makes projections for DUNE. The matter potential created by the local matter density modifies the dispersion relation of the neutrinos with lepton non-universal charges, leading to very competitive bounds in our region of interest. Similar considerations have also been explored in the context of high-energy astrophysical neutrinos [182]. Other experimental searches have been conducted at electron beam dumps. This technique consists of producing the Z' boson at the target via radiative processes such as $e + A \rightarrow e + A + Z'$, and look for the visible decays of the boson in the detector. In this model, the decay products are mostly $e^+ e^-$ states and the bounds are only applicable at appreciably small values of g' and $M_{Z'}$, where the lifetime of the Z' is sufficiently large. Probing the large mass region, on the other hand, requires high-energy experiments. In that regime, the strongest bounds come from searches at the $e^+ e^-$ collider BaBar. These come about in two ways: looking for the visible decay products of a Z' produced radiatively or in heavy meson decays [4], or exploring the BR into invisible final states [5].
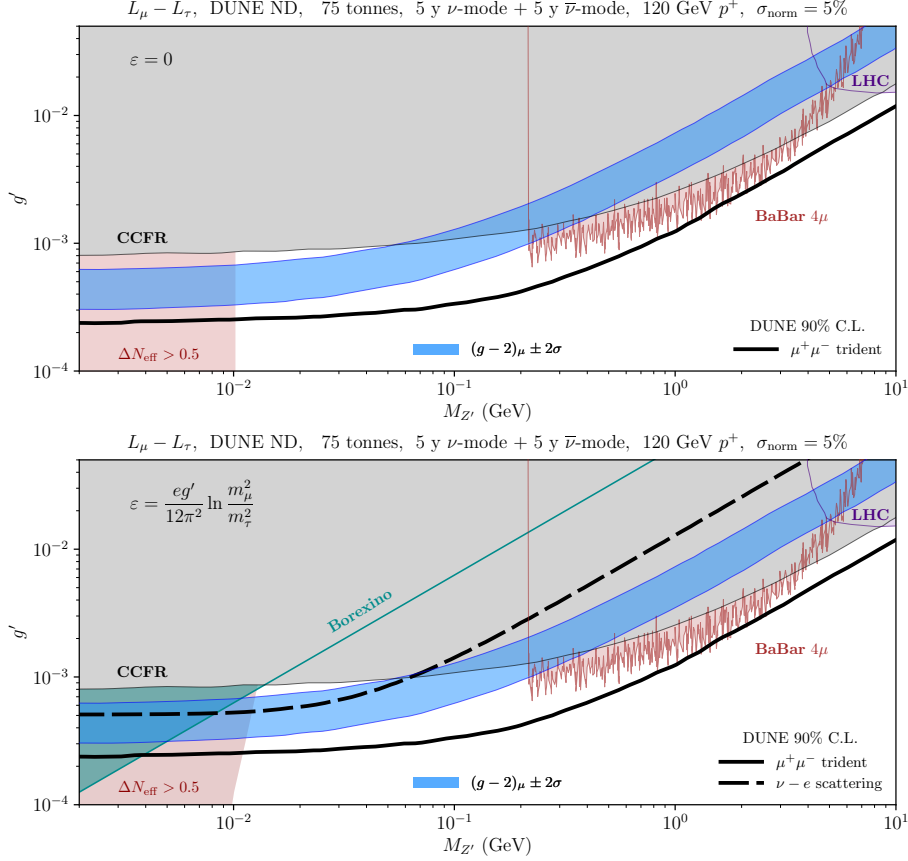
Fig. 4.9. The DUNE ND neutrino scattering sensitivities for $L_\mu - L_\tau$ at 90% C.L. The upper panel shows the case with no kinetic mixing, and the lower panel the case with the loop-induced mixing. Bounds from neutrino-electron scattering apply only to the latter. We also show bounds from BaBar [7], LHC [8], Borexino [9] and from the neutrino trident production measurement at CCFR [10,11]. Recent cosmological bounds for the two kinetic mixing cases derived in Ref. [12] are also shown.

4.4.3 $L_\mu - L_\tau$

In this section we evaluate the DUNE ND sensitivity to the presence of a light vector Z' charged under $L_\mu - L_\tau$. Beyond being anomaly free, this choice of charges allows for positive contributions to the anomalous magnetic moment of the muon, $a_\mu = (g-2)_\mu$, as discussed in Refs. [149, 152, 183–185]. This quantity is well known for a $\sim 3.7\sigma$ discrepancy between the experimental measurement [186] and the theory predictions [187, 188]. If future efforts to measure it [189] confirm this disagreement and if theoretical uncertainties are better controlled in the next few years, then constraining new physics scenarios that could contribute to a_μ is of utmost importance.

This model can significantly impact neutrino trident production of a muon pair. In fact, the leading bound in this parameter space for masses $M_{Z'} \lesssim 200$ MeV comes from the
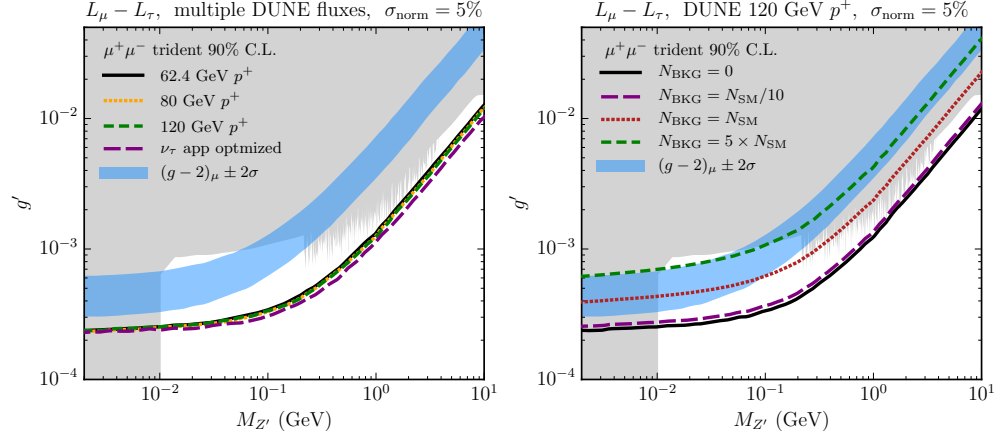
Fig. 4.10. The dimuon neutrino trident sensitivity to the $L_\mu - L_\tau$ model with no kinetic mixing at 90% C.L. On the left panel we show the sensitivity using different choices for the neutrino flux, and on the right we use the neutrino beam from 120 GeV protons and scale the background with respect to the total number of SM trident events after cuts.

CCFR measurement of the same neutrino trident channel [10]. CCFR observed 37.0 ± 12.4 events, extracting a measurement of the trident cross section of $\sigma_{\rm CCFR}/\sigma_{\rm SM} = 0.82 \pm 0.28$. Curiously, the measurement by CHARM-II [30] provides weaker constraints on this model despite seeing a larger number of trident events, namely 55 ± 16 events in total, most likely due to the 1σ upward fluctuation of the measurement: $\sigma_{\rm CHARM-II}/\sigma_{\rm SM} = 1.58 \pm 0.57$. Other important bounds from $\nu - e$ scattering have also been obtained using the kinetic mixing parameter generated at one-loop. The strongest of which uses data from Borexino [9], and are only relevant for the low mass region $M_{Z'} \lesssim 20$ MeV.

At DUNE, both of these measurements are possible, allowing to constrain this model in different ways. We show our results in Fig. 4.9, without including backgrounds. In this scenario, DUNE would be able to cover all the 2σ region compatible with the $(g-2)_\mu$ measurement only with the $\mu^+\mu^-$ trident events. For the low mass region, measuring the $\nu - e$ scattering rate can provide a complementary probe of this region, depending most strongly on the systematic uncertainties DUNE can achieve. We note that analysis thresholds used for $\nu - e$ scattering have little impact on the sensitivity in the region of interest. Our conclusion that DUNE can cover all of the $(g-2)_\mu$ region holds provided backgrounds are kept below the SM signal rate. This can be seen when we include backgrounds with different assumption on the right panel of Fig. 4.10. Finally, different assumption for the beam design have little impact on the sensitivity, as show on the left panel of Fig. 4.10.

Apart from neutrino scattering, dedicated searches for resonances decaying into $\mu^+\mu^-$ in four muon final states have been performed at BaBar [7], looking for $e^+e^- \to \mu^+\mu^- Z'(\to \mu^+\mu^-)$. At the LHC, the searches for $Z \to 4\mu$ [8] performed by the ATLAS collaboration can be recast into a bound on Z'. Here, we show the bounds derived in [11]. Big Bang Nucleosynthesis bounds were studied in [149, 185], and shown to constrain the mass of the boson to be $M_{Z'} \gtrsim 5$ MeV. Recently, additional constraints from Cosmology were derived given that the presence of very light Z' bosons changes the evolution of the early Universe [12]. In particular, the decays and inverse decays induced by the new leptophilic interactions can modify the neutrino relativistic degrees of freedom, requiring $M_{Z'} \gtrsim 10$ MeV in order for $\Delta N_{\text{eff}} < 0.5$ for the case with no kinetic mixing. The authors of Ref. [12] also found that an additional Z' boson can alleviate the tension in the different measurements of the Hubble parameter. Let us stress here that all these bounds will be complementary to possible future constraints that can be obtained by the DUNE program, as shown in Fig. 4.9.

4.5 Conclusions

Although the next generation neutrino oscillation experiments are primarily designed for making precision measurements of the neutrino mixing parameters, the unprecedented fluxes and large detectors will allow for many non-minimal new physics searches. In this work, we have considered the physics potential of the DUNE ND for constraining the existence of an additional anomaly-free $U(1)$ gauge group giving rise to a Z' boson which only couples to leptons — a form of a purely leptophilic neutral current. Specifically, we have considered the anomaly free scenarios with charges associated to the lepton number difference $L_\alpha - L_\beta$. Focusing on the two most promising neutrino scattering processes, $\nu - e$ and $\nu\ell\ell$ trident scattering, we have computed expected sensitivity curves for the DUNE ND for a variety of charge assignments.

In performing our sensitivity studies as a function of the coupling and mass of the Z' boson, we have remained as faithful as possible to the real experimental conditions of a LAr detector. Our main results rely on the realistic assumptions of flux uncertainties of 5% and feasible exposures. To avoid large backgrounds, we have also implemented kinematical cuts on the neutrino trident sample, and a kinetic energy threshold of 600 MeV for $\nu - e$

scattering events. The parameter space which can be probed by $\nu - e$ scattering in the $L_e - L_\mu$ scenario is at least two times better than the $e^+ e^-$ and almost twenty times better than the $\mu^+ \mu^-$ trident channels, specially for the lower mass region. In this case, the DUNE ND would improve only slightly on previous $\nu - e$ scattering bounds, especially at around $M_{Z'} \sim 100$ MeV. We do not expect $e^+ e^-$ trident measurements at DUNE to improve our coverage of the $L_e - L_\mu$ Z' parameter space, but note this process has a distinct dependence on $M_{Z'}$ if compared to $\nu - e$ scattering.

If the light vector Z' is charged under $L_\mu - L_\tau$, we have found that the dimuon trident measurement could provide the leading bound in this parameter space. This is particularly interesting as these models can also explain the discrepancy between the measurement of the anomalous magnetic moment of the muon and its SM prediction. We expect that DUNE will be able to fully explore the $(g-2)_\mu$ motivated parameter space provided backgrounds are kept under control. The robustness of our results is tested against different choices of neutrino fluxes, where we find that despite the larger rates at higher neutrino energies and the larger BSM enhancement at lower energies, the sensitivities are very similar.

Improvements to the experimental sensitivities we have displayed in Figs. 4.7 and 4.9 can be achieved by reducing uncertainties on the neutrino flux and detection. From the experimental side, novel detection techniques suitable to rare neutrino events are currently under discussion, such as the magnetized HPgTPC [169] and the Straw Tube Tracker [190, 191]. Together with improved analysis techniques, these will help to improve upon our projections for the sensitivity of DUNE to new physics that might be hiding at light masses and small couplings.

Chapter 5

A dark neutrino sector
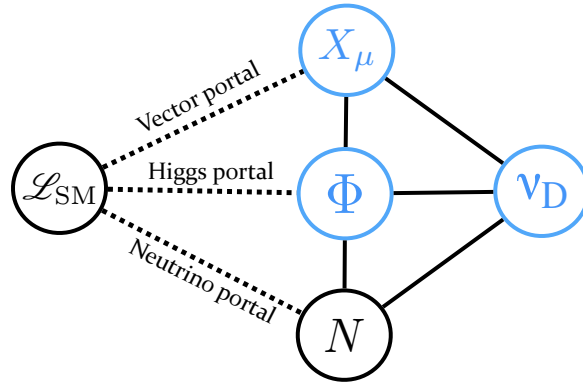
Fig. 5.1. Schematic representation of our dark neutrino model. The dark neutrino, ν_D and the complex scalar Φ are the only fields charged under the new $\mathrm{U}(1)'$ gauge symmetry. The new vector boson X_μ acquires a mass after spontaneous symmetry breakig, and N remains a complete singlet.

Chapter 6

Tests of the MiniBooNE explanation

Introduction – Non-zero neutrino masses have been established in the last twenty years by measurements of neutrino flavor conversion in natural and human-made sources, including long- and short-baseline experiments. The overwhelming majority of data points towards a three-neutrino framework. Within this framework, we have measured the mixing angles that parametrize the relationship between mass and flavor eigenstates to percent-level precision [108]. The remaining unknowns are the absolute scale of neutrino masses and their origin, the CP-violating phase, and the mass ordering of the neutrinos. In addition, anomalies in short-baseline accelerator and reactor experiments [192–195] are yet to have satisfying explanations. The most significant anomalies are beyond statistical doubt. Minimal extensions of the three-neutrino framework to explain the anomalies introduce the so-called sterile neutrino states, which do not participate in Standard Model (SM) interactions in order to agree with measurements of the Z-boson invisible decay width [196]. Unfortunately, these minimal scenarios are disfavoured as they fail to explain all data [197–199]. This has led the community to explore nonminimal scenarios. Along this direction, it is interesting to study well-motivated neutrino-mass models that can also explain the short-baseline anomalies and are testable in the laboratory. In this work, we will examine the class of neutrino-mass-related models that have been proposed as an explanation of the anomalous observation of electron-neutrino-like events in MiniBooNE [195].

The MiniBooNE excess is currently in tension with the standard three-neutrino prediction at a level of 4.7σ [195]. While it is possible that the excess is fully or partially due to systematic uncertainties or SM backgrounds (see, *e.g.*, [200–202]), many Beyond the Standard Model (BSM) explanations have been put forth. These new physics (NP) scenarios typically require the existence of new particles, which can: participate in short-baseline oscillations [203–225], change the neutrino propagation in matter [222, 226–228], be produced in the beam or in the detector and its surroundings [229–236]. These models either increase the conversion of muon- to electron-neutrinos or produce electron-neutrino-like signatures in the detector, where in the latter category one typically exploits the fact that the LSND and MiniBooNE are Cherenkov detectors that cannot distinguish between electrons and photons. Although it is possible to consider MiniBooNE explanations that have little to no theoretical motivation, recent models [13, 123, 237] are motivated by neutrino-mass generation via hidden interactions in the heavy neutrino sector. In particular, the common feature of these models is the upscattering into a heavy neutrino, usually with tens to
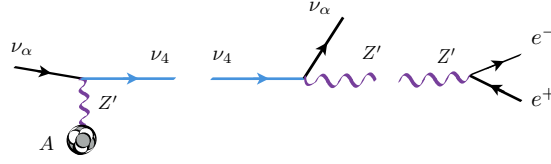
Fig. 6.1. *Illustration of heavy neutrino production.* Left: production of the heavy mass state via upscattering. Center: Decay of the heavy neutrino into a light neutrino and a gauge boson. Right: Decay of a gauge boson into a pair of electrons that produce the experimental signature.

hundreds of MeV in mass, which subsequently decays into a pair of electrons. If collimated, this pair of electrons can fake a single-electron signature.

In this article, we introduce new techniques to probe these testable neutrino mass generation models in past, present, and future neutrino experiments. In addition, our analysis showcases a generic way to look for models that rely on the ambiguity between photons and electrons to explain the MiniBooNE observation. Due to the electron-like nature of the excess, we consider neutrino-electron scattering measurements [2, 133, 179, 180, 238]. Although these experiments have been shown to provide powerful constraints on light NP [21, 239, 240], the unique topology of the signatures we consider requires us to go beyond the final processed sample quoted by the experiments and develop new ways to search for them. Since the typical heavy neutrino mass is in the hundreds-of-MeV regime, we focus on two high-energy neutrino experiments: MINERνA [133, 177, 241] and CHARM-II [179, 242, 243]. These experiments are complementary in neutrino energy and background composition. In both cases we make use of sideband measurements, taking advantage of the excellent particle reconstruction capabilities of MINERνA and the precise measurements at CHARM-II to constrain NP.

Model − We limit our discussion to the minimal version of the model that could explain the MiniBooNE excess. This contains at least one heavy neutrino, ν_D, charged under a new U(1)$'$ gauge group, which is part of the particle content and gauge structure needed for mass generation. The ν_D can be either of a Dirac or Majorana [237] nature. In this paper, we show our results for a Dirac particle since the Majorana case is more severely in tension with the angular distribution [244, 245]. The dark sector is connected to the SM in two ways: through kinetic mixing between the new gauge boson and hypercharge, and through neutrino mass mixing. We start by specifying the kinetic part of the NP

Lagrangian

$$\mathscr{L}_{\text{kin}} \supset \quad \frac{1}{4}\hat{Z}'_{\mu\nu}\hat{Z}'^{\mu\nu} + \frac{\sin\chi}{2}\hat{Z}'_{\mu\nu}\hat{B}^{\mu\nu} + \frac{m_{\hat{Z}'}^2}{2}\hat{Z}'^{\mu}\hat{Z}'_{\mu}, \qquad (6.0.1)$$

where $\hat{Z}'^{\mu}$ stands for the new gauge boson field, $\hat{Z}'^{\mu\nu}$ its field strength, and $\hat{B}^{\mu\nu}$ the hypercharge field strength. After usual field redefinitions [246], we arrive at the physical states of the theory. Working at leading order in χ and assuming $m_{Z'}^2/m_Z^2$ to be small, we can specify the relevant interaction Lagrangian as

$$\mathscr{L}_{\text{int}} \supset \quad g_D\overline{\nu}_D\gamma_\mu\nu_D Z'^{\mu} + e\varepsilon Z'^{\mu}J_\mu^{\text{EM}}, \qquad (6.0.2)$$

where J_μ^{EM} is the SM electromagnetic current, g_D is the U(1)$'$ gauge coupling assumed to be $\mathcal{O}(1)$, and $\varepsilon \equiv c_{\text{w}}\chi$, with c_{w} being the cosine of the weak angle. Additional terms would be present at higher orders in χ and mass mixing with the SM Z is also possible, though severely constrained. After electroweak symmetry breaking, the dark neutrino ν_D is a superposition of neutrino mass states. The flavor and mass eigenstates are related via

$$\nu_\alpha = \sum_{i=1}^{4} U_{\alpha i}\nu_i, \quad (\alpha = e, \mu, \tau, D), \qquad (6.0.3)$$

where U is a 4×4 unitary matrix. It is expected that $|U_{\alpha 4}|$ is small for $\alpha = e, \mu, \tau$, but $|U_{D4}|$ can be of $\mathcal{O}(1)$ [197, 247]. The choice of m_4 and $m_{Z'}$ has important consequences for the allowed decays of the new particle content. We focus on the case in which $m_4 > m_{Z'}$, where the two body $\nu_4 \to \nu_\alpha Z'$ decay is allowed. In addition, the mass of the new gauge boson is kept below ~ 100 MeV, making the decay into e^+e^- pairs the dominant channel. Decay into a pair of neutrinos is possible, but is subdominant provided the mixing is small.

Signature − As illustrated in Fig. 6.1, the heavy neutrino is produced by upscattering from an active neutrino flavour state. The production cross section is proportional to $\alpha_D\alpha_{\text{QED}}\varepsilon^2|U_{\alpha 4}|^2$, usually dominated by the muon-neutrino contribution due to the flavor composition of the beam. This production can happen off the whole nucleus in a coherent way or off individual nucleons. For $m_{Z'} \lesssim 100$ MeV, the production will be mainly coherent, but for heavier masses, such as the ones considered in [123], the upscattering happens predominantly in a diffractive regime. In Fig. 6.2, we show the cross section at the benchmark point of [237] and compare it with the quasi-elastic cross section. By superimposing the cross section on the neutrino fluxes of MINERνA and MiniBooNE, we
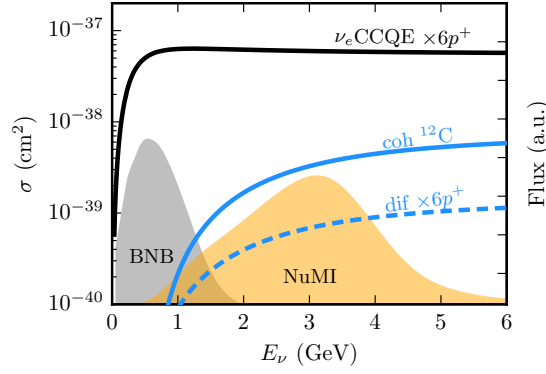
Fig. 6.2. *Upscattering cross section compared to the quasi-elastic.* The quasi-elastic cross section for $6p^+$ is shown as a function of the neutrino energy (solid black line). Similarly the coherent, out of a carbon atom, and the diffractive NP contributions for the benchmark point of [13] are shown as solid and dashed blue lines, respectively. In the background, the light gray shaded region is the Booster Neutrino Beam (BNB) flux shape, while the light golden region is the Neutrinos at the Main Injector (NuMI) low-energy neutrino-mode flux.

make it explicit that the larger energies at MINERνA and CHARM-II are ideal to probe these models. Once produced, ν_4 is then expected to decay promptly inside of the detector, setting a requirement on its lifetime. The mass of the heavy neutrino also controls the angular distribution of the signal with respect to the beam. The lighter ν_4 is, the more forward the signal will be. The produced Z' is required to decay into an overlapping e^+e^- pair, setting a lower bound on its mass of a few MeV. To summarize, increasing $m_{Z'}$ has two effects. On one hand, it increases the ratio of diffractive to coherent upscattering, and on the other hand, it makes the electron pair less collimated. Even though we focus on overlapping e^+e^- pairs, we note that a significant fraction of events would appear as well-separated electrons or as a pair of electrons with large energy asymmetry, similarly to the neutral current π^0 events. The asymmetric events also contribute to the MiniBooNE excess and can also be looked for in $\nu - e$ scattering analyses.

Analysis – Neutrino-electron scattering measurements at MINERνA and CHARM-II predicate their cuts in the following core ideas: no hadronic activity near the interaction vertex, small opening angle from the beam, $E_e\theta^2 < 2m_e$, and the requirement that the measured energy deposition dE/dx be consistent with that of a single electron. When the coherent process dominates and the mass of the Z' is small, the first two conditions are satisfied. However, the requirement of a single-electron-like energy deposition removes a significant fraction of the new-physics induced events. This presents a challenge, as the

signal events are mostly overlapping electron pairs and will potentially be removed by the dE/dx cut. In order to circumvent this problem, we do our analysis not at the final-cut level, but at an intermediate one. The CHARM-II experiment provides data as a function of $E_e\theta^2$ without the dE/dx cut, and in the case of MINERνA we have access to the data as a function of the measured dE/dx after analysis cuts on $E_e\theta^2$.

We briefly describe the main features of the MINERνA event selection here (for more details see [177]). The minimum electron energy required is 0.8 GeV in order to remove the π^0 background and have reliable angular and energy reconstruction. Events are kept only when they meet the following angular separation criterion: $E_e\theta^2 < 3.2 \times 10^{-3}$ GeV rad^2. A final cut is applied, ensuring $dE/dx < 4.5$ MeV/1.7 cm. The MINERνA analysis uses the data outside the previous dE/dx cut to contrain backgrounds. This sideband is defined as all events with $E_e\theta^2 > 5 \times 10^{-3}$ GeV rad^2 and $dE/dx < 20$ MeV/1.7 cm. Using this sideband measurement, the collaboration tunes their backgrounds by (0.76, 0.64, 1.0) for (ν_eCCQE, ν_μNC, ν_μCCQE) processes. We perform our analysis with the data shown in Fig. 3 of [177] where all the cuts are applied except for the final dE/dx cut. We have developed our own Monte Carlo (MC) to simulate candidate electron pair events; in our MC simulation, detector-resolution effects are assumed to be Gaussian with appropriate widths taken from [171]. We only consider the coherent part of the cross section to avoid hadronic-activity cuts, which is conservative. We also select only events with small energy asymmetries and small opening electron angles. We calculate the mean dE/dx in plastic scintillators [248] according to [249, 250]. In our final event selection, we require that the sum of the energy deposited by each electron be more than 4.5 MeV/1.7 cm, which yields an efficiency of 90%. We obtain the expected size of neutrino-electron scattering and background events in this range from Fig. 3 of [177]. To place our limits, we perform a rate-only analysis by means of a χ^2 test statistic. We incorporate uncertainties in background size and flux normalization as nuisance parameters with Gaussian constraint terms. For the neutrino electron scattering and BSM signal, we allow the normalization to scale proportionally to the same flux uncertainty parameter. The background term also scales with the flux-uncertainty parameter but has an additional nuisance parameter to account for its unknown size. We obtain our constraint as a function of heavy neutrino mass m_4, and mixing $|U_{\mu 4}|$ assuming with two degrees of freedom [250]. In our nominal MINERνA analysis, we allow for 30% uncertainty on the background motivated by the amount
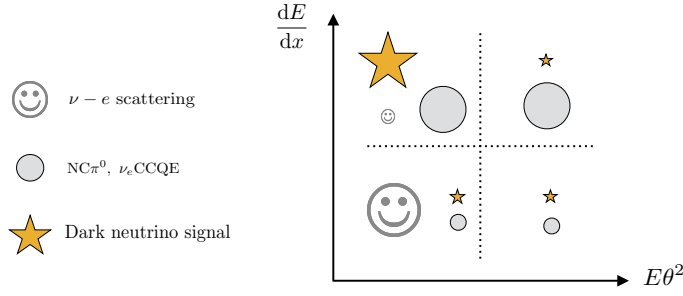
Fig. 6.3. A schematic representation of the relative number of events in sideband regions of neutrino-electron scattering analyses.

of tuning performed on the original backgrounds. Note that the nominal background predictions in the MINERνA analysis overpredicts the data before tuning, and that tuning parameters are measured at the 3% level [133]. We also perform a background-ignorant analysis in which we assume 100% uncertainty for the background normalization, which changes our conclusions by only less than a factor of two. This emphasizes the robustness of our MINERνA bound, since the NP typically overshoots the low number of events in the sideband.

6.1   Using neutrino-electron scattering data

Our CHARM-II analysis is mostly based on Fig. 1 of [179]. This sample is shown as a function of $E\theta^2$ and does not have any cuts on dE/dx. The NP signal lies mostly in a region with small $E\theta^2$. Thus, we constrain backgrounds using the data from $30 < E\theta^2 < 60$ MeV rad^2. This sideband measurement constrains the normalization of the backgrounds in the signal region at the level of 3%. The extrapolation of the shape of the background to the signal region introduces the largest uncertainty in our analysis. For this reason, we raise the uncertainty of the background normalization from 3% to a conservative 10% when setting the limits. Flux uncertainties are assumed to be 4% [251] and are applicable to the new-physics signal, $\nu - e$ scattering prediction, and backgrounds. Our χ^2 test is similar to the one used in the MINERνA analysis and carries normalization nuisance parameters for the background and flux predictions. Uncertainties in the $\nu - e$ scattering cross sections are expected to be sub-dominant and are neglected in the analysis [19].

We have performed our own fit to the MiniBooNE energy spectrum using the data release
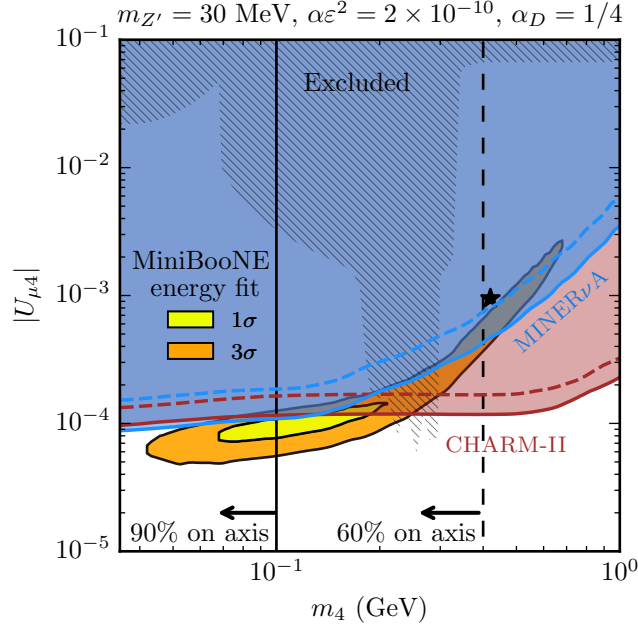
Fig. 6.4. *New constraints on mass generation model as a MiniBooNE explanation.* The MiniBooNE region of interest from [13], only fitted to the energy distribution, is shown as closed yellow (orange) regions for one (three) sigma C.L. The benchmark point, chosen to provide a good angular distribution fit, is shown as a black star. Exclusion from heavy neutrino searches is shown as a hatched background. Our new constraints at 90% C.L. using MINERνA are shown in blue for our nominal 30% background normalization uncertainty (solid) and conservative case of 100% background uncertainty (dashed). Our CHARM-II bound is shown in cherry red, where the 3% background normalization from the sideband is shown as a solid curve and the conservative 10% case as a dashed curve. The solid vertical black line at 100 MeV signals the point where 90% of NP events lie in the most forward bin in the MiniBooNE angular distribution, and the dashed one where 60% of events do so. Other relevant assumed parameters are shown above the plot; changing them does not change our conclusion.

from [195], and our results agree with [13]. The data release, however, only contains information about the neutrino energy and baseline distance. Thus, the re-weighting procedure for the model of interest can only be performed approximately. A proper analysis can be performed only if true and reconstructed electron angles and energies per simulated event are given.

Results and conclusions – The resulting limits at 90% confidence level (CL) in the $|U_{\mu 4}|$ vs m_4 plane are shown in Fig. 6.4, together with the MiniBooNE fit from [13]. For comparison, we have chosen the same values of ε, α_D, and $m_{Z'}$ as used in [13]. We note that the MiniBooNE event rate scales identically to our signal rate in all the couplings, and the dependence of our bounds on $m_{Z'}$ is subleading due to the large Q^2 involved. This implies that changing the values of these parameters does not modify the overall conclusions of our

work. In addition, one can lower the value of $m_{Z'}$ to only around 10 MeV before hitting beam dump constraints [6]. On the other hand, for this realization of the model, larger $m_{Z'}$ implies larger values of m_4, increasing the tension between the MiniBooNE fit and our bounds. Our results from MINERνA and CHARM-II are compatible given that they impose similar constraints for $m_4 \lesssim 200$ MeV. For larger masses, the kinematics of the signal becomes less forward and the production thresholds start being important. This explains the upturns visible in our bounds, where we observe it first in MINERνA and later in CHARM-II as we increase m_4, since CHARM-II has higher beam energy and the neutrino flux peaks at approximately 20 GeV.

The preferred region of [13] results from doing an energy-spectrum only fit to the MiniBooNE data. This neglects the angular distribution of the MiniBooNE excess. The preferred region of this energy-only fit is excluded by our analysis for masses of m_4 greater than ≈ 250 MeV. As was recently pointed out in [252], reasonable angular distribution of NP explanations of the MiniBooNE excess requires hundreds of MeV NP particles. Since the released MiniBooNE data do not provide the correlation between angle and energy and their associated systematics, a rigorous assessment of the tension is hard to quantify. The angular distribution of observed excess contains $\approx 50\%$ of the events in the most forward bin, with a statistical uncorrelated uncertainty of 5% on this quantity. We use this information and our calculation of the angular distribution of the NP events from our dedicated MC to give an assessment of the tension in this observable. We draw a vertical line at $m_4 = 100$ MeV, where 90% of the NP events would lie in the most forward bin and a dashed line at 60%. This 60% line, as expected, is close to the benchmark point of [237]. This consideration suggests that our analysis targets precisely the region where the model can lead to agreement in the angular data.

In the near future, the MINERνA medium-energy results on neutrino-electron scattering will be available. With the increase in energy, we estimate that it can improve the probe significantly if backgrounds, which are also rising, are well understood. This class of analyses will thus greatly benefit from improved calculations and measurements of coherent π^0 production and single-photon emitting processes. This is particularly important if an excess is observed in these channels. A complementary result can also be obtained by measuring this process in NOνA, which will sample a different kinematic regime as its

off-axis beam peaks at lower energies and expects fewer $NC\pi^0$ events per ton. Interestingly, we note that this class of BSM signatures could be lurking in current measurements of π^0 production, *e.g.*, at MINOS [253] and MINERνA [254]. The latter measurement observes a significant excess of diffractive events, which are abundant in similar realizations of this NP model [123]. To summarize, a variety of measurements are underway to further lay siege to this explanation of the MiniBooNE observation and, simultaneously, start probing testable neutrino mass generation models, as well as other similar NP signatures. It is clear that understanding neutrino cross sections will be crucial as we move forward.

Chapter 7

The future of precision in neutrino scattering

Chapter 8

Conclusions

Particle physics is at a very important moment of its history. The Standard Model has surprised us with its unprecedent accuracy in describing particle data, but a few mysteries remain. Perhaps neutrino masses and dark matter are to the Standard Model what blackbody radiation was to classical physics in the beginning of the 20th century, a scientific revolution on the wait.

Appendix A

Phase space

In this appendix we derive some key results for the phase space treatment we use in calculating cross sections and decay rates. We begin with the factorization of N-final state phase-space factors into $N-2$ two-body ones. In general, a N-body phase space can be written as

$$\mathrm{d}\Phi_N(P, p_1, \ldots, p_N) = (2\pi)^4 \delta^4(P - \sum_i^N p_i) \prod_i^N \frac{\mathrm{d}^3 p_i}{(2\pi)^3 2E_i}. \qquad (A.0.1)$$

Focusing on the 1-2 subsystem with total momentum $p_{12} = p_1 + p_2$, we can write

$$\begin{aligned}
\mathrm{d}\Phi_N(P, p_1, \ldots, p_N) &= \int \mathrm{d}^4 p_{12} \, \delta^4(p_{12} - p_1 - p_2) \, (2\pi)^4 \delta^4(P - \sum_i^N p_i) \prod_i^N \frac{\mathrm{d}^3 p_i}{(2\pi)^3 2E_i} \\
&= \int \mathrm{d}^4 p_{12} \, \mathrm{d}\Phi_2(p_{12}, p_1, p_2) \, (2\pi)^4 \delta^4(P - p_{12} - \sum_{i=3}^N p_i) \prod_{i=3}^N \frac{\mathrm{d}^3 p_i}{(2\pi)^3 2E_i} \\
&= \int \mathrm{d}^4 p_{12} \, \mathrm{d}m_{12}^2 \, \delta(p_{12}^2 - m_{12}^2) \, \mathrm{d}\Phi_2(p_{12}, p_1, p_2) \\
&\qquad \times (2\pi)^4 \delta^4(P - p_{12} - \sum_{i=3}^N p_i) \prod_{i=3}^N \frac{\mathrm{d}^3 p_i}{(2\pi)^3 2E_i},
\end{aligned}$$

$$\qquad (A.0.2)$$

which from

$$\int \mathrm{d}^4 p_{12} \, \delta(p_{12}^2 - m_{12}^2) = \int \mathrm{d}^4 p_{12} \, \frac{\delta(E_{12} - \sqrt{m_{12}^2 + |\vec{p}_{12}|^2})}{2\sqrt{m_{12}^2 + |\vec{p}_{12}|^2}} = \int \frac{\mathrm{d}^3 p_{12}}{2E_{12}},$$

yields the final results

$$\mathrm{d}\Phi_N(P, p_1, \ldots, p_N) = \frac{\mathrm{d}m_{12}^2}{2\pi}\mathrm{d}\Phi_2(p_{12}, p_1, p_2)\mathrm{d}\Phi_N(P, p_{12}, p_3, \ldots, p_N). \qquad \text{(A.0.3)}$$

This result not only lets us factorize any resonant features in phase space, but also provides a recipe to tackle the kinematics of any process. It is worth noting that the 2-body phase-space factors and associated four-momenta in the center-of-mass (CM) framce can always be written as

$$\mathrm{d}\Phi_2(p_{12}, p_1, p_2) = \frac{\lambda^{1/2}\left(1, m_1^2/E_{12}^{\mathrm{CM}\,2}, m_2^2/E_{12}^{\mathrm{CM}\,2}\right)}{32\pi^2}\mathrm{d}\Omega^{\mathrm{CM}},$$

$$p_{12} = \left(E_{12}^{\mathrm{CM}}, \vec{0}\right),$$

$$p_1 = \left(\frac{E_{12}^{\mathrm{CM}\,2} + m_1^2 - m_2^2}{2E_{12}^{\mathrm{CM}\,2}}, |\vec{p}_1|\sin\theta\cos\phi, |\vec{p}_1|\sin\theta\sin\phi, |\vec{p}_1|\cos\theta\right),$$

$$p_2 = \left(\frac{E_{12}^{\mathrm{CM}\,2} + m_2^2 - m_1^2}{2E_{12}^{\mathrm{CM}\,2}}, -\vec{p}_1\right), \qquad \text{(A.0.4)}$$

where $\lambda(a, b, c) = (a - b - c)^2 - 4bc$ is the Källén function. We showed that the general phase space problem reduces to a 2-body phase space treatment provided one can work in the CM frame of every p_{ij} subsystem.

Dark-bremsstrahlung)   Here we take the Dark-Bremsstrahlung (DB) process discussed in Section **??** as an example of a 3-body phase space. In this process, the neutrino scatters off the nuclear target with momentum exchange $Q^2 = ()$.

Neutrino trident production)   Here we take the Dark-Bremsstrahlung (DB) process discussed in Section **??** as an example of a 3-body phase space. In this process, the neutrino scatters off the nuclear target with momentum exchange $Q^2 = ()$.

In this appendix we derive a phase space parametrization for neutrino trident production in terms of the momentum transfer $K^2 = 2p_1 \cdot p_2$. This is important if one wants to change variables to smooth out the integrand at low $M_{Z'}$ masses. We follow the calculation in [161] and [135], and proceed to define K^2 as one of the integration variables. The relevant Lorentz invariant phase space for the $2 \to 3$ leptonic part of the cross section is given by

$$\int \mathrm{d}^3\Pi_{\mathrm{LIPS}} = \int \frac{\mathrm{d}\vec{p_2}}{(2\pi)^3 2E_2} \frac{\mathrm{d}\vec{p_3}}{(2\pi)^3 2E_3} \frac{\mathrm{d}\vec{p_4}}{(2\pi)^3 2E_4}$$

$$(2\pi)^4 \delta^{(4)}(p_1 + q - p_2 - p_3 - p_4). \tag{A.0.5}$$

Following [161] we start by working in the frame $\vec{p_1} + \vec{q} - \vec{p_3} = 0$, putting $\vec{p_1}$ along the $\hat{z}$ direction instead. The delta function can be integrated with the $\vec{p_4}$ and $|\vec{p_2}|$ integrals, such that

$$\int \frac{\mathrm{d}\vec{p_2}}{2E_2} \frac{\mathrm{d}\vec{p_4}}{2E_4} \delta^{(4)}(p_1 + q - p_2 - p_3 - p_4) = \int \frac{|\vec{p_2}|}{4W_c} \frac{1}{E_1 E_2} \mathrm{d}K^2 \, \mathrm{d}\phi_2, \tag{A.0.6}$$

where we defined

$$|\vec{p_2}| = (W_c^2 - m_1^2)/2W_c,$$

$$W_c = q^0 + E_1 - E_3,$$

$$K^2 = 2E_1 E_2 (1 - \cos\theta_2). \tag{A.0.7}$$

Since we conserve energy and momentum in this frame, we can take $-1 \leq \cos\theta_2 \leq 1$ and $0 \leq \phi_2 \leq 2\pi$. The remaining $\vec{p_3}$ integral can be performed with the variables defined in [161] to yield

$$\int \frac{\mathrm{d}\vec{p_3}}{2E_3} = \int \frac{2\pi}{\hat{s}} \, \mathrm{d}x_5 \, \mathrm{d}x_3, \tag{A.0.8}$$

where a trivial azimuthal angle was integrated over. Their limits are more easily found in the frame $\vec{p_1} + \vec{q} = 0$, with $\vec{q}$ along the $\hat{z}$ direction. Finally, our main result is given by

$$\int \mathrm{d}^3\Pi_{\mathrm{LIPS}} = \frac{1}{(2\pi)^4} \int \frac{|\vec{p_2}|}{4W_c} \frac{1}{\hat{s}} \frac{1}{E_1 E_2} \, \mathrm{d}x_5 \, \mathrm{d}x_3 \, \mathrm{d}K^2 \, \mathrm{d}\phi_2. \tag{A.0.9}$$

There remains two non-trivial integrations to be performed to obtain the full 4-body phase space cross section, namely the ones over q^2 and $\hat{s}$. The substitutions suggested in [162] for these two invariants are still convenient, and we make use of them in our numerical

integrations.

Appendix B

Trident distributions

B.0.1 Kinematical Distributions at DUNE ND

In this section we explore the trident signal in more detail, showing some relevant kinematical distributions for coherent and diffractive events. For concreteness, and due to its large number of events, we choose to focus on the DUNE ND, only commenting slightly on the signal at the lower energies of SBN and νSTORM. The observables we calculate are the invariant mass of the charged leptons $m^2_{\ell^+\ell^-}$, their separation angle $\Delta\theta$ and their individual energies $E_\pm$. The flux convolved distributions of these observables are shown for the DUNE ND in neutrino mode in Fig. **??**. In these plots, we sum all trident channels with a given undistinguishable final-state proportionally to their rates, although ν_μ initiated processes always dominate. The coherent and diffractive contributions are shown separately and on the same axes, but we do not worry about their relative normalization. Other potentially interesting quantities are the angle between the cone formed by the two charged leptons and the beam, α_C, and the angle of each charged lepton with respect to the beam direction, $\theta_\pm$. These additional observables are explored in Appendix **??**. We also report the distributions of the momentum transfer to the hadronic system, Q^2. Although this is not a directly measurable quantity, it is a strong discriminant between the coherent and diffractive processes. We do not present the antineutrino distributions here, but they are qualitatively similar.

Perhaps one of the most valuable tools for background suppression in the measurement of the $\mu^+\mu^-$ trident signal at CHARM II, CCFR and NuTeV [10, 30, 31] was the smallness of the invariant mass $m^2_{\ell^+\ell^-}$. This feature, shown here on the top row of Fig. **??**, is also

present at lower energies, where the distributions become even more peaked at lower values; although, the diffractive events tend to be have a more uniform distribution in this variable. This is also true for the angular separation $\Delta\theta$, where coherent dimuon tridents tends to be quite collimated, with 90% of events having $\Delta\theta < 20°$, whilst diffractive ones are less so, with only 47% of events surviving the cut. This difference is much less pronounced for mixed and dielectron channels, where only half of our coherent events obey $\Delta\theta < 20°$, when 37% of diffractive events do so.

An interesting feature of same flavour tridents induced by a neutrino (antineutrino) is that the negative (positive) charged lepton tends to be slightly more energetic than its counterpart, whilst for mixed tridents muons tend to carry away most of the energy. These considerations are also reflected in the angular distributions. The most energetic particle is also the more forward one. For instance, in mixed neutrino induced tridents, $\sim 80\%$ of the μ^- are expected to be within $10°$ of the beam direction, whilst only $\sim 35\%$ of their e^+ counterparts do so (see Appendix **??** for additional distributions).

Finally, we mention that detection thresholds can also be important for trident channels with electrons in the final-state. Assuming, for example, a detection threshold for muons and electromagnetic (EM) showers of 30 MeV in LAr, we end up with efficiencies of (99%, 71%, 77%, 86%) for ($\mu^+\mu^-$, e^+e^-, $e^+\mu^-$, $e^-\mu^+$) coherent tridents. These efficiencies become (96%, 91%, 93%, 96%) for diffractive tridents, dropping for $\mu^+\mu^-$ and increasing for all others. For comparison, at the lower neutrino energies of SBND and assuming the same detection thresholds, the efficiencies for coherent and diffractive tridents are slightly lower, (97%, 57%, 67%, 77%) and (90%, 81%, 85%, 90%) respectively.

While trident events are generally quite forward going, their angular behaviour is quite interesting. We consider here the angle between the charged lepton cone and the neutrino beam, α_C, defined as

$$\cos\alpha_C = \frac{(\vec{p}_3 + \vec{p}_4) \cdot \vec{p}_1}{|\vec{p}_3 + \vec{p}_4||\vec{p}_1|} \,,$$

and in the individual angle of the charged lepton to the neutrino beam, θ. For same flavour tridents we define θ for each charge of the visible final-state, whilst for mixed tridents we use their flavour. We also show the distribution in $Q^2 = -q^2$, where $q = (P - P')$, which is of particular interest when considering coherency and the impact of form factors.
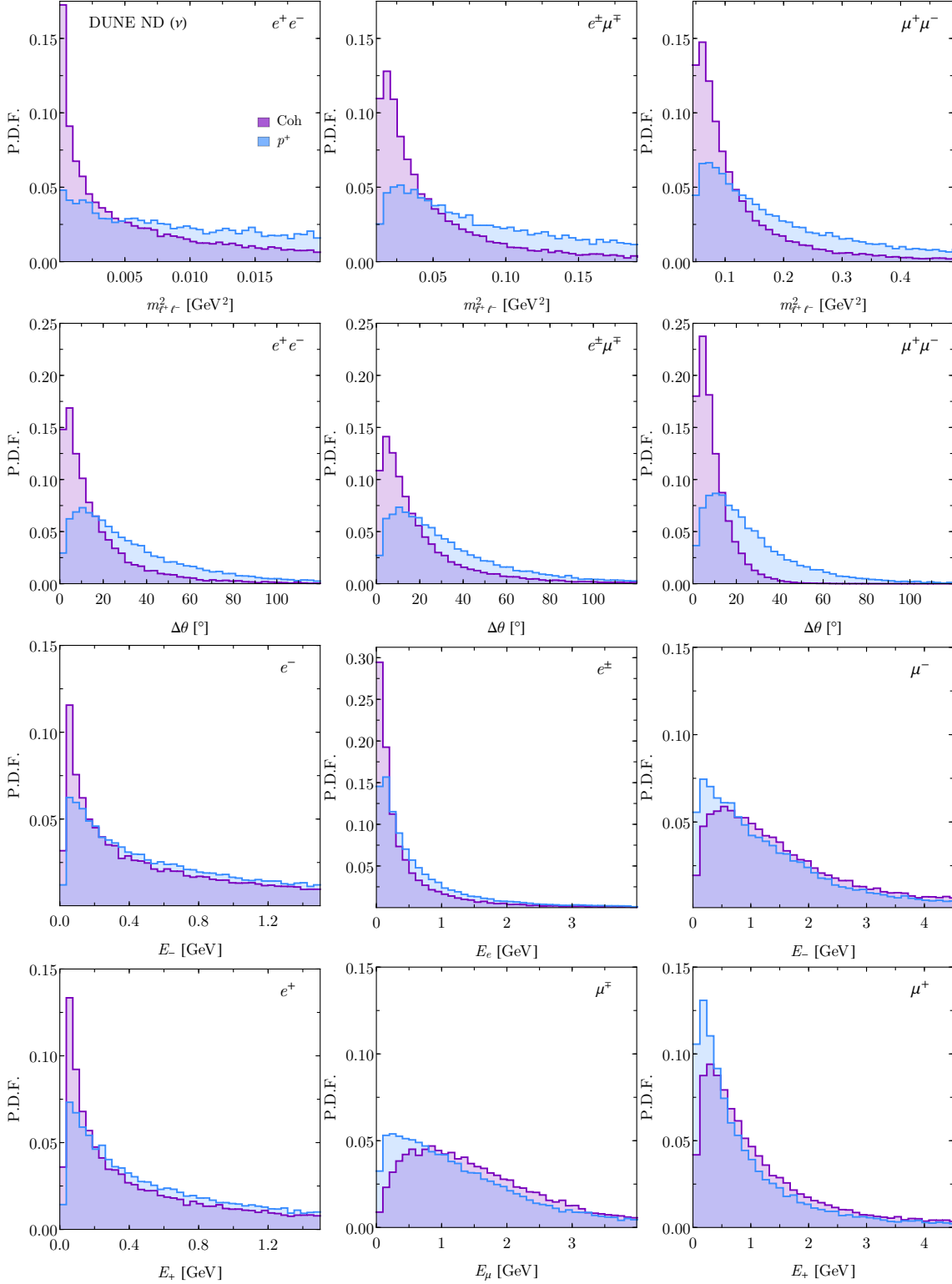
Fig. B.1. Flux convolved neutrino trident production distributions for DUNE ND in neutrino mode. In purple we show the coherent contribution in ^{40}Ar and in blue the diffractive contribution from protons as targets only (including Pauli blocking). The coherent and diffractive distributions are normalized independently. The relative importance of each contribution as a function of E_ν can be seen in Fig. 3.6.
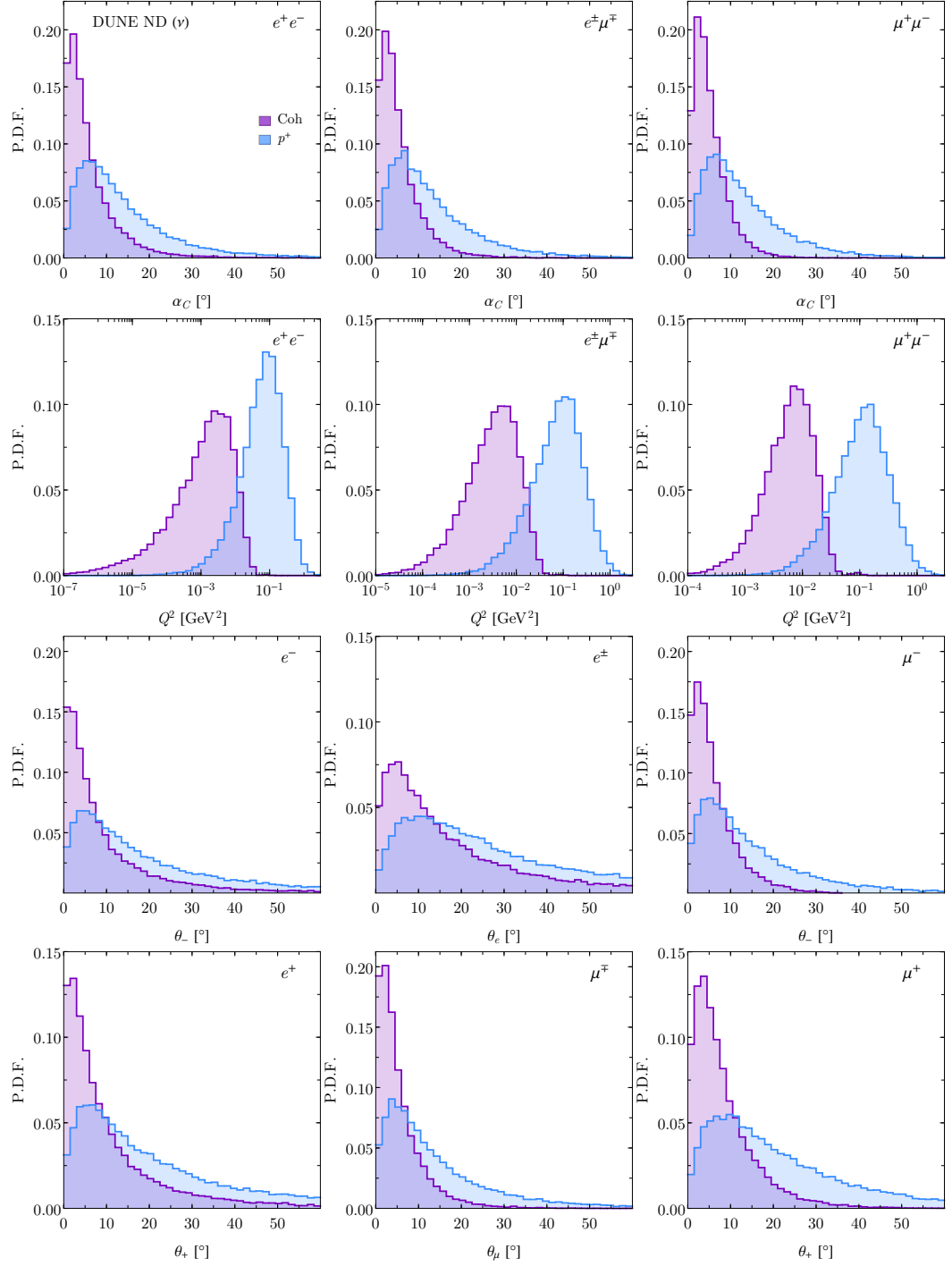
Fig. B.2. Flux convolved neutrino trident production distributions for DUNE ND in neutrino mode in additional variables. In purple we show the coherent contribution in ^{40}Ar and in blue the diffractive contribution from protons as targets only (including Pauli blocking). The coherent and diffractive distributions are normalized independently.

Appendix C

Trident rates at current facilities

C.1   Trident rates in current facilities

The search for neutrino trident production events certainly benefits from the capabilities of LAr technologies but need not be limited to it. In this section we study neutrino trident production rates at non-LAr experiments which have finished data taking or are still running: the on-axis near detector of T2K (INGRID), the near detectors of MINOS and NOνA and the MINERνA experiment. We calculate the total number of trident events as in Eq. (3.4.1), taking into account the fact that some detectors are made of composite material. We summarize in Tab. C.1 the details of all non-LAr detectors considered in this section. We limit ourselves to a discussion of the total rates in the fiducial volume, but remark that a careful consideration of each detector is needed in order to assess their true potential to detect a trident signal. For instance, requirements about low energy EM shower reconstruction, hadronic activity measurements and event containment would have to be met to a good degree in order for the detector to be competitive.

INGRID   INGRID, the on-axis near detector of the T2K experiment, is located 280 m from the beam source. It consists of 14 identical iron modules, each with a mass of 7.1 t, resulting in a total fiducial mass of 99.4 t [47]. The modules are spread over a range of angles between $0°$ and $1.1°$ with respect to the beam axis. The currently approved T2K exposure is $(3.9 + 3.9) \times 10^{21}$ POT in neutrino + antineutrino modes (T2K-I), with the goal to increase it to a total exposure of $(1 + 1) \times 10^{22}$ POT in the second phase of the

Experiment	Material	Baseline (m)	Exposure (POT)	Fiducial Mass (t)	E_ν (GeV)
T2K	Fe	280	$3.9\ (3.9) \times 10^{21}$	99.4	$0-4$
T2K-II	Fe	280	$10\ (10) \times 10^{21}$	99.4	$0-4$
MINOS	Fe and C	1040	$10.56\ (3.36) \times 10^{20}$	28.6	$0-20$
MINOS+	Fe and C	1040	9.69×10^{20}	28.6	$0-20$
NOνA	C_2H_3Cl and CH_2	1000	$8.85\ (6.9)\ \times 10^{20}$	231	$0-20$
NOνA-II	C_2H_3Cl and CH_2	1000	$36\ (36) \times 10^{20}$	231	$0-20$
MINERνA	CH, H_2O, Fe, Pb, C	1035	$12\ (12) \times 10^{20}$	7.98	$0-20$

Tab. C.1. Summary of the non-LAr detector set-up and values used in our calculations. The POT numbers are given for a neutrino (antineutrino) beam.

experiment (T2K-II) [50]. Hence we expect approximately 2.6 times more trident events for T2K-II.

We use the on-axis neutrino mode flux spectra at the INGRID module-3 from Ref. [48]. The flux contribution for each neutrino flavour and energy range is listed in Table 1 of Ref. [48]. We assume here that the fluxes at the other 13 modules are the same as at module-3. Although this is not exactly correct it should provide a reasonable estimate of the total rate.

MINOS/MINOS+ Near Detector   The MINOS near detector is a magnetized, coarse-grained tracking calorimeter, made primarily of steel and plastic scintillator. Placed 1.04 km away from the NuMI target at Fermilab [255], it weighs 980 t and is similar to the far detector in design. In our analysis, we assume a similar fiducial volume cut to the standard ν_μ CC analyses, namely a fiducial mass of 28.6 t made of 80% of iron and 20% of carbon [256].

The experiment ran from 2005 till 2012 in the low energy (LE) configuration of the NuMI beam ($E_\nu^{\text{peak}} \approx 3$ GeV) and collected 10.56×10^{20} (3.36×10^{20}) POT in the neutrino (antineutrino) beam [257]. The successor to MINOS, MINOS+, ran with the same detectors subjected to the medium energy (ME) configuration of the NuMI beam ($E_\nu^{\text{peak}} \approx 7$ GeV) from 2013 to 2016, and has collected 9.69×10^{20} POT in the neutrino mode. To calculate the trident event rates we use the fluxes taken from Ref. [258]. We assume that the MINOS+ neutrino flux is identical to the one at the MINERνA experiment (see section **??**). Although the cross section for iron is about two times larger than for argon and the neutrino fluxes similar, the number of trident events at MINOS ND is much smaller than the expected one at DUNE ND due to a lower exposure and fiducial mass. The stringent

cut on the fiducial volume assumed here implies a reduction from the 980 t near detector bulk mass to 28.6 t. This cut can be relaxed, depending on the signature considered, and may significantly enhance the rates we quote. A careful analysis of trident signatures outside the fiducial volume would be necessary, but we point out that our rates can increase by at most a factor of ≈ 30.

NOνA Near Detector   The NOνA near detector is a fine grained low-Z liquid-scintillator detector placed off-axis from the NuMI beam at a distance of 1 km. Its total mass is 330 t, with almost 70% of it active mass (231 t). In this estimate we assume all of this active mass to also be fiducial. The detector material is approximately 70% mineral oil (CH_2) and 30% of PVC (C_2H_3Cl) [55]. A total exposure of $8.85\,(6.9) \times 10^{20}$ POT has been collected in the neutrino (antineutrino) beam mode prior to 2018 [56].

The NOνA ND neutrino fluxes (taken from Ref. [258]) peak at slightly lower energies than the MINOS or MINERνA ones, $E_\nu^{\mathrm{peak}} \approx 2$ GeV. The flavour composition is 91% (11%) ν_μ and 8% (88%) $\overline{\nu}_\mu$ in the neutrino (antineutrino) mode and about 1% $\nu_e + \overline{\nu}_e$ in each mode.

Comparing NOνA and MINOS, we see that while NOνA ND has a fiducial mass almost 8 times larger, the flux times total cross section at MINOS ND is at least two orders of magnitude larger than at NOνA ND, especially above 4 GeV, making the rates at MINOS ND larger than the rates at NOνA ND.

NOνA is planning to collect a total exposure of $36\,(36) \times 10^{20}$ POT in the neutrino (antineutrino) mode (NOνA-II) [56, 259], making the expected rates almost 4.1(5.2) times larger (shown in Tab. C.2). In this case the expected dimuons and mixed events at MINOS+ would be at least two times larger than NOνA-II. On the other hand, for NOνA-II there will be two times more dielectron events given the much higher exposure.

MINERνA   The multi-component MINERνA detector was mainly designed to measure neutrino and antineutrino interaction cross sections with different nuclei in the 1-20 GeV range of energy [52]. The detector is located at 1.035 km from the NuMI target. We assume a fiducial mass of about 8 t, with a composition of 75% CH, 9% Pb, 8% Fe, 6% H_2O and 2% C. The experiment has collected 12×10^{20} POT in the neutrino mode and is planning to reach the same exposure in the antineutrino mode by 2019, both using the medium

energy flux of NuMI beam configuration. We do not include the low energy runs, as these have lower number of POT and lower neutrino energies. The neutrino (antineutrino) beam is composed of 95% (7%) ν_μ and 4% (92%) $\overline{\nu}_\mu$, both beams have about 1% of $\nu_e + \overline{\nu}_e$. As expected, the event rate is lower than at MINOS+, as the latter has a larger fiducial mass. MINERνA, however, benefits from its fine grained technology and its dedicated design for cross section measurements.

Channel	T2K-I	T2K-II	MINOS	MINOS+	NOνA-I	NOνA-II	MINERνA
$\nu_\mu \to \nu_e e^+ \mu^-$	538	1379	179 (25)	688	71 (14)	291 (73)	140 (13)
	49	126	21 (3)	82	21 (4)	86 (21)	30 (3)
$\overline{\nu}_\mu \to \overline{\nu}_e e^- \mu^+$	23	58	42 (31)	38	10 (57)	41 (296)	8 (89)
	2	5	5 (4)	5	3 (17)	12 (88)	2 (19)
$\nu_e \to \nu_\mu e^- \mu^+$	2	6	1 (0.2)	4	2 (0.5)	8 (3)	1 (0.09)
	0.3	1	0.3 (0.04)	0.8	0.9 (0.2)	4 (1)	0.3 (0.03)
$\overline{\nu}_e \to \overline{\nu}_\mu e^+ \mu^-$	0.2	0.6	0.4 (0.3)	0.4	0.5 (0.9)	2 (5)	0.06 (0.5)
	0.04	0.1	0.08 (0.06)	0.08	0.2 (0.4)	0.8 (2)	0.02 (0.2)
Total $e^\pm \mu^\mp$	563	1444	222 (56)	730	83 (72)	340 (374)	149 (102)
	52	132	27 (7)	88	25 (22)	102 (114)	32 (22)
$\nu_\mu \to \nu_\mu e^+ e^-$	257	659	48 (5)	44	22 (3)	90 (16)	35 (3)
	9	23	3 (0.4)	3	3 (0.6)	00	4 (0.4)
$\overline{\nu}_\mu \to \overline{\nu}_\mu e^- e^+$	10	26	9 (8)	9	2 (16)	8 (83)	2 (23)
	0.4	1	0.7 (0.5)	0.7	0.4 (3)	2 (15)	0.2 (3)
$\nu_e \to \nu_e e^- e^+$	9	24	3 (0.3)	8	3 (0.9)	12 (5)	2 (0.2)
	0.3	0.8	0.2 (0.03)	0.6	0.7 (0.2)	3 (1)	0.2 (0.02)
$\overline{\nu}_e \to \overline{\nu}_e e^+ e^-$	0.9	2	0.7 (0.6)	0.7	0.8 (2)	3 (10)	0.1 (0.9)
	0.03	0.08	0.06 (0.04)	0.05	0.2 (0.3)	0.8 (1)	0.01 (0.1)
Total $e^+ e^-$	277	711	61 (15)	62	29 (22)	119 (114)	39 (27)
	10	25	4 (1)	4	4 (4)	16 (21)	4 (3)
$\nu_\mu \to \nu_\mu \mu^+ \mu^-$	29	73	21 (3)	81	7 (2)	28 (11)	17 (2)
	15	38	8 (1)	33	7 (2)	29 (10)	12 (1)
$\overline{\nu}_\mu \to \overline{\nu}_\mu \mu^- \mu^+$	1	3	5 (3)	5	1 (7)	4 (35)	1 (11)
	0.7	2	2 (1)	2	1 (6)	4 (30)	0.7 (8)
$\nu_e \to \nu_e \mu^+ \mu^-$	0.09	0.2	0.09 (0.01)	0.3	0.1 (0.04)	0.4 (0.2)	0.06 (0.007)
	0.04	0.1	0.03 (0.004)	0.1	0.1 (0.03)	0.4 (0.1)	0.03 (0.004)
$\overline{\nu}_e \to \overline{\nu}_e \mu^+ \mu^-$	0.01	0.03	0.03 (0.02)	0.03	0.04 (0.06)	0.2 (0.3)	0.004 (0.03)
	0.004	0.01	0.01 (0.009)	0.01	0.03 (0.05)	0.1 (0.3)	0.003 (0.02)
Total $\mu^+ \mu^-$	30	76	26 (6)	86	9 (9)	37 (47)	18 (13)
	16	40	10 (2)	35	8 (8)	34 (36)	13 (9)

Tab. C.2. Total number of **coherent** (top row) and **diffractive** (bottom row) trident events expected at different non-LAr detectors for each channel. The numbers in parentheses are for the antineutrino running mode, when present. These calculations consider a detection efficiency of 100%.

Appendix D

One loop ν masses in Type-I seesaw

D.1   Type-I seesaw neutrino masses in the SM

In this appendix, we compute the one-loop corrections to the light neutrino masses in the SM, following Refs. [260–262].

We work with the on-shell (OS) renormalization scheme. This is ensured by requiring that the off-diagonal elements of the self-energy be diagonal when the external particles are on their mass shell, and that the residue of the renormalized propagator are equal to one. Note this is only applicable to the off-diagonal entries that involve at least one heavy neutrino, and that the light-light entries are all non-zero and finite at one-loop.

Assuming Majorana neutrino fields, one can write the self-energy tensor in its most general form:

$$\Sigma_{ij}(\slashed{q}) = \slashed{q}P_L\Sigma_{ij}^L(q^2) + \slashed{q}P_R\Sigma_{ij}^R(q^2) + P_L\Sigma_{ij}^M(q^2) + P_R\Sigma_{ij}^{M*}(q^2), \qquad (D.1.1)$$

where by virtue of the Majorana nature the previous terms obey

$$\Sigma_{ij}^L(q^2) = \Sigma_{ij}^{R*}(q^2), \qquad \Sigma_{ij}^M(q^2) = \Sigma_{ji}^M(q^2).$$

D.1.1   Self-energy

We now compute explicitly the self-energy corrections. The contribution from the scalar fields $s = h^0, \varphi^0$, the goldstones $G = G_h, G_\varphi$ and the vector bosons $V = Z, Z'$ are

$$-i\,\Sigma_{ij}^{s}(p^2) = (-i)^2 \left(\Delta_s P_R + \Delta_s^* P_L\right)_{ik} \times$$
$$\int \frac{d^d k}{(2\pi)^d} \frac{i(\not{p} + \not{k} + m_k)}{(p+k)^2 - m_k^2} \frac{i}{k^2 - m_s^2} \left(\Delta_s P_R + \Delta_s^* P_L\right)_{kj},$$

$$-i\,\Sigma_{ij}^{G}(p^2) = (-i)^2 \left(i\,\Delta_G P_R + i\,\Delta_G^* P_L\right)_{ik} \times$$
$$\int \frac{d^d k}{(2\pi)^d} \frac{i(\not{p} + \not{k} + m_k)}{(p+k)^2 - m_k^2} \frac{i}{k^2 - \xi_V m_V^2} \left(i\,\Delta_G P_R + i\,\Delta_G^* P_L\right)_{kj},$$

$$-i\,\Sigma_{ij}^{G}(p^2) = -(-i)^2 \gamma^\mu \left(C_V P_L - C_V^T P_R\right)_{ik} \times$$
$$\int \frac{d^d k}{(2\pi)^d} \frac{i(\not{p} + \not{k} + m_k)}{(p+k)^2 - m_k^2} \frac{iP_{\mu\nu}}{k^2 - m_V^2} \gamma^\nu \left(C P_L - C^T P_R\right)_{kj},$$

with no index summation notation. In the latter term, we defined the vector boson propagator numerator, which we rewrite as

$$\gamma^\mu P_{\mu\nu} \gamma^\nu = \gamma^\mu \left[g_{\mu\nu} - (1 - \xi_V) \frac{k_\mu k_\nu}{k^2 - \xi_V m_V^2} \right] \gamma^\nu$$
$$= d - (1 - \xi_V) \frac{k^2 - m_k^2}{k^2 - \xi_V m_V^2} - \frac{m_k^2}{m_V^2} \frac{(k^2 - \xi_V m_V^2) - (k^2 - m_V^2)}{k^2 - \xi_V m_V^2}.$$

This allows us to write the relevant part of the self-energy as functions of the scalar two-point loop function

$$B_0(l, m_a^2, m_c^2) = \mu^{2\epsilon} \int \frac{d^d k}{(2\pi)^d} \frac{1}{(k^2 - m_a^2)((l+k)^2 - m_c^2)}, \tag{D.1.2}$$

such that

$$\Sigma_{ij}^{s}(0)\, P_R = -\frac{\pi^2}{(2\pi)^4} \mu^{d-4} \left[(\Delta_s)_{ik} m_k B_0(0, m_k^2, m_s^2)(\Delta_s)_{kj} \right] P_R \tag{D.1.3}$$

$$\Sigma_{ij}^{G}(0)\, P_R = \frac{\pi^2}{(2\pi)^4} \mu^{d-4} \left[(\Delta_G)_{ik} m_k B_0(0, m_k^2, \xi_V m_V^2)(\Delta_G)_{kj} \right] P_R \tag{D.1.4}$$

$$\Sigma_{ij}^{V}(0)\, P_R = -\frac{\pi^2}{(2\pi)^4} \mu^{d-4} \left[(C_V)_{ik} m_k\, f(m_k^2, m_V^2, \xi m_V^2)(C_V^*)_{kj} \right] P_R, \tag{D.1.5}$$

where the rearrangement of the boson propagator allowed us to write $f(m_k^2, m_V^2, \xi m_V^2)$ as

$$f(m_k^2, m_V^2, \xi m_V^2) = d\, B_0(0, m_k^2, m_V^2) - (1 - \xi_V) B_0(0, m_V^2, \xi_V m_V^2) +$$
$$\frac{m_k^2}{m_V^2} B_0(0, m_k^2, \xi_V m_V^2) - \frac{m_k^2}{m_V^2} B_0(0, m_k^2, m_V^2).$$

Finally, the scalar loop function is given by

$$B_0(0, m_a^2, m_b^2) = \frac{1}{\epsilon} - \gamma_E + \ln 4\pi - \int_0^1 dx \ln \frac{m_a^2 - x(m_a^2 - m_b^2)}{\mu^2}$$

$$= \frac{1}{\epsilon} - \gamma_E + \ln 4\pi - \frac{m_a^2}{m_b^2 - m_a^2}\left[\ln\frac{m_a^2}{\mu^2} - 1\right] + \frac{m_b^2}{m_b^2 - m_a^2}\left[\ln\frac{m_b^2}{\mu^2} - 1\right].$$

The finiteness of our final result and its gauge invariance are a consequence of the two following identities

$$\Delta_G = \Delta_S = C\frac{\hat{m}}{m_V} + \frac{\hat{m}}{m_V}C^T, \qquad C\hat{m}C^T = 0. \tag{D.1.6}$$

For light neutrinos $(i, j = 1, 2, 3)$, the final result reads

$$\Sigma_{ij}P_R = -\frac{\pi^2}{(2\pi)^4}C\hat{m}\left[d\,B_0(0, \hat{m}^2, m_V^2) + \frac{\hat{m}^2}{m_V^2}\left(B_0(0, \hat{m}^2, m_S^2) - B_0(0, \hat{m}^2, m_V^2)\right)\right]C^T P_R.$$

$$\tag{D.1.7}$$

Bibliography

[1] TEXONO collaboration, H. T. Wong et al., *A Search of Neutrino Magnetic Moments with a High-Purity Germanium Detector at the Kuo-Sheng Nuclear Power Station*, Phys. Rev. **D75** (2007) 012001, [`hep-ex/0605006`].

[2] TEXONO collaboration, M. Deniz et al., *Measurement of Nu(e)-bar -Electron Scattering Cross-Section with a CsI(Tl) Scintillating Crystal Array at the Kuo-Sheng Nuclear Power Reactor*, Phys. Rev. **D81** (2010) 072001, [`0911.1597`].

[3] J.-W. Chen, H.-C. Chi, H.-B. Li, C. P. Liu, L. Singh, H. T. Wong et al., *Constraints on millicharged neutrinos via analysis of data from atomic ionizations with germanium detectors at sub-keV sensitivities*, Phys. Rev. **D90** (2014) 011301, [`1405.7168`].

[4] BaBar collaboration, J. P. Lees et al., *Search for a Dark Photon in e^+e^- Collisions at BaBar*, Phys. Rev. Lett. **113** (2014) 201801, [`1406.2980`].

[5] BaBar collaboration, J. P. Lees et al., *Search for Invisible Decays of a Dark Photon Produced in e^+e^- Collisions at BaBar*, Phys. Rev. Lett. **119** (2017) 131804, [`1702.03327`].

[6] M. Bauer, P. Foldenauer and J. Jaeckel, *Hunting All the Hidden Photons*, JHEP **07** (2018) 094, [`1803.05466`].

[7] BaBar collaboration, J. P. Lees et al., *Search for a muonic dark force at BABAR*, Phys. Rev. **D94** (2016) 011102, [`1606.03501`].

[8] ATLAS collaboration, G. Aad et al., *Measurements of Four-Lepton Production at the Z Resonance in pp Collisions at $\sqrt{s} = 7$ and 8 TeV with ATLAS*, Phys. Rev. Lett. **112** (2014) 231806, [`1403.5657`].

[9] Y. Kaneta and T. Shimomura, *On the possibility of a search for the $L_\mu - L_\tau$ gauge boson at Belle-II and neutrino beam experiments*, *PTEP* **2017** (2017) 053B04, [`1701.00156`].

[10] CCFR collaboration, S. R. Mishra et al., *Neutrino tridents and W Z interference*, *Phys. Rev. Lett.* **66** (1991) 3117–3120.

[11] W. Altmannshofer, S. Gori, M. Pospelov and I. Yavin, *Neutrino Trident Production: A Powerful Probe of New Physics with Neutrino Beams*, *Phys. Rev. Lett.* **113** (2014) 091801, [`1406.2332`].

[12] M. Escudero, D. Hooper, G. Krnjaic and M. Pierre, *Cosmology With a Very Light $L_\mu - L_\tau$ Gauge Boson*, `1901.02010`.

[13] E. Bertuzzo, S. Jana, P. A. N. Machado and R. Zukanovich Funchal, *Dark Neutrino Portal to Explain MiniBooNE excess*, *Phys. Rev. Lett.* **121** (2018) 241801, [`1807.09877`].

[14] A. Fradette, M. Pospelov, J. Pradler and A. Ritz, *Cosmological beam dump: constraints on dark scalars mixed with the Higgs boson*, *Phys. Rev.* **D99** (2019) 075004, [`1812.07585`].

[15] V. Silveira and A. Zee, *SCALAR PHANTOMS*, *Phys. Lett.* **161B** (1985) 136–140.

[16] N. Craig, C. Englert and M. McCullough, *New Probe of Naturalness*, *Phys. Rev. Lett.* **111** (2013) 121803, [`1305.5251`].

[17] S. M. Boucenna, S. Morisi and J. W. F. Valle, *The low-scale approach to neutrino masses*, *Adv. High Energy Phys.* **2014** (2014) 831598, [`1404.3751`].

[18] W. J. Marciano and Z. Parsa, *Neutrino electron scattering theory*, *J. Phys.* **G29** (2003) 2629–2645, [`hep-ph/0403168`].

[19] A. de Gouvea and J. Jenkins, *What can we learn from neutrino electron scattering?*, *Phys. Rev.* **D74** (2006) 033004, [`hep-ph/0603036`].

[20] A. N. Khan, *Global analysis of the source and detector nonstandard interactions using the short baseline $\nu - e$ and $\bar{\nu} - e$ scattering data*, *Phys. Rev. D* **93** (May, 2016) 093019.

[21] M. Lindner, F. S. Queiroz, W. Rodejohann and X.-J. Xu, *Neutrino-electron scattering: general constraints on Z' and dark photon models*, *JHEP* **05** (2018) 098, [1803.00060].

[22] J. N. Bahcall, M. Kamionkowski and A. Sirlin, *Solar neutrinos: Radiative corrections in neutrino - electron scattering experiments*, *Phys. Rev.* **D51** (1995) 6146–6158, [astro-ph/9502003].

[23] M. Passera, *QED corrections to neutrino electron scattering*, *Phys. Rev.* **D64** (2001) 113002, [hep-ph/0011190].

[24] W. Czyz, G. C. Sheppey and J. D. Walecka, *Neutrino production of lepton pairs through the point four-fermion interaction*, *Nuovo Cim.* **34** (1964) 404–435.

[25] J. Lovseth and M. Radomiski, *Kinematical distributions of neutrino-produced lepton triplets*, *Phys. Rev.* **D3** (1971) 2686–2706.

[26] K. Fujikawa, *The self-coupling of weak lepton currents in high-energy neutrino and muon reactions*, *Annals Phys.* **68** (1971) 102–162.

[27] R. W. Brown, *Intermediate boson. i. theoretical production cross-sections in high-energy neutrino and muon experiments*, *Phys. Rev.* **D3** (1971) 207–223.

[28] K. Koike, M. Konuma, K. Kurata and K. Sugano, *Neutrino production of lepton pairs. 1. -*, *Prog. Theor. Phys.* **46** (1971) 1150–1169.

[29] G. Magill and R. Plestid, *Neutrino Trident Production at the Intensity Frontier*, *Phys. Rev.* **D95** (2017) 073004, [1612.05642].

[30] CHARM-II collaboration, D. Geiregat et al., *First observation of neutrino trident production*, *Phys. Lett.* **B245** (1990) 271–275.

[31] NuTeV collaboration, T. Adams et al., *Neutrino trident production from NuTeV*, in *High-energy physics. Proceedings, 29th International Conference, ICHEP'98, Vancouver, Canada, July 23-29, 1998. Vol. 1, 2*, pp. 631–634, 1998, hep-ex/9811012.

[32] R. W. Brown, R. H. Hobbs, J. Smith and N. Stanko, *Intermediate boson. iii. virtual-boson effects in neutrino trident production*, *Phys. Rev.* **D6** (1972) 3273–3292.

[33] I. V. Gaidaenko, V. A. Novikov and M. I. Vysotsky, *On the production of a lepton pair in the collision of ultrarelativistic neutral particle with nonzero magnetic moment with nuclei*, *Phys. Lett.* **B497** (2001) 49–54, [hep-ph/0007204].

[34] W. Altmannshofer, S. Gori, M. Pospelov and I. Yavin, *Neutrino Trident Production: A Powerful Probe of New Physics with Neutrino Beams*, *Phys. Rev. Lett.* **113** (2014) 091801, [1406.2332].

[35] S.-F. Ge, M. Lindner and W. Rodejohann, *New Physics and Atmospheric Neutrino Trident Production with PINGU and ORCA*, 1702.02617.

[36] G. Magill and R. Plestid, *Probing new charged scalars with neutrino trident production*, *Phys. Rev.* **D97** (2018) 055003, [1710.08431].

[37] A. Falkowski, G. Grilli di Cortona and Z. Tabrizi, *Future DUNE constraints on EFT*, *JHEP* **04** (2018) 101, [1802.08296].

[38] R. Belusevic and J. Smith, *W - Z Interference in Neutrino - Nucleus Scattering*, *Phys. Rev.* **D37** (1988) 2419.

[39] M. A. Kozhushner and E. P. Shabalin, *Production of lepton particle pairs on a Coulomb center*, *Sov. Phys. JETP* **14** (1962) 676.

[40] E. P. Shabalin, *The $\mu^+\mu^-$ and e^+e^- pair production cross sections for neutrinos scattered by nuclei*, *Sov. Phys. JETP* **16** (1963) 125.

[41] R. Acciarri et al., *A Proposal for a Three Detector Short-Baseline Neutrino Oscillation Program in the Fermilab Booster Neutrino Beam*, 1503.01520.

[42] DUNE collaboration, R. Acciarri et al., *Long-Baseline Neutrino Facility (LBNF) and Deep Underground Neutrino Experiment (DUNE)*, 1601.02984.

[43] D. DUNE Collaboration, R. Acciarri et al., *Long-Baseline Neutrino Facility (LBNF) and Deep Underground Neutrino Experiment (DUNE) Conceptual Design Report Volume 2: The Physics Program for DUNE at LBNF*, 1512.06148.

[44] F. J. P. Soler, *nuSTORM: Neutrinos from Stored Muons*, in *Proceedings, Topical Research Meeting on Prospects in Neutrino Physics (NuPhys2014): London, UK, December 15-17, 2014*, 2015, `1507.08836`.

[45] D. Adey, R. Appleby, R. Bayes, A. Bogacz, A. Bross, J.-B. Lagrange et al., *Overview of the neutrinos from stored muons facility - nustorm*, *Journal of Instrumentation* **12** (2017) P07020.

[46] C. Andreopoulos et al., *The GENIE Neutrino Monte Carlo Generator*, *Nucl. Instrum. Meth.* **A614** (2010) 87–104, [`0905.2517`].

[47] K. Abe et al., *Measurements of the T2K neutrino beam properties using the INGRID on-axis near detector*, *Nucl. Instrum. Meth.* **A694** (2012) 211–223, [`1111.3119`].

[48] T2K collaboration, K. Abe et al., *Measurement of the muon neutrino inclusive charged-current cross section in the energy range of 1–3 GeV with the T2K INGRID detector*, *Phys. Rev.* **D93** (2016) 072002, [`1509.06940`].

[49] T2K collaboration, K. Abe et al., *Measurement of Coherent π^+ Production in Low Energy Neutrino-Carbon Scattering*, *Phys. Rev. Lett.* **117** (2016) 192501, [`1604.04406`].

[50] T2K collaboration, K. Abe et al., *Sensitivity of the T2K accelerator-based neutrino experiment with an Extended run to 20×10^{21} POT*, `1607.08004`.

[51] MINERvA collaboration, O. Altinok et al., *Measurement of ν_μ charged-current single π^0 production on hydrocarbon in the few-GeV region using MINERvA*, *Phys. Rev.* **D96** (2017) 072003, [`1708.03723`].

[52] MINERvA collaboration, "MINERvA Status Report and Request for 12×10^{20} POT in Antineutrino Mode." 2017.

[53] MINOS collaboration, P. Adamson et al., *Study of quasielastic scattering using charged-current ν_μ -iron interactions in the MINOS near detector*, *Phys. Rev.* **D91** (2015) 012005, [`1410.8613`].

[54] J. A. Alpern Boehm, *A Measurement of Electron Neutrino Appearance with the MINOS Experiment*, Ph.D. thesis, Harvard University, 2009.

[55] B. Wang, *Muon-Neutrino Electron Elastic Scattering and a Search for the Muon-Neutrino Magnetic Moment in the NOvA Near Detector*, Ph.D. thesis, Southern Methodist University, 2017.

[56] M. Sanchez, "NOvA Results and Prospects." June, 2018.

[57] L. N. Hand, *Experimental investigation of pion electroproduction*, Phys. Rev. **129** (1963) 1834–1846.

[58] B. A. Kniehl, *Elastic e p scattering and the Weizsacker-Williams approximation*, Phys. Lett. **B254** (1991) 267–273.

[59] C. F. von Weizsacker, *Radiation emitted in collisions of very fast electrons*, Z. Phys. **88** (1934) 612–625.

[60] E. J. Williams, *Nature of the high-energy particles of penetrating radiation and status of ionization and radiation formulae*, Phys. Rev. **45** (1934) 729–730.

[61] E. Fermi, *On the Theory of the impact between atoms and electrically charged particles*, Z. Phys. **29** (1924) 315–327.

[62] S. Frixione, M. L. Mangano, P. Nason and G. Ridolfi, *Improving the Weizsacker-Williams approximation in electron - proton collisions*, Phys. Lett. **B319** (1993) 339–345, [hep-ph/9310350].

[63] A. Weber, "ND(s) for DUNE." May, 2018.

[64] DUNE collaboration, V. Papadimitriou, "Design of the LBNF Beamline." 2016.

[65] νSTORM collaboration, D. Adey et al., *Light sterile neutrino sensitivity at the nuSTORM facility*, Phys. Rev. **D89** (2014) 071301, [1402.5250].

[66] J. Smith and J. A. M. Vermaseren, *Electromagnetic Backgrounds in Neutrino Produced Trimuon Events*, Phys. Rev. **D17** (1978) 2288.

[67] C. H. Albright, J. Smith and J. A. M. Vermaseren, *A Comparison of Trimuon Production Mechanisms*, Phys. Rev. **D18** (1978) 108.

[68] ArgoNeuT collaboration, R. Acciarri et al., *First Observation of Low Energy Electron Neutrinos in a Liquid Argon Time Projection Chamber*, Phys. Rev. **D95** (2017) 072005, [1610.04102].

[69] D. Rein and L. M. Sehgal, *Coherent π^0 production in neutrino reactions*, Nuclear Physics B **223** (1983) 29 – 44.

[70] D. Rein and L. M. Sehgal, *PCAC and the Deficit of Forward Muons in pi+ Production by Neutrinos*, Phys. Lett. **B657** (2007) 207–209, [hep-ph/0606185].

[71] MiniBooNE collaboration, A. A. Aguilar-Arevalo et al., *Measurement of ν_μ-induced charged-current neutral pion production cross sections on mineral oil at $E_\nu \in 0.5 - 2.0$ GeV*, Phys. Rev. **D83** (2011) 052009, [1010.3264].

[72] MINERvA collaboration, A. Higuera et al., *Measurement of Coherent Production of $\pi^\pm$ in Neutrino and Antineutrino Beams on Carbon from E_ν of 1.5 to 20 GeV*, Phys. Rev. Lett. **113** (2014) 261802, [1409.3835].

[73] MINERvA collaboration, A. Mislivec et al., *Measurement of total and differential cross sections of neutrino and antineutrino coherent $\pi^\pm$ production on carbon*, Phys. Rev. **D97** (2018) 032014, [1711.01178].

[74] T2K collaboration, K. Abe et al., *First measurement of the muon neutrino charged current single pion production cross section on water with the T2K near detector*, Phys. Rev. **D95** (2017) 012010, [1605.07964].

[75] ArgoNeuT collaboration, R. Acciarri et al., *First Measurement of Neutrino and Antineutrino Coherent Charged Pion Production on Argon*, Phys. Rev. Lett. **113** (2014) 261801, [1408.0598].

[76] MiniBooNE collaboration, A. A. Aguilar-Arevalo et al., *Measurement of ν_μ and $\bar{\nu}_\mu$ induced neutral current single π^0 production cross sections on mineral oil at $E_\nu \sim \mathcal{O}(1\text{GeV})$*, Phys. Rev. **D81** (2010) 013005, [0911.2063].

[77] SciBooNE collaboration, Y. Kurimoto et al., *Improved measurement of neutral current coherent π^0 production on carbon in a few-GeV neutrino beam*, Phys. Rev. **D81** (2010) 111102, [1005.0059].

[78] ArgoNeuT collaboration, R. Acciarri et al., *Measurement of ν_μ and $\bar{\nu}_\mu$ neutral current $\pi^0 \to \gamma\gamma$ production in the ArgoNeuT detector, Phys. Rev.* **D96** (2017) 012006, [1511.00941].

[79] D. Rein and L. M. Sehgal, *Neutrino Excitation of Baryon Resonances and Single Pion Production, Annals Phys.* **133** (1981) 79–153.

[80] K2K collaboration, C. Mariani et al., *Measurement of inclusive π^0 production in the Charged-Current Interactions of Neutrinos in a 1.3-GeV wide band beam, Phys. Rev.* **D83** (2011) 054023, [1012.1794].

[81] A. C. Benvenuti et al., *Observation of New Particle Production by High-Energy Neutrinos and anti-neutrinos, Phys. Rev. Lett.* **34** (1975) 419.

[82] G. De Lellis, P. Migliozzi and P. Santorelli, *Charm physics with neutrinos, Phys. Rept.* **399** (2004) 227–320.

[83] V. P. Efrosinin, Yu. G. Kudenko and A. N. Khotjantsev, *Single-photon production in neutrino-nucleon interactions, Phys. Atom. Nucl.* **72** (2009) 459–464.

[84] A. Bodek, *Muon internal bremsstrahlung: A Conventional explanation for the excess nu(e) events in MiniBoone*, 0709.4004.

[85] A. M. Ankowski, O. Benhar, T. Mori, R. Yamaguchi and M. Sakuda, *Analysis of γ-ray production in neutral-current neutrino-oxygen interactions at energies above 200 mev, Phys. Rev. Lett.* **108** (Feb, 2012) 052505.

[86] S. Centelles Chuliá, E. Ma, R. Srivastava and J. W. F. Valle, *Dirac Neutrinos and Dark Matter Stability from Lepton Quarticity, Phys. Lett.* **B767** (2017) 209–213, [1606.04543].

[87] E. Ma and R. Srivastava, *Dirac or inverse seesaw neutrino masses with $B - L$ gauge symmetry and S_3 flavor symmetry, Phys. Lett.* **B741** (2015) 217–222, [1411.5042].

[88] A. Aranda, C. Bonilla, S. Morisi, E. Peinado and J. W. F. Valle, *Dirac neutrinos from flavor symmetry, Phys. Rev.* **D89** (2014) 033001, [1307.3553].

[89] P. Minkowski, *$\mu \to e\gamma$ at a Rate of One Out of 10^9 Muon Decays?, Phys. Lett.* **67B** (1977) 421–428.

[90] R. N. Mohapatra and G. Senjanovic, *Neutrino Mass and Spontaneous Parity Violation, Phys. Rev. Lett.* **44** (1980) 912.

[91] M. Gell-Mann, P. Ramond and R. Slansky, *Complex Spinors and Unified Theories, Conf. Proc.* **C790927** (1979) 315–321, [`1306.4669`].

[92] T. Yanagida, *HORIZONTAL SYMMETRY AND MASSES OF NEUTRINOS, Conf. Proc.* **C7902131** (1979) 95–99.

[93] G. Lazarides, Q. Shafi and C. Wetterich, *Proton Lifetime and Fermion Masses in an SO(10) Model, Nucl. Phys.* **B181** (1981) 287–300.

[94] R. N. Mohapatra and G. Senjanovic, *Neutrino Masses and Mixings in Gauge Models with Spontaneous Parity Violation, Phys. Rev.* **D23** (1981) 165.

[95] J. Schechter and J. W. F. Valle, *Neutrino Masses in SU(2) x U(1) Theories, Phys. Rev.* **D22** (1980) 2227.

[96] T. P. Cheng and L.-F. Li, *Neutrino Masses, Mixings and Oscillations in SU(2) x U(1) Models of Electroweak Interactions, Phys. Rev.* **D22** (1980) 2860.

[97] R. Foot, H. Lew, X. G. He and G. C. Joshi, *Seesaw Neutrino Masses Induced by a Triplet of Leptons, Z. Phys.* **C44** (1989) 441.

[98] S. F. King and C. Luhn, *Neutrino Mass and Mixing with Discrete Symmetry, Rept. Prog. Phys.* **76** (2013) 056201, [`1301.1340`].

[99] M. Fukugita and T. Yanagida, *Baryogenesis Without Grand Unification, Phys. Lett.* **B174** (1986) 45–47.

[100] T. Asaka and M. Shaposhnikov, *The nuMSM, dark matter and baryon asymmetry of the universe, Phys. Lett.* **B620** (2005) 17–26, [`hep-ph/0505013`].

[101] T. Asaka, S. Blanchet and M. Shaposhnikov, *The nuMSM, dark matter and neutrino masses, Phys. Lett.* **B631** (2005) 151–156, [`hep-ph/0503065`].

[102] C. Boehm, Y. Farzan, T. Hambye, S. Palomares-Ruiz and S. Pascoli, *Is it possible to explain neutrino masses with scalar dark matter?, Phys. Rev.* **D77** (2008) 043516, [`hep-ph/0612228`].

[103] E. Ma, *Verifiable radiative seesaw mechanism of neutrino mass and dark matter*, *Phys. Rev.* **D73** (2006) 077301, [`hep-ph/0601225`].

[104] S. Gabriel and S. Nandi, *A New two Higgs doublet model, Phys. Lett.* **B655** (2007) 141–147, [`hep-ph/0610253`].

[105] S. M. Davidson and H. E. Logan, *Dirac neutrinos from a second Higgs doublet*, *Phys. Rev.* **D80** (2009) 095008, [`0906.3335`].

[106] E. Bertuzzo, P. A. N. Machado, Z. Tabrizi and R. Zukanovich Funchal, *A Neutrinophilic 2HDM as a UV Completion for the Inverse Seesaw Mechanism*, *JHEP* **11** (2017) 004, [`1706.10000`].

[107] N. Nath, M. Ghosh, S. Goswami and S. Gupta, *Phenomenological study of extended seesaw model for light sterile neutrino, JHEP* **03** (2017) 075, [`1610.09090`].

[108] I. Esteban, M. C. Gonzalez-Garcia, A. Hernandez-Cabezudo, M. Maltoni and T. Schwetz, *Global analysis of three-flavour neutrino oscillations: synergies and tensions in the determination of θ_{23}, $\delta_{\rm CP}$, and the mass ordering*, `1811.05487`.

[109] J. M. Conrad, M. H. Shaevitz and T. Bolton, *Precision measurements with high-energy neutrino beams, Rev. Mod. Phys.* **70** (1998) 1341–1392, [`hep-ex/9707015`].

[110] MINOS collaboration, P. Adamson et al., *Neutrino and Antineutrino Inclusive Charged-current Cross Section Measurements with the MINOS Near Detector, Phys. Rev.* **D81** (2010) 072002, [`0910.2201`].

[111] MiniBooNE collaboration, A. A. Aguilar-Arevalo et al., *First measurement of the muon antineutrino double-differential charged-current quasielastic cross section*, *Phys. Rev.* **D88** (2013) 032001, [`1301.7067`].

[112] MINERvA collaboration, L. Ren et al., *Measurement of the antineutrino to neutrino charged-current interaction cross section ratio in MINERvA, Phys. Rev.* **D95** (2017) 072009, [`1701.04857`].

[113] DUNE collaboration, R. Acciarri et al., *Long-Baseline Neutrino Facility (LBNF) and Deep Underground Neutrino Experiment (DUNE)*, `1601.05471`.

[114] M. Blennow, P. Coloma, E. Fernandez-Martinez, J. Hernandez-Garcia and J. Lopez-Pavon, *Non-Unitarity, sterile neutrinos, and Non-Standard neutrino Interactions*, *JHEP* **04** (2017) 153, [1609.08637].

[115] S. Hannestad, R. S. Hansen and T. Tram, *How Self-Interactions can Reconcile Sterile Neutrinos with Cosmology*, *Phys. Rev. Lett.* **112** (2014) 031802, [1310.5926].

[116] B. Dasgupta and J. Kopp, *Cosmologically Safe eV-Scale Sterile Neutrinos and Improved Dark Matter Structure*, *Phys. Rev. Lett.* **112** (2014) 031803, [1310.6337].

[117] A. Mirizzi, G. Mangano, O. Pisanti and N. Saviano, *Collisional production of sterile neutrinos via secret interactions and cosmological implications*, *Phys. Rev.* **D91** (2015) 025019, [1410.1385].

[118] J. F. Cherry, A. Friedland and I. M. Shoemaker, *Short-baseline neutrino oscillations, Planck, and IceCube*, 1605.06506.

[119] F. Capozzi, I. M. Shoemaker and L. Vecchi, *Solar Neutrinos as a Probe of Dark Matter-Neutrino Interactions*, *JCAP* **1707** (2017) 021, [1702.08464].

[120] P. B. Denton, Y. Farzan and I. M. Shoemaker, *Activating the fourth neutrino of the 3+1 scheme*, *Phys. Rev.* **D99** (2019) 035003, [1811.01310].

[121] X. Chu, B. Dasgupta, M. Dentler, J. Kopp and N. Saviano, *Sterile neutrinos with secret interactions—cosmological discord?*, *JCAP* **1811** (2018) 049, [1806.10629].

[122] A. Esmaili and H. Nunokawa, *On the robustness of IceCube's bound on sterile neutrinos in the presence of non-standard interactions*, *Eur. Phys. J.* **C79** (2019) 70, [1810.11940].

[123] P. Ballett, S. Pascoli and M. Ross-Lonergan, *U(1)' mediated decays of heavy sterile neutrinos in MiniBooNE*, 1808.02915.

[124] C. A. Argüelles, M. Hostert and Y.-D. Tsai, *Testing New Physics Explanations of MiniBooNE Anomaly at Neutrino Scattering Experiments*, 1812.08768.

[125] C. Boehm, *Implications of a new light gauge boson for neutrino physics*, *Phys. Rev.* **D70** (2004) 055007, [hep-ph/0405240].

[126] D. G. Cerdeño, M. Fairbairn, T. Jubb, P. A. N. Machado, A. C. Vincent and C. Bœhm, *Physics from solar neutrinos in dark matter direct detection experiments*, *JHEP* **05** (2016) 118, [1604.01025].

[127] P. B. Denton, Y. Farzan and I. M. Shoemaker, *Testing large non-standard neutrino interactions with arbitrary mediator mass after COHERENT data*, *JHEP* **07** (2018) 037, [1804.03660].

[128] A. Falkowski, M. González-Alonso and Z. Tabrizi, *Reactor neutrino oscillations as constraints on Effective Field Theory*, 1901.04553.

[129] Y. Farzan, *A model for large non-standard interactions of neutrinos leading to the LMA-Dark solution*, *Phys. Lett.* **B748** (2015) 311–315, [1505.06906].

[130] P. Bakhti, Y. Farzan and M. Rajaee, *Secret interactions of neutrinos with light gauge boson at the DUNE near detector*, *Phys. Rev.* **D99** (2019) 055019, [1810.04441].

[131] X.-G. He, G. C. Joshi, H. Lew and R. R. Volkas, *Simplest Z-prime model*, *Phys. Rev.* **D44** (1991) 2118–2132.

[132] X. G. He, G. C. Joshi, H. Lew and R. R. Volkas, *NEW Z-prime PHENOMENOLOGY*, *Phys. Rev.* **D43** (1991) 22–24.

[133] J. Park, *Neutrino-Electron Scattering in MINERvA for Constraining the NuMI Neutrino Flux*, Ph.D. thesis, U. Rochester, 2013. 10.2172/1248363.

[134] J. Bian, *Measurement of Neutrino-Electron Elastic Scattering at NOvA Near Detector*, in *Proceedings, Meeting of the APS Division of Particles and Fields (DPF 2017): Fermilab, Batavia, Illinois, USA, July 31 - August 4, 2017*, 2017, 1710.03428.

[135] P. Ballett, M. Hostert, S. Pascoli, Y. F. Perez-Gonzalez, Z. Tabrizi and R. Zukanovich Funchal, *Neutrino Trident Scattering at Near Detectors*, *JHEP* **01** (2019) 119, [1807.10973].

[136] T. Araki, S. Hoshino, T. Ota, J. Sato and T. Shimomura, *Detecting the $L_\mu - L_\tau$ gauge boson at Belle II*, *Phys. Rev.* **D95** (2017) 055006, [1702.01497].

[137] S.-F. Ge, M. Lindner and W. Rodejohann, *Atmospheric Trident Production for Probing New Physics*, *Phys. Lett.* **B772** (2017) 164–168, [`1702.02617`].

[138] P. Batra, B. A. Dobrescu and D. Spivak, *Anomaly-free sets of fermions*, *J. Math. Phys.* **47** (2006) 082301, [`hep-ph/0510181`].

[139] J. A. Dror, R. Lasenby and M. Pospelov, *New constraints on light vectors coupled to anomalous currents*, *Phys. Rev. Lett.* **119** (2017) 141803, [`1705.06726`].

[140] V. D. Barger, E. Ma and K. Whisnant, *General Analysis of a Possible Second Weak Neutral Current in Gauge Models*, *Phys. Rev.* **D26** (1982) 2378.

[141] S. M. Barr, B. Bednarz and C. Benesh, *Anomaly Constraints and New U(1) Gauge Bosons*, *Phys. Rev.* **D34** (1986) 235.

[142] B. C. Allanach, J. Davighi and S. Melville, *An Anomaly-free Atlas: charting the space of flavour-dependent gauged $U(1)$ extensions of the Standard Model*, `1812.04602`.

[143] J. Ellis, M. Fairbairn and P. Tunney, *Anomaly-Free Models for Flavour Anomalies*, *Eur. Phys. J.* **C78** (2018) 238, [`1705.03447`].

[144] B. C. Allanach, J. Davighi and S. Melville, *Anomaly-free, flavour-dependent U(1) charge assignments for Standard Model/Standard Model plus three right-handed neutrino fermionic content*, Dec., 2018. 10.5281/zenodo.1478085.

[145] A. Ismail, W.-Y. Keung, K.-H. Tsao and J. Unwin, *Axial vector Z′ and anomaly cancellation*, *Nucl. Phys.* **B918** (2017) 220–244, [`1609.02188`].

[146] Y. Kahn, G. Krnjaic, S. Mishra-Sharma and T. M. P. Tait, *Light Weakly Coupled Axial Forces: Models, Constraints, and Projections*, *JHEP* **05** (2017) 002, [`1609.09072`].

[147] J. A. Dror, R. Lasenby and M. Pospelov, *Dark forces coupled to nonconserved currents*, *Phys. Rev.* **D96** (2017) 075036, [`1707.01503`].

[148] B. Holdom, *Two U(1)'s and Epsilon Charge Shifts*, *Phys. Lett.* **166B** (1986) 196–198.

[149] A. Kamada and H.-B. Yu, *Coherent Propagation of PeV Neutrinos and the Dip in the Neutrino Spectrum at IceCube, Phys. Rev.* **D92** (2015) 113004, [1504.00711].

[150] M. Ibe, W. Nakano and M. Suzuki, *Constraints on $L_\mu - L_\tau$ gauge interactions from rare kaon decay, Phys. Rev.* **D95** (2017) 055022, [1611.08460].

[151] J. Alexander et al., *Dark Sectors 2016 Workshop: Community Report*, 2016, 1608.08632, http://lss.fnal.gov/archive/2016/conf/fermilab-conf-16-421.pdf.

[152] T. Araki, F. Kaneko, T. Ota, J. Sato and T. Shimomura, *MeV scale leptonic force for cosmic neutrino spectrum and muon anomalous magnetic moment, Phys. Rev.* **D93** (2016) 013014, [1508.07471].

[153] J. Heeck and W. Rodejohann, *Gauged $L_\mu - L_\tau$ Symmetry at the Electroweak Scale, Phys. Rev.* **D84** (2011) 075007, [1107.5238].

[154] K. J. Kelly and Y. Zhang, *Mono-Neutrino at DUNE: New Signals From Neutrinophilic Thermal Dark Matter*, 1901.01259.

[155] M. Holder et al., *Observation of Trimuon Events Produced in Neutrino and anti-neutrino Interactions, Phys. Lett.* **70B** (1977) 393–395.

[156] CHORUS collaboration, A. Kayis-Topaksu et al., *Experimental study of trimuon events in neutrino charged-current interactions, Phys. Lett.* **B596** (2004) 44–53.

[157] A. Benvenuti et al., *Observation of a new process with trimuon production by high-energy neutrinos, Physical Review Letters* **38** (may, 1977) 1110–1113.

[158] B. C. Barish, J. F. Bartlett, A. Bodek, K. W. Brown, D. Buchholz, Y. K. Chu et al., *Observation of Trimuon Production by Neutrinos, Physical Review Letters* **38** (mar, 1977) 577–580.

[159] J. Smith and J. A. M. Vermaseren, *PH YSICAL RE VIE% 0 Electromagnetic backgrounds in neutrino-produced trimuon events*, .

[160] NuTeV collaboration, M. Goncharov et al., *Precise Measurement of Dimuon Production Cross-Sections in ν_μ Fe and $\bar{\nu}_\mu$ Fe Deep Inelastic Scattering at the Tevatron., Phys. Rev.* **D64** (2001) 112006, [hep-ex/0102049].

[161] W. Czyz, G. C. Sheppey and J. D. Walecka, *Neutrino production of lepton pairs through the point four-fermion interaction*, *Il Nuovo Cimento* **34** (oct, 1964) 404–435.

[162] J. Løvseth and M. Radomski, *Kinematical distributions of neutrino-produced lepton triplets*, *Physical Review D* **3** (1971) 2686–2706.

[163] C. F. Uhlemann and N. Kauer, *Narrow-width approximation accuracy*, *Nucl. Phys.* **B814** (2009) 195–211, [0807.4112].

[164] R. W. Brown, R. H. Hobbs, J. Smith and N. Stanko, *Intermediate boson. iii. virtual-boson effects in neutrino trident production*, *Phys. Rev.* **D6** (1972) 3273–3292.

[165] D. R. Albert, "The DUNE Near Detector." Aug., 2018.

[166] M. Steven, "Status of DUNE Near Detector." Oct., 2018.

[167] DUNE collaboration, "2016 DUNE fluxes." 2016.

[168] DUNE collaboration, "2016 DUNE fluxes." 2017.

[169] DUNE collaboration, "High-Pressure Argon gas TPC Option for the DUNE Near Detector." 2019.

[170] MINOS collaboration, D. G. Michael et al., *The Magnetized steel and scintillator calorimeters of the MINOS experiment*, *Nucl. Instrum. Meth.* **A596** (2008) 190–228, [0805.3170].

[171] MINERvA collaboration, L. Aliaga et al., *Design, Calibration, and Performance of the MINERvA Detector*, *Nucl. Instrum. Meth.* **A743** (2014) 130–159, [1305.5199].

[172] A. G. Abramov, N. A. Galyaev, V. I. Garkusha, J. Hylen, F. N. Novoskoltsev, A. D. Ryabov et al., *Beam optics and target conceptual designs for the NuMI project*, *Nucl. Instrum. Meth.* **A485** (2002) 209–227.

[173] A. Bodek, U. Sarica, D. Naples and L. Ren, *Methods to Determine Neutrino Flux at Low Energies:Investigation of the Low ν Method*, *Eur. Phys. J.* **C72** (2012) 1973, [1201.3025].

[174] NOMAD collaboration, P. Astier et al., *Neutrino production of opposite sign dimuons in the NOMAD experiment*, *Phys. Lett.* **B486** (2000) 35–48.

[175] NuTeV collaboration, T. Adams et al., *Evidence for diffractive charm production in muon-neutrino Fe and anti-muon-neutrino Fe scattering at the Tevatron*, *Phys. Rev.* **D61** (2000) 092001, [hep-ex/9909041].

[176] N. J. Baker, S. A. Kahn, M. J. Murtagh, N. P. Samios, M. Tanaka, C. Baltay et al., $\mu^- e^+$ *dilepton production in charged-current ν_μ interactions*, *Phys. Rev. D* **43** (May, 1991) 2765–2777.

[177] MINERvA collaboration, J. Park et al., *Measurement of Neutrino Flux from Neutrino-Electron Elastic Scattering*, *Phys. Rev.* **D93** (2016) 112007, [1512.07699].

[178] S. Bilmis, I. Turan, T. M. Aliev, M. Deniz, L. Singh and H. T. Wong, *Constraints on Dark Photon from Neutrino-Electron Scattering Experiments*, *Phys. Rev.* **D92** (2015) 033009, [1502.07763].

[179] CHARM-II collaboration, P. Vilain et al., *Precision measurement of electroweak parameters from the scattering of muon-neutrinos on electrons*, *Phys. Lett.* **B335** (1994) 246–252.

[180] G. Bellini et al., *Precision measurement of the 7Be solar neutrino interaction rate in Borexino*, *Phys. Rev. Lett.* **107** (2011) 141302, [1104.1816].

[181] M. B. Wise and Y. Zhang, *Lepton Flavorful Fifth Force and Depth-dependent Neutrino Matter Interactions*, *JHEP* **06** (2018) 053, [1803.00591].

[182] M. Bustamante and S. K. Agarwalla, *Universe's Worth of Electrons to Probe Long-Range Interactions of High-Energy Astrophysical Neutrinos*, *Phys. Rev. Lett.* **122** (2019) 061103, [1808.02042].

[183] S. Baek, N. G. Deshpande, X. G. He and P. Ko, *Muon anomalous g-2 and gauged L(muon) - L(tau) models*, *Phys. Rev.* **D64** (2001) 055006, [hep-ph/0104141].

[184] M. Pospelov, *Secluded U(1) below the weak scale*, *Phys. Rev.* **D80** (2009) 095002, [0811.1030].

[185] A. Kamada, K. Kaneta, K. Yanagi and H.-B. Yu, *Self-interacting dark matter and muon $g - 2$ in a gauged $U(1)_{L_\mu - L_\tau}$ model*, *JHEP* **06** (2018) 117, [1805.00651].

[186] MUON G-2 collaboration, G. W. Bennett et al., *Final Report of the Muon E821 Anomalous Magnetic Moment Measurement at BNL*, *Phys. Rev.* **D73** (2006) 072003, [hep-ex/0602035].

[187] RBC, UKQCD collaboration, T. Blum, P. A. Boyle, V. Gülpers, T. Izubuchi, L. Jin, C. Jung et al., *Calculation of the hadronic vacuum polarization contribution to the muon anomalous magnetic moment*, *Phys. Rev. Lett.* **121** (2018) 022003, [1801.07224].

[188] A. Keshavarzi, D. Nomura and T. Teubner, *Muon $g - 2$ and $\alpha(M_Z^2)$: a new data-based analysis*, *Phys. Rev.* **D97** (2018) 114025, [1802.02995].

[189] MUON G-2 collaboration, J. Grange et al., *Muon (g-2) Technical Design Report*, 1501.06858.

[190] R. Petti, ""Precision measurements of fundamental interactions in the ND(s)." 2018.

[191] H. Duyang, B. Guo, S. R. Mishra and R. Petti, *A Novel Approach to Neutrino-Hydrogen Measurements*, 1809.08752.

[192] LSND collaboration, C. Athanassopoulos et al., *Evidence for anti-muon-neutrino —> anti-electron-neutrino oscillations from the LSND experiment at LAMPF*, *Phys. Rev. Lett.* **77** (1996) 3082–3085, [nucl-ex/9605003].

[193] LSND collaboration, A. Aguilar-Arevalo et al., *Evidence for neutrino oscillations from the observation of anti-neutrino(electron) appearance in a anti-neutrino(muon) beam*, *Phys. Rev.* **D64** (2001) 112007, [hep-ex/0104049].

[194] MINIBOONE collaboration, A. A. Aguilar-Arevalo et al., *A Search for electron neutrino appearance at the $\Delta m^2 \sim 1 eV^2$ scale*, *Phys. Rev. Lett.* **98** (2007) 231801, [0704.1500].

[195] MINIBOONE collaboration, A. A. Aguilar-Arevalo et al., *Observation of a Significant Excess of Electron-Like Events in the MiniBooNE Short-Baseline Neutrino Experiment*, 1805.12028.

[196] ALEPH, CDF, D0, DELPHI, L3, OPAL, SLD, LEP ELECTROWEAK
WORKING GROUP, TEVATRON ELECTROWEAK WORKING GROUP, SLD
ELECTROWEAK AND HEAVY FLAVOUR GROUPS collaboration, L. E. W. Group,
Precision Electroweak Measurements and Constraints on the Standard Model,
`1012.2367`.

[197] Collin, G. H. and Argüelles, C. A. and Conrad, J. M. and Shaevitz, M. H., *First
Constraints on the Complete Neutrino Mixing Matrix with a Sterile Neutrino*,
`1607.00011`.

[198] F. Capozzi, C. Giunti, M. Laveder and A. Palazzo, *Joint short- and long-baseline
constraints on light sterile neutrinos*, *Phys. Rev.* **D95** (2017) 033006, [`1612.07764`].

[199] M. Dentler, Hernández-Cabezudo, J. Kopp, P. A. N. Machado, M. Maltoni,
I. Martinez-Soler et al., *Updated Global Analysis of Neutrino Oscillations in the
Presence of eV-Scale Sterile Neutrinos*, *JHEP* **08** (2018) 010, [`1803.10661`].

[200] MINIBOONE collaboration, A. A. Aguilar-Arevalo et al., *Unexplained Excess of
Electron-Like Events From a 1-GeV Neutrino Beam*, *Phys. Rev. Lett.* **102** (2009)
101802, [`0812.2243`].

[201] MINIBOONE collaboration, A. A. Aguilar-Arevalo et al., *A Combined $\nu_\mu \to \nu_e$ and
$\bar{\nu}_\mu \to \bar{\nu}_e$ Oscillation Analysis of the MiniBooNE Excesses*, 2012, `1207.4809`,
http://lss.fnal.gov/archive/2012/pub/fermilab-pub-12-394-ad-ppd.pdf.

[202] R. J. Hill, *On the single photon background to ν_e appearance at MiniBooNE*, *Phys.
Rev.* **D84** (2011) 017501, [`1002.4215`].

[203] H. Murayama and T. Yanagida, *LSND, SN1987A, and CPT violation*, *Phys. Lett.*
B520 (2001) 263–268, [`hep-ph/0010178`].

[204] A. Strumia, *Interpreting the LSND anomaly: Sterile neutrinos or CPT violation
or...?*, *Phys. Lett.* **B539** (2002) 91–101, [`hep-ph/0201134`].

[205] G. Barenboim, L. Borissov and J. D. Lykken, *CPT violating neutrinos in the light
of KamLAND*, `hep-ph/0212116`.

[206] M. C. Gonzalez-Garcia, M. Maltoni and T. Schwetz, *Status of the CPT violating interpretations of the LSND signal*, *Phys. Rev.* **D68** (2003) 053007, [`hep-ph/0306226`].

[207] V. Barger, D. Marfatia and K. Whisnant, *LSND anomaly from CPT violation in four neutrino models*, *Phys. Lett.* **B576** (2003) 303–308, [`hep-ph/0308299`].

[208] M. Sorel, J. M. Conrad and M. H. Shaevitz, *A Combined analysis of short baseline neutrino experiments in the (3+1) and (3+2) sterile neutrino oscillation hypotheses*, *Phys. Rev.* **D70** (2004) 073004, [`hep-ph/0305255`].

[209] G. Barenboim and N. E. Mavromatos, *CPT violating decoherence and LSND: A Possible window to Planck scale physics*, *JHEP* **01** (2005) 034, [`hep-ph/0404014`].

[210] K. M. Zurek, *New matter effects in neutrino oscillation experiments*, *JHEP* **10** (2004) 058, [`hep-ph/0405141`].

[211] D. B. Kaplan, A. E. Nelson and N. Weiner, *Neutrino oscillations as a probe of dark energy*, *Phys. Rev. Lett.* **93** (2004) 091801, [`hep-ph/0401099`].

[212] H. Pas, S. Pakvasa and T. J. Weiler, *Sterile-active neutrino oscillations and shortcuts in the extra dimension*, *Phys. Rev.* **D72** (2005) 095017, [`hep-ph/0504096`].

[213] A. de Gouvêa and Y. Grossman, *A Three-flavor, Lorentz-violating solution to the LSND anomaly*, *Phys. Rev.* **D74** (2006) 093008, [`hep-ph/0602237`].

[214] T. Schwetz, *LSND versus MiniBooNE: Sterile neutrinos with energy dependent masses and mixing?*, *JHEP* **02** (2008) 011, [`0710.2985`].

[215] Y. Farzan, T. Schwetz and A. Y. Smirnov, *Reconciling results of LSND, MiniBooNE and other experiments with soft decoherence*, *JHEP* **07** (2008) 067, [`0805.2098`].

[216] S. Hollenberg, O. Micu, H. Pas and T. J. Weiler, *Baseline-dependent neutrino oscillations with extra-dimensional shortcuts*, *Phys. Rev.* **D80** (2009) 093005, [`0906.0150`].

[217] A. E. Nelson, *Effects of CP Violation from Neutral Heavy Fermions on Neutrino Oscillations, and the LSND/MiniBooNE Anomalies*, *Phys. Rev.* **D84** (2011) 053001, [`1010.3970`].

[218] E. Akhmedov and T. Schwetz, *MiniBooNE and LSND data: Non-standard neutrino interactions in a (3+1) scheme versus (3+2) oscillations*, *JHEP* **10** (2010) 115, [1007.4171].

[219] J. S. Diaz and V. A. Kostelecky, *Three-parameter Lorentz-violating texture for neutrino mixing*, *Phys. Lett.* **B700** (2011) 25–28, [1012.5985].

[220] Y. Bai, R. Lu, S. Lu, J. Salvado and B. A. Stefanek, *Three Twin Neutrinos: Evidence from LSND and MiniBooNE*, *Phys. Rev.* **D93** (2016) 073004, [1512.05357].

[221] C. Giunti and E. M. Zavanin, *Appearance–disappearance relation in $3 + N_s$ short-baseline neutrino oscillations*, *Mod. Phys. Lett.* **A31** (2015) 1650003, [1508.03172].

[222] J. Liao and D. Marfatia, *Impact of nonstandard interactions on sterile neutrino searches at IceCube*, *Phys. Rev. Lett.* **117** (2016) 071802, [1602.08766].

[223] D. K. Papoulias and T. S. Kosmas, *Impact of Nonstandard Interactions on Neutrino-Nucleon Scattering*, *Adv. High Energy Phys.* **2016** (2016) 1490860, [1611.05069].

[224] Moss, Zander and Moulai, Marjon H. and Argüelles, Carlos A. and Conrad, Janet M., *Exploring a nonminimal sterile neutrino model involving decay at IceCube*, *Phys. Rev.* **D97** (2018) 055017, [1711.05921].

[225] M. Carena, Y.-Y. Li, C. S. Machado, P. A. N. Machado and C. E. M. Wagner, *Neutrinos in Large Extra Dimensions and Short-Baseline ν_e Appearance*, 1708.09548.

[226] J. Liao, D. Marfatia and K. Whisnant, *MiniBooNE, MINOS+ and IceCube data imply a baroque neutrino sector*, 1810.01000.

[227] J. Asaadi, E. Church, R. Guenette, B. J. P. Jones and A. M. Szelc, *New light Higgs boson and short-baseline neutrino anomalies*, *Phys. Rev.* **D97** (2018) 075021, [1712.08019].

[228] D. Döring, H. Päs, P. Sicking and T. J. Weiler, *Sterile Neutrinos with Altered Dispersion Relations as an Explanation for the MiniBooNE, LSND, Gallium and Reactor Anomalies*, `1808.07460`.

[229] S. N. Gninenko, *The MiniBooNE anomaly and heavy neutrino decay, Phys. Rev. Lett.* **103** (2009) 241802, [`0902.3802`].

[230] S. N. Gninenko, *A resolution of puzzles from the LSND, KARMEN, and MiniBooNE experiments, Phys. Rev.* **D83** (2011) 015015, [`1009.5536`].

[231] C. Dib, J. C. Helo, S. Kovalenko and I. Schmidt, *Sterile neutrino decay explanation of LSND and MiniBooNE anomalies, Phys. Rev.* **D84** (2011) 071301, [`1105.4664`].

[232] D. McKeen and M. Pospelov, *Muon Capture Constraints on Sterile Neutrino Properties, Phys. Rev.* **D82** (2010) 113018, [`1011.3046`].

[233] M. Masip, P. Masjuan and D. Meloni, *Heavy neutrino decays at MiniBooNE, JHEP* **01** (2013) 106, [`1210.1519`].

[234] M. Masip and P. Masjuan, *Heavy-neutrino decays at neutrino telescopes, Phys. Rev.* **D83** (2011) 091301, [`1103.0689`].

[235] S. N. Gninenko, *New limits on radiative sterile neutrino decays from a search for single photons in neutrino interactions, Phys. Lett.* **B710** (2012) 86–90, [`1201.5194`].

[236] G. Magill, R. Plestid, M. Pospelov and Y.-D. Tsai, *Dipole portal to heavy neutral leptons*, `1803.03262`.

[237] E. Bertuzzo, S. Jana, P. A. N. Machado and R. Zukanovich Funchal, *Neutrino Masses and Mixings Dynamically Generated by a Light Dark Sector*, `1808.02500`.

[238] LSND collaboration, L. B. Auerbach et al., *Measurement of electron - neutrino - electron elastic scattering, Phys. Rev.* **D63** (2001) 112001, [`hep-ex/0101039`].

[239] M. Pospelov and Y.-D. Tsai, *Light scalars and dark photons in Borexino and LSND experiments, Phys. Lett.* **B785** (2018) 288–295, [`1706.00424`].

[240] G. Magill, R. Plestid, M. Pospelov and Y.-D. Tsai, *Millicharged particles in neutrino experiments*, `1806.03310`.

[241] E. Valencia-Rodriguez, *Neutrino - Electron Scattering in MINERνA for Constraint NuMI Flux at Medium*, Ph.D. thesis, Guanajuato U., 2016. 10.2172/1341804.

[242] CHARM-II collaboration, K. De Winter et al., *A Detector for the Study of Neutrino - Electron Scattering, Nucl. Instrum. Meth.* **A278** (1989) 670.

[243] CHARM-II collaboration, D. Geiregat et al., *Calibration and performance of the CHARM-II detector, Nucl. Instrum. Meth.* **A325** (1993) 92–108.

[244] J. A. Formaggio, J. M. Conrad, M. Shaevitz, A. Vaitaitis and R. Drucker, *Helicity effects in neutral heavy lepton decays, Phys. Rev.* **D57** (1998) 7037–7040.

[245] A. B. Balantekin, A. de Gouvêa and B. Kayser, *Addressing the Majorana vs. Dirac Question with Neutrino Decays*, 1808.10518.

[246] E. J. Chun, J.-C. Park and S. Scopel, *Dark matter and a new gauge boson through kinetic mixing, JHEP* **02** (2011) 100, [1011.3300].

[247] S. Parke and M. Ross-Lonergan, *Unitarity and the Three Flavour Neutrino Mixing Matrix*, 1508.05095.

[248] Berger, M.J. and Coursey, J.S. and Zucker, M.A. and Chang, J., "https://dx.doi.org/10.18434/T4NC7P."

[249] W. R. Leo, *Techniques for Nuclear and Particle Physics Experiments: A How to Approach.* 1987.

[250] Particle Data Group collaboration, M. Tanabashi et al., *Review of Particle Physics, Phys. Rev.* **D98** (2018) 030001.

[251] CHARM collaboration, J. V. Allaby et al., *Total Cross-sections of Charged Current Neutrino and Anti-neutrino Interactions on Isoscalar Nuclei, Z. Phys.* **C38** (1988) 403–410.

[252] J. R. Jordan, Y. Kahn, G. Krnjaic, M. Moschella and J. Spitz, *Severe Constraints on New Physics Explanations of the MiniBooNE Excess*, 1810.07185.

[253] MINOS collaboration, P. Adamson et al., *Measurement of single π^0 production by coherent neutral-current ν Fe interactions in the MINOS Near Detector, Phys. Rev.* **D94** (2016) 072006, [1608.05702].

[254] MINERvA collaboration, J. Wolcott et al., *Evidence for Neutral-Current Diffractive π^0 Production from Hydrogen in Neutrino Interactions on Hydrocarbon*, *Phys. Rev. Lett.* **117** (2016) 111801, [`1604.01728`].

[255] MINERvA collaboration, L. Aliaga et al., *Neutrino Flux Predictions for the NuMI Beam*, *Phys. Rev.* **D94** (2016) 092005, [`1607.00704`].

[256] J. A. A. Boehm, *Measurement of electron neutrino appearance with the MINOS experiment*, Ph.D. thesis, Harvard U., 2009. 10.2172/957077.

[257] A. Aurisano, "Recent Results from MINOS and MINOS+." June, 2018.

[258] L. Loiacono, "Neutrino Flux Simulations with an Evacuated and Helium Gas Filled Decay Pipe ." 2007.

[259] P. Vahle, "NOvA Status and Prospects, 2018 July PUBLIC PAC Meeting." July, 2018.

[260] B. A. Kniehl and A. Pilaftsis, *Mixing renormalization in Majorana neutrino theories*, *Nucl. Phys.* **B474** (1996) 286–308, [`hep-ph/9601390`].

[261] W. Grimus and L. Lavoura, *One-loop corrections to the seesaw mechanism in the multi-Higgs-doublet standard model*, *Phys. Lett.* **B546** (2002) 86–95, [`hep-ph/0207229`].

[262] D. Aristizabal Sierra and C. E. Yaguna, *On the importance of the 1-loop finite corrections to seesaw neutrino masses*, *JHEP* **08** (2011) 013, [`1106.3587`].